

Crystalline topological semimetals: Classification and properties

Von der Fakultät Mathematik und Physik der Universität Stuttgart
zur Erlangung der Würde eines Doktors der Naturwissenschaften
(Dr. rer. nat.) genehmigte Abhandlung

vorgelegt von

Andreas Leonhardt

aus Göppingen, Deutschland

Hauptberichter:	Prof. Dr. Walter Metzner
Mitberichter:	Dr. Andreas P. Schnyder Prof. Dr. Hans Peter Büchler
Tag der mündlichen Prüfung:	25.10.2022

Max-Planck-Institut für Festkörperforschung
Universität Stuttgart
2022

Contents

1	Introduction	10
2	Background	14
2.1	Group theory in solids	14
2.1.1	Space groups	15
2.1.2	Group action on a Hamiltonian	19
2.1.3	Double space groups	19
2.1.4	Time-reversal symmetry	20
2.2	Fibre bundles	21
2.3	Nodes and their invariants	23
2.3.1	Berry phase	24
2.3.2	Berry curvature	25
2.4	Low-energy Hamiltonians	26
3	Symmetry-enforced nodes	29
3.1	Weyl points	31
3.1.1	Weyl points at high-symmetry points	32
3.2	Higher-order point crossings	34
3.2.1	Double Weyl points	35
3.2.2	Fourfold double Weyl points	37
3.2.3	Fourfold quadruple Weyl points	40
3.3	Movable point crossings on rotation axes	43
3.3.1	Hourglass dispersion from twofold screw rotations	43
3.3.2	Accordion states from fourfold screw rotations	45
3.3.3	Compatibility relations spanning several rotation axis	47

3.4	Topological nodal planes	51
3.5	Case study for the chiral space groups 19 and 92/96	55
3.5.1	Tight-binding model for SG 19	55
3.5.2	Example material Ba_3Sn_2 in SG 96	57
3.6	Dirac points	60
3.6.1	Dirac points at high-symmetry points	61
3.6.2	Movable Dirac points	65
3.7	Line degeneracies	66
3.7.1	Pinned nodal lines	67
3.7.2	Movable nodal lines	70
3.7.3	Interlinked nodal lines	75
3.7.4	Almost movable lines	78
3.7.5	Dirac lines	79
3.8	Enforced topology in planes	80
3.9	Summary	85
4	Quasiparticle interference of drumhead surface states	86
4.1	Nodal loops	86
4.2	Berry phase and surface states	89
4.3	Spin-orbit coupled nodal-loop semimetal	94
4.4	Quasiparticle interference	95
4.5	Spin-resolved quasiparticle interference	99
4.6	Summary	102
5	Anomalous Hall effect in nodal line system	103
5.1	Model Hamiltonian	103
5.2	Berry curvature and anomalous velocity	105
5.3	Periodic driving	106
5.3.1	Floquet formalism	106
5.3.2	Effective Hamiltonian	110
5.3.3	Keldysh formalism for the quasistatic system	112
5.4	Current in a finite sample	116
5.5	Conductivity tensor	121

5.6	Real-time description	129
5.7	Summary	134
6	Conclusion	136
A	Group action on crystal momentum	140
B	Symmetry-enforced nodes in orthorhombic and tetragonal space groups	142
C	Derivation of DC conductivity for a periodically driven system	157
	Bibliography	161

List of Figures

3.1	Dispersion of symmetry-enforced Weyl nodes with Chern number $ \mathcal{C} \geq 2$	36
3.2	Dispersion of the fourfold double Weyl point in Pd_7Se_4	40
3.3	Schematic hourglass dispersion	44
3.4	Connectivity diagrams for fourfold screw rotations	46
3.5	Band crossings enforced by compatibility relations comprising three rotation axes in spinless band structures	49
3.6	Compatibility relations at R in SG 19	52
3.7	Elementary band representation in SG 19	58
3.8	Elementary band representation in SG 96	59
3.9	Dispersion around S in AuTlSb	64
3.10	Dispersion around the fourfold nodal line in NaSn_5	71
3.11	Pinned and movable lines in mirror planes	73
3.12	Dispersion around R in AuTlSb	74
3.13	Arrangement of bands along three rotation axes with hourglass nodal lines	77
3.14	Symmetry-enforced weak topology in Ir_2Si	83
3.15	Symmetry-enforced weak topology in Sr_2Bi_3	84
4.1	Illustration and dispersion of the nodal-loop model	88
4.2	Bulk and surface BZ for the nodal-loop system	90
4.3	Surface states of the open chain	92
4.4	Dispersion and surface density of states for the NLSM	95
4.5	QPI patterns for the spinless case at different bias	97

4.6	LDOS at constant ω with SOC	98
4.7	Surface density of states for the NLSM	100
4.8	Spin-resolved QPI patterns	101
5.1	Floquet quasienergy band structure of the driven NLSM projected onto the $n = 0$ component.	110
5.2	Berry curvature for a gapped nodal loop	111
5.3	Schematic setup of the driven NLSM between two leads	117
5.4	Currents in a finite-sized driven NLSM	120
5.5	Mean occupation of Floquet quasienergy bands	124
5.6	Conductivity as function of driving amplitude	126
5.7	Chemical potential dependence of the conductivity	127
5.8	Lifetime dependence of the conductivity	127
5.9	Detailed occupation of bands close to the nodal line for different values of Γ	128
5.10	Real-time calculation of the longitudinal current J_x and anomalous Hall current J_z	131
5.11	Time-averaged current for different lifetimes	133
B.1	Brillouin zones of orthorhombic lattices	144
B.2	Brillouin zones of the tetragonal lattices	152
C.1	Graphical representation of the conductivity tensor in terms of Feynman diagrams	158

Nomenclature

\mathcal{T}	time-reversal symmetry
σ_i, τ_i	Pauli matrices in spin, orbital space, respectively
BZ	Brillouin zone
DP	Dirac point
EBR	elementary band representation
FBZ	Floquet Brillouin zone, $[-\frac{\pi}{T}, \frac{\pi}{T})$
ICSD	Inorganic Crystal Structure Database
LDOS	local density of states
MP	Materials Project
NLSM	nodal-line semimetal
QPI	quasiparticle interference
SG	space group
SOC	spin-orbit coupling
STM	scanning tunneling microscope
TRIM	time-reversal invariant momentum
WP	Weyl point

Abstract

We investigate topological semimetals in the context of crystalline symmetries. In the first part, we classify all symmetry-enforced band crossings in orthorhombic and tetragonal space groups with time-reversal symmetry and identify all types of two- and fourfold degenerate point and line crossings, and nodal planes. Our comprehensive findings are listed in several tables, which serve as a reference and source of knowledge for band topology. For each type of crossing we explain the pairing mechanism and provide a local low-energy Hamiltonian, from which we evaluate its topological invariant. This systematic analysis revealed several higher-order point crossings with Chern numbers of $\mathcal{C} = \pm 2$ or $\mathcal{C} = \pm 4$ and nodal planes, which necessarily carry a topological charge. The systematic analysis also includes global restrictions on the band structure by symmetry. These lead to movable Weyl and Dirac points on rotation axes and movable nodal lines in mirror planes, which make up nodal loops or nodal chains in certain space groups. In the second part, we investigate observable consequences of a nodal-line semimetal. First, we calculate the drumhead surface states of a nodal-loop semimetal and calculate their signature in quasiparticle interference patterns from scattering at a surface impurity. We show that in the presence of strong spin-orbit coupling, the surface states become spin polarized and demonstrate that their spin structure can be resolved in spin-sensitive measurements of interference patterns from scattering at a magnetic impurity. We then calculate transport properties of the nodal-line semimetal subject to periodic driving by circularly polarized light. The driving field breaks the symmetry protecting the nodal line and leads to an anomalous Hall effect. In the Floquet picture, we demonstrate that the nodal line is weakly gapped except for two Weyl points. The anomalous Hall effect can then be explained by the Berry curvature between these two Weyl points.

Zusammenfassung

In dieser Arbeit studieren wir topologische Halbmetalle, deren Bandkreuzungen durch räumliche Symmetrie erzwungen oder geschützt sind. Im ersten Teil der Arbeit identifizieren wir alle erzwungenen Bandkreuzungen in orthorhombischen und tetragonalen Kristallsystemen mit Zeitumkehr-Symmetrie und präsentieren diese in umfassenden Tabellen, sortiert nach entarteten Punkten, Linien und Ebenen. Für jeden Typus präsentieren wir Niedrigenergie-Modelle, eine Beschreibung des Mechanismus, der zur Entartung führt, sowie eine Analyse der topologischen Eigenschaften. Die systematische Analyse offenbart unter anderem zweifach und vierfach entartete Punktkreuzungen mit Chernzahlen bis zu $\mathcal{C} = 4$, und topologische Ebenen, die notwendigerweise topologisch nichttrivial sind. Berücksichtigt wurden insbesondere auch globale Randbedingungen nichtsymmorpher Raumgruppen, die bewegliche Punktkreuzungen auf Rotationsachsen und bewegliche entartete Linien und Ketten in Spiegelebenen erzwingen. Der zweite Teil dieser Arbeit befasst sich mit beobachtbaren Konsequenzen topologischer Halbmetalle mit Linienkreuzungen. Wir berechnen die Oberflächenzustände eines Halbmetalles mit einer Ringkreuzung und deren Signatur in den Mustern der Quasiteilchen-Streuung an Punktdefekten der Oberfläche. Es wird gezeigt, dass Spin-Bahnkopplung diese Oberflächenzustände aufspaltet und deren Spinstruktur durch spinauflösende Messungen der Streuung an magnetischen Störstellen gemessen werden kann. Wir berechnen außerdem die Transporteigenschaften eines solchen Halbmetalles mit Ringkreuzung, das durch zirkular polarisiertes Licht periodisch getrieben wird. Die Symmetrien, welche die Bandkreuzung schützen, werden durch das Licht gebrochen, was zu einer anomalen Hall-Leitfähigkeit führt. Im Floquet-Formalismus kann demonstriert werden, dass die Linienkreuzung bis auf zwei Weyl-Punkte aufspaltet und dass die anomale Hall-Leitfähigkeit auf den Fluss der Berry-Krümmung zwischen diesen Punkten zurückgeführt werden kann.

1. Introduction

Symmetries are an essential ingredient in the modern formulation of fundamental physics. Group theory provides an analytical approach to virtually all physical systems with symmetries and allows to make definitive, qualitative statements, for example about degeneracies, allowed transitions and conserved quantities. In condensed matter physics, the use of symmetry representations is a powerful concept for reducing complexity in the description of periodically ordered matter. The 17 wallpaper groups and 230 space groups are the complete collection of all possible and distinct symmetry groups containing discrete translations in two or three dimensions, respectively. and were already identified in 1891 [1, 2], They were crucial in the development of crystallography and all periodically ordered systems in three dimensions can be classified in terms of their space groups. Foremost, for weakly interacting systems group theory provides the basis for separating an infinite-dimensional Hilbert space into subspaces labeled by the crystal momentum \mathbf{k} . In the single particle picture, each of these subspaces are finite dimensional and provide the basis for understanding the properties of materials in terms of their band structure. Inversion, reflections and discrete rotations can further reduce complexity by decoupling subspaces with different transformation properties. A complete description of degeneracies in terms of orthogonal subspaces at high-symmetry points can be given for any band structure on the basis of orbitals at Wyckoff positions in terms of their irreducible representations of the space group [3, 4].

With the advent of topology in condensed matter, the focus shifted from local quantities, like degeneracies of eigenvalues or symmetry allowed or forbidden transitions at some \mathbf{k} , to the global behavior of eigenstates for vary-

ing external parameters. The importance of a global phase winding under periodic changes of an external parameter that cannot be removed by any gauge transformation has been recognized in 1984 by M. V. Berry [5] and subsequently applied to the crystal momentum \mathbf{k} [6]. In the context of single-particle band structures, topology is used to identify the different ways eigenstates of the Hamiltonian can be smoothly assigned to each crystal momentum \mathbf{k} up to gauge transformations. The classification of such a map takes the whole parameter space into account and can be nontrivial in a projected subspace, e.g., the subset of occupied bands [7]. This idea is presented together with a short introduction to symmetries in crystals in Chapter 2.

Topological insulators were the first examples of nontrivial topology of the valence and conduction bands [8–10]. The explanation of the integer quantum Hall effect in two-dimensional electron gases in terms of the topological invariant of the bulk states showed the importance of topology in observable quantities [11, 12]. All possible topological insulators were subsequently classified in the tenfold way according to the presence or absence of the nonspatial symmetries, time-reversal, particle-hole or chiral symmetry and dimension [13–15]. This classification is valid for parameter spaces of arbitrary dimension and also covers crystal analogues, e.g., time periodic systems [16], (multidimensional) Floquet spaces [17–20] and time crystals [21]. The classification was then further extended to symmetry-protected topological phases in the presence of various spatial symmetries [22, 23], culminating in the complete classification of all known band insulators based on elementary band representations [24].

In topological semimetals, the same methods can be applied to characterize gapless systems with band crossings in terms of the topology on gapped sub-manifolds surrounding the degeneracies. Topologically protected band crossings are therefore inherently non-local and cannot be removed by local perturbations. Most famously, Weyl and Dirac semimetals have topologically protected band crossings, whose low-energy spectrum provides a condensed matter analogue of the Weyl and Dirac fermions of elementary particle physics [25–29]. Beyond these most famous examples, the combination of spatial and non-spatial symmetries brings forth a variety of topological

degeneracies without a high-energy analogue. Those comprise not only point crossings of up to eight bands, but also higher dimensional crossings along so-called nodal lines [29, 23] and nodal planes [30, 31] in the Brillouin zone, each with their own topological invariants. The topological classification of band crossings in time-reversal symmetric and magnetic space groups is still ongoing. Although a purely symmetry-based analysis is qualitatively exact, it cannot predict the magnitude of band splittings and the energy at which they appear. This poses a challenge for finding good example candidates, in which the band crossing of interest is at a relevant energy scale, well isolated from other bands and the band splitting is large enough to be experimentally observable. A promising approach to identify candidate materials is given by restricting the search to space groups, where the symmetries already guarantee the existence of topological band crossings. To aid this search, we conduct a systematic classification and provide a complete reference of symmetry-enforced band crossings. In Chapter 3, we will introduce the methods and discuss examples of all types of symmetry-enforced band crossings in time-reversal symmetric crystals in the orthorhombic and tetragonal space groups together with an analysis of their topological properties. For these systems, we present comprehensive lists of all symmetry-enforced degenerate points, lines and planes in Appendix B. The analysis is done in terms of representation theory and compatibility relations, identifying all types of symmetry-enforced band crossings. Expanding the Hamiltonians around the degenerate points provides a way to evaluate the topological invariants in the abstract case.

Topological materials are not only of fundamental interest, but have unique and robust experimental signatures with potential applications in functional materials and devices. The winding of eigenstates in a topological material has consequences for example for electric and thermal transport properties [12], electromagnetic response functions [32–34] and the surface spectrum through the bulk-boundary correspondence [35–38]. In the last two chapters, we will shift our focus to nodal-loop semimetals and calculate the influence of their topology on observable quantities. Firstly, we will focus on surface states and the relation to the bulk topology in Chapter 4. More

specifically, we will calculate the signature of the so-called drumhead surface states in the quasiparticle interference pattern from surface impurities. Magnetic impurities in combination with spin-resolved scanning tunneling microscopy allows to reveal the spin texture of the surface states. Secondly, nontrivial topology is expected to lead to new transport phenomenon. In the case of a nodal-loop semimetal, breaking the symmetry of the system with polarized light is expected to lead to an anomalous Hall current. In Chapter 5, we calculate the currents in a driven nodal-loop semimetal using various methods.

2. Background

In this chapter we introduce the mathematical foundation and notation for the following chapters. We will briefly review the concept of symmetry groups and their representations applied to quantum states and lattice Hamiltonians. Finally, we introduce the concept of topology for single-particle band structures in the framework of fibre bundles and define the Berry connection and curvature.

2.1 Group theory in solids

The symmetries of a system form a group \mathcal{G} , with the group operation $\circ : \mathcal{G} \times \mathcal{G} \rightarrow \mathcal{G}$ meaning the consecutive application of two symmetry operations. The identity id is to be understood as the trivial symmetry of no transformation. The inverse of a symmetry is given by the inverse transformation, e.g., a rotation in the other direction.

A matrix representation is a map $\rho : \mathcal{G} \rightarrow \text{U}(N)$, that assigns every element $R_i \in \mathcal{G}$ a unitary matrix $\rho(R_i) = U_i$ in such a way, that the group structure is preserved under matrix multiplication,

$$\rho(R_i \circ R_j) = \rho(R_i)\rho(R_j) = U_i U_j, \quad (2.1.1)$$

$$\rho(\text{id}) = \mathbb{1}_{N \times N}. \quad (2.1.2)$$

A matrix representation $\{U_i\}$ is not unique, since for any unitary matrix V , $\{V U_i V^\dagger\}$ is also a representation of the same group. Likewise, the direct sum of two representations forms a representation. For a finite group, there are only a finite number of inequivalent representation that cannot be written

as direct sum of lower-dimensional representations. These are called the irreducible representations.

The electron structure of a crystal, described by a Hamiltonian $H(\mathbf{r})$ is invariant under a symmetry group, if a matrix representation exists, such that for every spatial symmetry R_i and its representation U_i the Hamiltonian is invariant,

$$U_i H(\mathbf{r}) U_i^\dagger = H(R_i(\mathbf{r})). \quad (2.1.3)$$

If the representation $\{U_i\}$ can be decomposed in irreducible representations, the Hamiltonian can be block-diagonalized with each block transforming under one of the irreducible representations.

2.1.1 Space groups

A space group (SG) describes the mathematical symmetries of the atoms in a crystal structure. Space groups contain discrete translations and potentially point group symmetries, like rotations, reflections and inversions. Finally, some space groups also contain nonsymmorphic symmetries, which can be understood as a combination of a point group symmetry with a fractional lattice translation in such a way, that no point is invariant. Two SGs are seen as equivalent, if they can be transformed into each other by a basis transformation. With this definition, there are 230 different SGs. In the following, we introduce different types of symmetries together with their notation.

Discrete translation groups

Discrete translation groups are the symmetry groups of lattices and form a subgroup of each SG. A lattice in three dimensions is generated from three linear independent vectors \mathbf{a}_i , $i = 1, 2, 3$, and a site \mathbf{X} in the lattice can be described as a linear combination of these three vectors with integer coefficients,

$$\mathbf{X} = n_1 \mathbf{a}_1 + n_2 \mathbf{a}_2 + n_3 \mathbf{a}_3, \quad (2.1.4)$$

with $n_1, n_2, n_3 \in \mathbb{Z}$. To describe crystals as three dimensional lattices, they are either assumed to extend to infinity or have periodic boundary conditions. In the latter case, there is a finite number N_i for each lattice direction, after which lattice sites are identified, that is, the coefficients in Eq. (2.1.4) are $n_i \in \mathbb{Z}/N_i$. Depending on the relative length and angles of the generators, a lattice belongs to one of the 14 Bravais lattices [39].

The symmetry groups of a lattice consists of all integer valued translations $\mathbf{T} = \sum_{i=1}^3 n_i \mathbf{a}_i$, that map a lattice site onto another and this way the lattice to itself. We will use the compact notation $t(n_1, n_2, n_3)$ to denote (fractional) translations compactly in multiples of the lattice vectors. Each of the lattice generators \mathbf{a}_i also generates a translation subgroup. For lattices with periodic boundary conditions, these are cyclic groups of order N_i . Since all translations commute, these are finite abelian groups. It follows from Schur's lemma that irreducible representations of finite abelian subgroups are one-dimensional [40]. One-dimensional unitary matrices are just phases that can be parametrized by a real number ϕ , $e^{i\phi} \in \text{U}(1)$, $\phi \in [0, 2\pi)$. Irreducible representations of the three dimensional translation group are also one-dimensional and can be written as products of the individual phases. Commonly, a three component vector \mathbf{k} is introduced to parametrize the translation eigenvalue for a translation by \mathbf{T} as $\phi = \mathbf{k} \cdot \mathbf{T}$. Two labels \mathbf{k}_1 and \mathbf{k}_2 are identified, if they label the same translation group representation, i.e. for every lattice translation \mathbf{T} their difference has translation eigenvalue 1, which is identical to the condition

$$(\mathbf{k}_1 - \mathbf{k}_2) \cdot \mathbf{T} = 2\pi n, \quad n \in \mathbb{Z}, \forall \mathbf{T}. \quad (2.1.5)$$

The space of all \mathbf{k} is therefore also invariant under discrete translations and forms a three dimensional lattice, called the reciprocal lattice, spanned by the lattice vectors \mathbf{K}_i defined via $\mathbf{K}_i \cdot \mathbf{a}_j = 2\pi\delta_{ij}$. The labels become unique by restriction to the first Brillouin zone (BZ) of the reciprocal lattice [41].

Any single particle Hamiltonian invariant under the discrete translation group can be block-diagonalized with respect to the different irreducible representations labeled by \mathbf{k} . According to Eq. (2.1.3) the eigenfunctions of a

block $H(\mathbf{k}) = \sum_{\alpha} E_{\alpha,\mathbf{k}} \Psi_{\alpha,\mathbf{k}}(\mathbf{r})^* \Psi_{\alpha,\mathbf{k}}(\mathbf{r})$, labeled by some internal index α , are also eigenvectors of lattice translations \mathbf{T} and transform as

$$\Psi_{\alpha,\mathbf{k}}(\mathbf{r} + \mathbf{T}) = e^{i\mathbf{k}\cdot\mathbf{T}} \Psi_{\alpha,\mathbf{k}}(\mathbf{r}) \quad (2.1.6)$$

This is a group theoretic proof of Bloch's theorem. Dividing by the proper phase factor reproduces the periodic part of the Bloch wave function,

$$u_{\alpha,\mathbf{k}}(\mathbf{r}) = e^{-i\mathbf{k}\cdot\mathbf{r}} \Psi_{\alpha,\mathbf{k}}(\mathbf{r}) \quad (2.1.7)$$

and \mathbf{k} is the crystal momentum of the Bloch wave function.

Point group symmetries

Symmetry groups that leave at least one point in space invariant are called point groups. Those consist of rotations, reflections, inversion and rotoinversions. In a space group, a point group symmetry can be combined with any lattice translation, resulting in another point group symmetry with its invariant point shifted to another position. A point group symmetry is therefore given in terms of a representative with relation to an arbitrarily chosen origin. The combination with all lattice translations forms a coset of the translation group. The rotations compatible with the Bravais lattices are two-, three-, four- and sixfold. They will leave an axis invariant and are denoted in this thesis following Hermann-Mauguin notation [42, 43], by the numbers 2, 3, 4 and 6, respectively. Additionally, we will indicate the direction of the symmetry axis by a subscript, e.g., 2_{001} for a rotation with the invariant axis in $[001]$ direction. Reflections leave a plane invariant and are indicated by the letter M , followed by the subscript of its invariant plane. In this notation, the plane M_{001} leaves the (001) plane invariant, which implies its surface normal is aligned with $[001]$. Inversion and improper rotations leave only one point invariant. The former is denoted by \mathcal{P} , the latter can be understood as a rotation followed by a reflection in a plane perpendicular to the rotation axis and is indicated by writing the rotation with a bar, e.g., $\bar{4}_{001} = M_{001}4_{001}$.

For some SGs it is not possible to choose an origin, such that all point group symmetries can be written with full lattice translations as their translational parts. Depending on the convention, at least one symmetry will always carry a fractional translation in addition to the point group operation acting on the coordinates. Such a symmetry is called off-centered and the translation applied after the point group symmetry will be added to its symbol. For example, the two perpendicular rotations with non-crossing invariant axis in SG 17 can be given as $2_{100}(0, 0, 0)$, transforming a point $(x, y, z) \rightarrow (x, -y, -z)$, and $2_{010}(0, 0, \frac{1}{2})$, which acts on a point according to $(x, y, z) \rightarrow (-x, y, -z + \frac{1}{2})$. For a different origin choice, the two symmetries could also be written as $2_{100}(0, 0, -\frac{1}{2})$ and $2_{010}(0, 0, 0)$.

Nonsymmorphic symmetries

Another type of symmetry, that can appear in SGs are nonsymmorphic symmetries. Similar to off-centered symmetries, they consist of point group operations combined with a fractional lattice translations. In contrast to off-centered symmetries, they leave no point invariant and the fractional translation cannot be transformed away. For rotations, the translation must be along the rotation axis and such a symmetry is called a screw rotation. To be compatible with the lattice, an n -fold rotation can only be paired with a fraction translation that is a multiple of $\frac{1}{n}$. An example is the third rotation in SG 17, which can be obtained by applying the two perpendicular rotations from the previous paragraph. For both origin choices, the resulting symmetry reads $2_{001}(0, 0, \frac{1}{2})$. A mirror symmetry is nonsymmorphic, if it is followed by a translation of half a lattice vector within the invariant plane, e.g., $M_{001}(\frac{1}{2}, 0, 0)$. A nonsymmorphic reflection is also called a glide mirror symmetry and has no invariant points.

The crystallographic point group is the set of all symmetries in a SG with their translational components removed. The 230 SGs can be classified in 32 crystal systems according to their crystallographic point groups.

2.1.2 Group action on a Hamiltonian

A spatial symmetry $\{R_i|\mathbf{t}\}$ with point group part R_i and translational part \mathbf{t}_i acts on a Bloch Hamiltonian $H(\mathbf{k})$ in an orthonormal basis for the \mathbf{k} -space according to

$$U_i(\mathbf{k})H(\mathbf{k})U_i^\dagger(\mathbf{k}) = H(R_i\mathbf{k}). \quad (2.1.8)$$

The crystal momentum transforms only under the point group part, while the translational part leaves the Bloch Hamiltonian invariant, see Appendix A for a derivation. All symmetries leaving \mathbf{k} invariant up to a reciprocal lattice translation, $R_i\mathbf{k} = \mathbf{k} + \mathbf{K}$, form a subgroup called the little group of \mathbf{k} . Lattice translations are elements of every little group and the little groups with maximal symmetry are identical to the SG of the system. The little group of the point $\mathbf{k} = \Gamma = (0, 0, 0)$ is always the full SG and all translation eigenvalues are +1, i.e., they do not matter for the group structure and the little group representations of all SGs with the same crystallographic point group are identical. The remaining symmetries that are not elements of the little group map \mathbf{k} to finitely many symmetry-related momenta with the same little group, called the star of \mathbf{k} .

2.1.3 Double space groups

Since electron band structures are built from fermions, the transformation properties of spinors has to be taken into account in representations acting on wave functions. Three dimensional spinors transform under $SU(2)$, which forms a double cover of $SO(3)$. In terms of the 2x2 Pauli matrices σ_i , $i \in \{x, y, z\}$ and the identity σ_0 , a rotation by an angle Θ around an axis \mathbf{e} acts in spin space as $U = \exp(-i\frac{\Theta}{2}\mathbf{e} \cdot \boldsymbol{\sigma})$. Consequently, spinors acquire an additional minus sign under 2π rotations. Under a reflection with surface normal \mathbf{e} , spinors transform as pseudo-vectors. The reflection acts in spin space via $U = -i\mathbf{e} \cdot \boldsymbol{\sigma}$ and squares to $-\sigma_0$. Lastly, spinors are invariant under inversion, which acts as σ_0 .

The transformation properties of spinful states can be included in the group structure by introducing an additional symmetry \bar{E} , corresponding to

a rotation by 2π . It commutes with every other symmetry and otherwise respects the group structure. This forms the so-called double SGs, since every spatial symmetry operation appears once in combination with \bar{E} and once without. Additionally, the relation $\bar{E}^2 = 1$ needs to be defined, i.e., the full rotation is its own inverse. A n -fold rotation N fulfills $N^n = \bar{E}$ and mirror symmetries $M^2 = \bar{E}$. Because \bar{E} squares to the identity, its eigenvalues are restricted to ± 1 . The irreducible representations of a SG can therefore be grouped into one of two categories, which we will call spinless and spinful representations, with $U_{\bar{E}} = +\mathbb{1}$ and $U_{\bar{E}} = -\mathbb{1}$, respectively. A spinless representation represents the element \bar{E} with the identity and thereby forgets the double group structure. These representations are relevant for bosonic systems, but also for $SU(2)$ invariant electronic systems, for example for vanishing spin-orbit coupling (SOC). In the latter case, the action of a symmetry in spin space can be removed by combining it with an appropriate $SU(2)$ rotation. Double groups allow to analyze spinful and spinless systems in a common framework using representation theory.

2.1.4 Time-reversal symmetry

In this work, we will often deal with time-reversal symmetric band structures. In contrast to spatial symmetries, time-reversal symmetry \mathcal{T} is antiunitary, that is, the inner product of arbitrary states $|a\rangle$ and $|b\rangle$ is invariant under \mathcal{T} up to complex conjugation. $\langle \mathcal{T}a | \mathcal{T}b \rangle = \langle b | a \rangle$. An antiunitary symmetry can be represented by a unitary matrix $U_{\mathcal{T}}$ and the complex conjugation operator \mathcal{K} .

In k -space, \mathcal{T} acts like inversion and a Hamiltonian invariant under \mathcal{T} has to fulfill

$$U_{\mathcal{T}}^{\dagger} H^*(\mathbf{r}) U_{\mathcal{T}} = H(\mathbf{r}), \quad (2.1.9)$$

which reads for a Bloch Hamiltonian

$$U_{\mathcal{T}} H^*(\mathbf{k}) U_{\mathcal{T}} = H(-\mathbf{k}), \quad (2.1.10)$$

as shown in Appendix A. A time-reversal invariant crystal momentum (TRIM)

fulfills $\mathbf{k} = -\mathbf{k} + \mathbf{K}$ for some reciprocal lattice vector \mathbf{K} .

\mathcal{T} commutes with all spatial symmetries and any combination of a spatial symmetry R_i of a SG and \mathcal{T} is also part of the symmetry group, which will be written as the combination without introducing a new symbol. The groups with symmetry elements $\{R_i\} + \mathcal{T}\{R_i\}$ are the so-called gray groups of the magnetic space groups, representing paramagnetic phases without any magnetic order. The equivalent to matrix representations for symmetry groups consisting of unitary and antiunitary symmetries are Wigner's corepresentations, where all antiunitary symmetries are represented by unitary matrices followed by the complex conjugation operator \mathcal{K} and all unitary symmetries by unitary matrices. In double SGs, \mathcal{T} squares to the 2π rotation, $\mathcal{T}^2 = \bar{E}$.

2.2 Fibre bundles

The Hilbert spaces of Bloch Hamiltonians $H(\mathbf{k})$ can be treated in the formalism of a Hilbert bundle over the BZ. In this chapter we will recapitulate the concept of fibre bundles with this concrete application in mind and introduce the Berry connection in this context.

Conceptually, fibre bundles are manifolds, that locally look like the direct product of two differentiable manifolds. Formally, a fibre bundle E consists of [44]:

1. a base manifold M and a projection $\pi : E \rightarrow M$,
2. a fibre F , which is also a manifold,
3. a Lie group acting on the fibre $G : F \rightarrow F$, called structure group
4. an open covering $\{V_i\}$ of M , together with local trivializations $\phi_i : V_i \times F \rightarrow \pi^{-1}(V_i)$, such that $\pi \circ \phi_i(p, f) = p \forall p \in V_i, f \in F$,
5. transition functions $t_{ij} : V_i \cap V_j \rightarrow G$, defined via $t_{ij}(p) = \phi_i(p, \cdot)^{-1} \circ \phi_j(p, \cdot) \in G$.

Here, we will use this concept to describe the Hilbert spaces of Bloch Hamiltonians $H(\mathbf{k})$ for each point in the BZ as a parameter space [7]. More specifically, we identify

1. the BZ or a sub-manifold in k -space as the base manifold,
2. Hilbert spaces $\mathcal{H}_{\mathbf{k}}$ with finite dimension d as the fibres,
3. the unitary group $U(d)$ as the structure group,
4. a cover of open sets in the BZ with a smooth basis choice $\psi_i(\mathbf{k})$ as the local trivialization,
5. basis and gauge transformations as the transition functions $U_i(\mathbf{k}) \in U(d)$

In the special case of a one-dimensional Hilbert space, the structure group $U(1)$ represents the gauge freedom of quantum states. The assignment of a quantum state to a vector in the BZ, $\mathbf{k} \rightarrow \psi(\mathbf{k}) \in \mathcal{H}_{\mathbf{k}}$, is called a section. A basis and gauge choice in this language corresponds to a choice of sections, that span the Hilbert spaces $\mathcal{H}_{\mathbf{k}}$. A connection is a differential operator ∇ acting on sections, whose values are one-forms, i.e., co-vectors. It defines the notion of parallel transport of a tangent vector along a curve in the base manifold. This provides a unique way of lifting a path $\gamma(t)$ in the base manifold M to a path $\tilde{\gamma}(t)$ in the fibre bundle E from a given starting point $\psi(\mathbf{k} = \gamma(0))$ by solving the linear differential equation $\nabla_{\frac{\partial \gamma(t)}{\partial t}} \psi = 0$. The projection of the lifted path reproduces the initial path, $\pi(\psi(\gamma(t))) = \gamma(t)$, and the lifting respects composition laws for paths [7].

For all band structures induced from Wannier functions $\phi_\alpha(\mathbf{R}_i + \mathbf{r})$ with some internal index $\alpha = 1, \dots, d$ a smooth basis choice for the whole BZ can be chosen in terms of Bloch waves $\psi_\alpha(\mathbf{k}) = \sum_i e^{i\mathbf{k}\mathbf{R}_i} \phi_\alpha(\mathbf{R}_i + \mathbf{r})$. This makes it a trivializable bundle, i.e., it is isomorphic to the direct product $E = \text{BZ} \times \mathcal{H}_0$. Concretely speaking, a band representation induced from a site-symmetry group representation of a Wyckoff position is trivial in the basis, where the basis vectors correspond to site-symmetry representations. This is often also just called the orbital basis. Conversely, trivializable Hilbert

bundles which respect SG symmetries form band representations and can be decomposed into its elementary band representations (EBR) [45, 46]. In this case, there is a preferred trivial connection and a path can be lifted according to $\gamma(t) \rightarrow (\gamma(t), \psi_0) \forall t$.

A topologically more interesting situation is found in projected Hilbert bundles. According to the Serre-Swan theorem, every finite-dimensional Hilbert bundle is isomorphic to a projected subbundle of some finite rank trivial Hilbert bundle [47, 48]. The fibers in a projected Hilbert bundle \mathcal{V} are spanned by a subset of basis vectors $\{\psi_\alpha(\mathbf{k})\}$, $\alpha < d$, forming a sub-bundle \mathcal{V} . For topological insulators, the projection is into the subset of occupied states, using the projector $P(\mathbf{k}) = \Theta(E_{\text{gap}} - E(\mathbf{k}))$. This requires a well defined gap in the spectrum and bands that are either fully occupied and thus part of the projected bundle or not. In the context of topology and in this thesis, occupied bands therefore often refers to an integer number of bands below a possibly dispersive gap $E_{\text{gap}}(\mathbf{k})$. The position of the actual Fermi energy and the overall dispersion is for example irrelevant for the question of surface states in a gap separating two sets of bands, as long as the separation of bands above and below the gap is locally well defined for all \mathbf{k} . Even when starting from a trivial connection of the full Hilbert bundle \mathcal{H} , with $\nabla^{\mathcal{H}} |v_i\rangle = 0$ for all basis vectors $|v_i\rangle$, the projected Berry connection $\nabla^{\text{Berry}} = P \circ \nabla^{\mathcal{H}} \circ I$ defined on the projected Hilbert bundle \mathcal{V} is not necessarily trivial [7]. The distinction of valence and conductance bands is therefore an essential ingredient for getting topological nontrivial phase in band structures induced from Wannier functions.

2.3 Nodes and their invariants

The distinction of bands in occupied and unoccupied breaks down at band crossings or band touching points. The topology of semimetals is instead characterized on a subset of the BZ without gap closing points. Depending on the dimensionality d of the system and manifold of degenerate points, the subset resembles a lower-dimensional topological insulator. The topological invariant can then be evaluated on a closed manifold with dimension $D =$

$d - d_{\text{defect}} - 1$, which encloses the whole degeneracy and on which there is a well defined gap [49, 14]. In this work, we mainly deal with three-dimensional systems, $d = 3$ with point and line defects. Their invariants are line and surface integrals, evaluated on circles S^1 and spheres S^2 , respectively.

2.3.1 Berry phase

The Berry phase is the integral of the Berry connection $\mathcal{A}_i(\mathbf{k}) = \langle \psi_{\mathbf{k}} | \partial_{k_i} | \psi_{\mathbf{k}} \rangle$ on a closed loop and can characterize point defects in two-dimensional and line defects in three-dimensional systems. The Berry connection is not a gauge invariant quantity. For a differentiable gauge transformation $|\psi'_{\mathbf{k}}\rangle = e^{i\phi_{\mathbf{k}}} |\psi_{\mathbf{k}}\rangle$, we find

$$\mathcal{A}'(\mathbf{k}) = -i \langle \psi_{\mathbf{k}'} | \nabla_k | \psi'_{\mathbf{k}} \rangle = -i \langle \psi_{\mathbf{k}} | \nabla_k | \psi_{\mathbf{k}} \rangle + \nabla_k \phi_{\mathbf{k}} \quad (2.3.1)$$

However, in an integral along a path in the BZ the additional factor depends only on the endpoints and always vanishes for closed loops. In the presence of certain symmetries, the Berry phase of loops is restricted to a discrete set of values. A system is topological, if its holonomy group is not trivial, i.e., if there are paths in the Brillouin zone, for which the Berry phase is nonzero.

Evaluating the Berry phase numerically poses additional challenges, as it can only be done on discrete steps and there is no smooth phase convention for the eigenstates of the Hamiltonian. A solution to both problems is presented in the Wilson loop formalism, in which the Berry phase is expressed as a product of projection operators [50]. The discretized Wilson loop matrix is defined via the product of projectors onto the subspace of occupied states at intermediate points \mathbf{k}_n , $n = 1, \dots, N - 1$ along the path,

$$(\mathcal{W}_\gamma)_{ij} = \langle u_{\mathbf{k}_0}^i | \prod_{n=1}^{N-1} \left(\sum_l |u_{\mathbf{k}_n}^l\rangle \langle u_{\mathbf{k}_n}^l| \right) | u_{\mathbf{k}_N}^j \rangle \quad (2.3.2)$$

$$= \left(\prod_{n=0}^{N-1} S_n \right)_{ij} . \quad (2.3.3)$$

In the last step we introduced the overlap matrices

$$(S_n)_{ij} = \left\langle u_{\mathbf{k}_n}^i \left| u_{\mathbf{k}_{n+1}}^j \right. \right\rangle. \quad (2.3.4)$$

Note that the multiplication of states for different \mathbf{k} is only defined for a trivial connection on the bundle. Otherwise the vectors would first need to be parallel transported to the same Hilbert space.

The exponential of the path-ordered, multi-band Berry phase integral can be rewritten in terms of infinitesimal discrete steps,

$$\begin{aligned} \mathcal{P} \exp \left(i \int_{\gamma} \mathcal{A}(\mathbf{k}) \cdot d\mathbf{l} \right) &\approx \mathcal{P} \exp \left(i \sum_{i=0}^{N-1} \mathcal{A}(\mathbf{k}_i) \cdot (\mathbf{k}_{i+1} - \mathbf{k}_i) \right) \\ &= \mathcal{P} \prod_{i=0}^{N-1} \exp(i\mathcal{A}(\mathbf{k}_i) \cdot (\mathbf{k}_{i+1} - \mathbf{k}_i)) \\ &= \mathcal{P} \prod_{i=0}^{N-1} \frac{S_i}{\sqrt[N]{|\det S_i|}} \end{aligned} \quad (2.3.5)$$

In the last step, we expanded the exponential,

$$\begin{aligned} (e^{i\varepsilon\mathcal{A}_\alpha})_{ij} &\approx \frac{\delta_{ij} + i\varepsilon(\mathcal{A}_\alpha)_{ij}}{|\det(1 + i\varepsilon\mathcal{A}_\alpha)|^{1/d}} \\ &= \frac{\delta_{ij} + \left\langle u_{\mathbf{k}}^i \left| u_{\mathbf{k}+\varepsilon\hat{\mathbf{e}}_\alpha}^j \right. \right\rangle - \left\langle u_{\mathbf{k}}^i \left| u_{\mathbf{k}}^j \right. \right\rangle}{|\det(1 + i\varepsilon\mathcal{A}_\alpha)|^{1/d}} \\ &= \frac{\left\langle u_{\mathbf{k}}^i \left| u_{\mathbf{k}+\varepsilon\hat{\mathbf{e}}_\alpha}^j \right. \right\rangle}{|\det(1 + i\varepsilon\mathcal{A}_\alpha)|^{1/d}}. \end{aligned} \quad (2.3.6)$$

Dividing by the d -th root of the determinant preserves unitarity in the expansion and makes the expression numerically more stable, allowing fewer and coarser steps. Finally, the Berry phase P for a path γ in the multi-band case can be given in terms of the Wilson loop, $P = \text{Tr} \int_{\gamma} \mathcal{A} \cdot d\mathbf{l} = i \log(\det(\mathcal{W}_\gamma))$.

2.3.2 Berry curvature

The Berry curvature is the curl of the Berry connection, $\mathcal{F} = \nabla \times \mathcal{A}$, and is gauge invariant. The Berry curvature transforms like a pseudovector un-

der spatial symmetries, i.e., it is transformed by rotations, but remains unchanged by reflections and inversion. Time-reversal symmetry however inverts its sign. Therefore, the Berry curvature vanishes identically in \mathcal{PT} -symmetric band structures. The integral of the Berry curvature over a two-dimensional (sub-)manifold, e.g., a slice of the BZ or a sphere around a degenerate point gives the Chern number or Thouless-Kohmoto-Nightingale-Nijs (TKNN) invariant [16]. On a closed, orientable surface, the integral of the Berry curvature corresponds to the integral over the first Chern character [51, 44] and evaluates therefore always to an integer [16, 12].

For numeric evaluations, we can make use of Stokes' theorem and evaluate the flux through a finite patch of the integration surface via a line integral of the Berry connection along its border. The total integration surface A is tiled by small patches, which can be evaluated using the discrete Wilson loop formalism on the border of each patch [52].

$$\mathcal{C} = \int \mathcal{F} dA \quad (2.3.7)$$

$$= \sum_n F_{\mu\nu}(\mathbf{k}_n) = i \log W_{\mu\nu}(\mathbf{k}_n), \quad (2.3.8)$$

with the Wilson plaquette

$$W_{\mu\nu}(\mathbf{k}_n) = U_\mu(\mathbf{k}_n) U_\nu(\mathbf{k}_n + \hat{\mathbf{e}}_\mu) U_\mu^\dagger(\mathbf{k}_n + \hat{\mathbf{e}}_\nu) U_\nu^\dagger(\mathbf{k}_n), \quad (2.3.9)$$

$$(U_\mu(\mathbf{k}))_{ij} = \langle u_{\mathbf{k}}^i | u_{\mathbf{k}+\hat{\mathbf{e}}_\mu}^j \rangle. \quad (2.3.10)$$

Here, $\hat{\mu}$ and $\hat{\nu}$ are chosen such, that they connect to the three neighboring $\mathbf{k}_{n'}$ and the whole surface is covered exactly once. This method does not depend on the tiling or the shape of the integration surface, and is robust even for a coarse tiling.

2.4 Low-energy Hamiltonians

In order to better understand the dispersion around a degeneracy and evaluate its topological invariant, we construct low-energy Hamiltonians. The

dimension of a low-energy Hamiltonian is given by the number of states involved in the degeneracy. Since we are only interested in qualitative features like the splitting of bands when moving away from the degeneracy, the models are expanded to lowest non-vanishing order in the relative momentum coordinate. In a purely symmetry based analysis, the actual energy of states at the degeneracy and their dispersion in the vicinity are not determined. Therefore, we will call the states above the gap, which is closed by the degeneracy, unoccupied and the ones below occupied. In this slight abuse of terminology, bands are always fully occupied or fully unoccupied—except for the degeneracy, where this distinction is not possible—and the gap can be simply specified in terms of the band index. The projection on only the lower bands for evaluating the topological invariant is done after diagonalizing the low-energy Hamiltonian and the topological information is captured by the winding of the occupied eigenstates on a closed surface, that contains the degeneracy.

Formally, the low-energy Hamiltonian for a degeneracy at \mathbf{k}_0 is defined on an open environment $V \ni \mathbf{k}_0$ in the base manifold of the Hilbert bundle, where a local trivialization $\phi : V \times \mathcal{H} \rightarrow E$ for the relevant bands exists. Since the low-energy Hamiltonian describes both, occupied and unoccupied bands, it is trivializable, i.e. a smooth basis choice $\{|\psi(\mathbf{q})\rangle\}$ with $\mathbf{q} = \mathbf{k} - \mathbf{k}_0 \in V$ exists. Practically, V should be small enough to avoid crossing or strong hybridization with other bands.

A trivialization is then chosen such, that the matrix representations of the little group are constant over V . Concretely, for every symmetry in the little group with matrix representation U_i , we find

$$U_i H(\mathbf{q}) U_i^\dagger = H(R_i \mathbf{q}). \quad (2.4.1)$$

The use of the relative coordinate \mathbf{q} in this equation is justified, because \mathbf{k}_0 is invariant under the symmetries of the little group by definition. Including all symmetry-allowed terms in the Hamiltonian, one can then make qualitative statements about the dispersion in the vicinity of the degeneracy.

Mostly we are interested in the splitting of bands away from the degeneracy and the topological invariants, which are not sensitive to an overall dispersion, encoded in a term proportional to $\mathbf{1}$. Neglecting this term leaves us with the gap Hamiltonian. In the two-band case, the gap Hamiltonian can conveniently be written using the Pauli matrices σ_i (or τ_i), $i \in x, y, z$,

$$H_{\text{gap}}(\mathbf{q}) = \mathbf{d}(\mathbf{q}) \cdot \boldsymbol{\sigma}. \quad (2.4.2)$$

The real vector components $d_i(q)$ contain the momentum dependence and the degeneracy is found for all q with $d_i(q) = 0$ for all three components.

All elements \mathbf{k}_i in the star of \mathbf{k}_0 have the same little group. A matrix representation for the SG can be given for the entire star. The matrix representation of all little group symmetries will be block diagonal with respect to the elements of the star. The remaining symmetries are off-diagonal and determine, which little group representations at symmetry-related \mathbf{k}_i can be combined. They further relate the low-energy Hamiltonians expanded around each \mathbf{k}_i .

3. Symmetry-enforced nodes

In this chapter we will discuss symmetry-enforced topological band crossings. The degeneracy of these band crossings is enforced by symmetry and their topology can be determined from the symmetry allowed terms in the low-energy Hamiltonian evaluated in their vicinity.

In a collaborative effort, we performed a systematic search for all symmetry-enforced degenerate points, lines and planes in time-reversal symmetric orthorhombic and tetragonal SGs with SOC. The primary result of this search are comprehensive tables for all SGs, presented in references [53, 54] and in Appendix B. For the orthorhombic SGs, spinless band structures were considered as well. More precisely, we also included irreps with $U_{\bar{E}} = +1$ as defined in Sec. 2.1.3. These are relevant for bosonic band structure and electronic band structures with negligible SOC. In the latter case, spin degrees of freedom exist, but the system is invariant under spin rotations with symmetry group $SU(2)$ and the action of symmetries on spinors can be undone by combining them with properly chosen $SU(2)$ transformations. We will present the different types of degeneracies, explain how symmetries enforce them and calculate their topological invariants.

Our analysis contains topological band crossings pinned to points, lines or planes with higher symmetry, that can be understood in terms of their little groups. More importantly, we also identified all crossings enforced by compatibility relations of bands between high-symmetry points. These crossings cannot be found from the analysis of local little groups alone and they are free to move on an axis or within a plane, therefore they are called movable. For the point and line degeneracies, we derived low-energy Hamiltonians based on the little group of the degeneracy. The low-energy Hamiltonians

provide insight on how the different symmetries lead to degeneracies and how symmetry breaking affects them. Furthermore, they can be used for the evaluation of the topological invariants, often times analytically. Knowing that all topological charges within the same gap need to add up to zero [33], we can identify the charges of extended band crossings like nodal planes by summing up all other contributions in the same gap.

Material search

For the most interesting SGs, we performed a systematic search in databases of known compounds to identify material examples, consisting of an automated screening followed by manual inspection of the phases passing the first round. As a starting point, we include all materials that are found both in the Materials Project (MP) [55, 56] and the Inorganic Crystal Structure Database (ICSD) [57, 58]. The MP provides an API [59] and allows to apply further selection criteria to narrow down the results. The goal of preliminary screening is to reduce the number of results for further manual inspection, while maximizing the chance of finding well resolved band crossings close to the Fermi energy. Depending on the total available number of reported phases in a SG, which range from zero up to 1400 for the examples investigated here, the following criteria can be loosened or used for sorting the results. The first criteria is the thermodynamic stability of the reported structure and we require a formation energy of $\leq 50\text{meV}$ off the convex hull. Since we are interested in band crossings close to the Fermi energy, we reject phases with a reported band gap¹ above a certain threshold, depending on the availability of phases. In order to exclude materials with a high structural complexity, we place an upper limit of 50 atoms per primitive unit cell, as very large unit cells often lead to flat bands and crowded band structures. Finally, if the desired band crossing relies on spin split bands from SOC, we require heavier elements ($Z \geq 49$) to be present. In a more refined step we use the orbital projections in the DOS of a certain energy window around the

¹In the high-throughput calculations of the MP, the band gap is calculated using a generalized gradient approximation functional, which often underestimates the band gap. For the elimination of insulators, this is of minor importance here.

Fermi energy and place a lower limit on the relative weight of heavy element orbitals.

The band structures of the candidates passing the primary selection can then be inspected for band crossings in the band structures on high-symmetry lines from the high-throughput calculations in the databases [60, 61]. Although the symmetry-enforced band crossings must exist in every set of bands in a given SG, they might not be resolved at a relevant energy scale. Furthermore, the bands involved in the crossing might show too large of a dispersion or there might be other trivial bands at the same energies, both of which can obscure the crossing and mask its effect on observable quantities. Understanding the pairing mechanism based on SG symmetries beforehand is crucial to correctly identify the dimension and topological nature of a crossings in the band structure plots along high-symmetry paths [62], as a crossing on a section might be a true point crossing or part of a nodal line. In a similar manner, nodal planes and degenerate lines are not distinguishable in the plots of the high-symmetry path alone.

3.1 Weyl points

Weyl fermions are real solutions of the massless Dirac equation first described by Weyl [63],

$$\sigma^\mu \partial_\mu \Psi = 0. \quad (3.1.1)$$

In condensed matter systems, a Weyl point is a pointlike degeneracy with a linear dispersion [64], which can be described locally by a low-energy Hamiltonian up to linear order in the relative momentum \mathbf{q} of the form

$$H(\mathbf{q}) = \sum_{i=x,y,z} (v_i q_i) \sigma_i. \quad (3.1.2)$$

The real factors v_i allow for anisotropic group velocities in each direction $i = x, y, z$. The Chern number of this Weyl point, evaluated on a closed surface surrounding $\mathbf{q} = 0$ is $\mathcal{C} = \prod_i \text{sgn}(v_i) \in \{+1, -1\}$. The Chern number remains unchanged when varying the velocities as long as the gap on the

enclosing surface is preserved, i.e., $v_i \neq 0, \forall i$. In the same way, the Chern number is preserved when higher-order terms are introduced smoothly while leaving the gap open.

The Chern numbers of two Weyl points related by proper rotations and time-reversal symmetry are identical, while improper rotations like inversion flip the sign of the Chern number. This follows directly from the transformation properties of the Berry curvature and can also be verified from the matrix representations of the star in a given SG.

3.1.1 Weyl points at high-symmetry points

A Weyl point at a high-symmetry point \mathbf{k}_0 can be completely understood from the invariance of the low-energy Hamiltonian under the little group of \mathbf{k}_0 . A twofold degeneracy is necessary, but not sufficient, since it might be part of a line or plane. In that case, the Chern number cannot be evaluated on an enclosing two-dimensional closed manifold, even though the whole node might still carry a nodal charge, see Sec. 3.4. The behavior of bands in the vicinity of the degeneracy can be understood in terms of a low-energy Hamiltonian respecting the symmetries of the little group.

Kramers theorem ensures a twofold degeneracy at all TRIMs in time-reversal symmetric spinful band structures. Invariance under \mathcal{T} restricts the gap Hamiltonian up to linear order in \mathbf{q} to the form

$$H(\mathbf{q}) = \mathbf{q}^T \cdot V \cdot \boldsymbol{\sigma}, \quad (3.1.3)$$

with a real valued velocity matrix V . Without fine-tuning, this matrix is in general diagonalizable by a proper choice of coordinates and Pauli matrices, thereby reproducing a Weyl point as defined in Eq. (3.1.2) with Chern number $\mathcal{C} = \pm 1$, called Kramers Weyl points [65, 66].

Usually, the little groups of TRIMs contain spatial symmetries as well. These symmetries restrict the entries in V . In case of mirror symmetries, roto-inversions or inversion, the degeneracy at the TRIM belongs to an extended degeneracy and no Chern number can be assigned. Chiral little groups lead in general to odd Chern numbers [65], but the inclusion of higher-order terms

might be needed to accurately describe the gap in the case of larger Chern numbers. Screw rotations in combination with \mathcal{T} enforce nodal planes for some TRIMs, which hide the point degeneracy, as we will discuss in Sec. 3.4.

In conclusion, Kramers Weyl points can be found in all chiral SGs, but also in non-primitive lattices of non-chiral SGs, where some TRIMs can have chiral little groups. For example, in the orthorhombic SG 35, the TRIMs S and R are not in mirror planes and their little group is generated by \mathcal{T} and 2_{001} .

Kramers theorem requires the representation of \mathcal{T} to square to -1 and is therefore not applicable for spinless band structures. Here we will present an alternative mechanism for creating Weyl points based on spatial symmetries alone, which works in spinless and spinful band structures. We consider three orthogonal off-centered twofold rotations, as found for example in SG 24. The rotation matrices of twofold rotations are diagonal and commute, whereas their spinor representations anticommute. Including the translational components of the off-centered rotations, we find the commutation relation [54]

$$2_{100}(0, 0, \frac{1}{2}) \cdot 2_{001}(0, \frac{1}{2}, 0) = \bar{E}t(0, -1, 0) \cdot 2_{001}(0, \frac{1}{2}, 0) \cdot 2_{100}(0, 0, \frac{1}{2}). \quad (3.1.4)$$

There are three points in the BZ of orthorhombic body-centered lattices with these three rotations in the little group, of which only $W = (\pi, \pi, \pi)$ has translation eigenvalue -1 for the above translation by one lattice constant in the conventional cell. Consequently, the spinless representations ($U_{\bar{E}} = 1$) of the rotations $U_{2_{001}}$ and $U_{2_{100}}$ anticommute and must therefore be at least two-dimensional. For an eigenstate $|\pm\rangle$ of $U_{2_{001}}$ with eigenvalue ± 1 we can write explicitly

$$U_{2_{001}}U_{2_{100}}|\pm\rangle = -U_{2_{100}}U_{2_{001}}|\pm\rangle = \mp U_{2_{100}}|\pm\rangle, \quad (3.1.5)$$

which implies that for example $|+\rangle$ and $U_{2_{100}}|+\rangle$ have different 2_{001} eigenvalues and must therefore be orthogonal. Because the Hamiltonian commutes with both, $U_{2_{001}}$ and $U_{2_{100}}$, the two states must furthermore be degenerate.

The same argument holds also for all spinful representations with little group 222 at Γ in any lattice, where translation eigenvalues are always 1.

A two-dimensional representation for the three anti-commuting twofold rotations can be given by $U_{2_{001}} = \sigma_z$, $U_{2_{100}} = \sigma_x$ and $U_{2_{010}} = i\sigma_y$, of which the last one squares to -1 . The low-energy Hamiltonian up to linear order invariant under these symmetries is of the form (3.1.2) and describes therefore a Weyl point with $\mathcal{C} = \pm 1$. This mechanism does not rely on time-reversal symmetry and holds equally in its absence. In our systematic analysis, the point W in SG 24 is the only instance of a symmetry-enforced Weyl point at a high-symmetry point in spinless band structures of orthorhombic SGs.

3.2 Higher-order point crossings

Higher order point crossings are made up from more than two bands or carry Chern numbers of a larger multiplicity. Among these are higher-order Weyl points, which are twofold pointlike band crossings with an integer Chern number $\pm n$ with $n \geq 1$. A model can be given via a generalization² of the definition in Eq. (3.1.2),

$$H_{\pm n}(\mathbf{q}) = (q_x \pm iq_y)^n \sigma_- + (q_x \mp iq_y)^n \sigma_+ + q_z \sigma_z, \quad (3.2.1)$$

where all anisotropies have been absorbed into the definition of q_i , and a gauge has been chosen, such that the signs in front of q_x and q_z are all positive. The Chern number of such a point degeneracy is $\mathcal{C} = \pm n$. The dispersion is linear along the q_z axis and of order q^n in the plane perpendicular to it. This model is rotationally invariant around the q_z -axis, and the off-diagonal terms must transform according to the ratio of rotation eigenvalues of the states on the axis.

² This is however not the most general form of a higher-order Weyl point. In the cubic SGs 207–214 and time-reversal symmetric SGs 195–199, there is a spinless representation at Γ creating a Weyl point with quadratic and cubic dispersion, but $\mathcal{C} = \pm 4$ [67, 68], enforced by the twofold and threefold rotations with non-orthogonal axes. The low-energy Hamiltonian in this case is $H(\mathbf{q}) = q_x q_y q_z \sigma_z + (q_z^2 - \frac{1}{2}(q_x^2 + q_y^2))\sigma_x - \frac{\sqrt{3}}{2}(q_x^2 - q_y^2)\sigma_y$.

3.2.1 Double Weyl points

Double Weyl points are the special case $n = \pm 2$ of a higher-order Weyl point and consequently their Chern number is $\mathcal{C} = \pm 2$. The dispersion to lowest order is linear along one axis and quadratic in directions perpendicular to it [69], as shown in Fig. 3.1(a). In spinless band structures, they can be found at TRIMs, when \mathcal{T} pairs non-real eigenvalues of three-, four- and sixfold rotations [66].

In the following, we will focus on fourfold rotations found in the tetragonal SGs. A crossing on a fourfold rotation axis forms a double Weyl point, when the ratio of rotation eigenvalues of the bands is -1 . In that case, the representation of the fourfold rotation is proportional to σ_z in the rotation eigenbasis, which restricts the diagonal elements in the gap Hamiltonian to be invariant under the symmetry, while the off-diagonal elements will acquire a negative sign. With the rotation axis oriented along q_z , symmetry allowed terms up to second order are q_z and $q_x^2 + q_y^2$ in d_z , whereas the requirement for off-diagonal terms in d_x and d_y can only be realized by the combinations $(q_x + iq_y)^2$ and $(q_x - iq_y)^2$. The Chern number of such a Hamiltonian is ± 2 , where the sign is determined by the term with the dominant prefactor. Note that the special case of identical prefactors the gap is closed along a line and the Chern number is not defined.

Such a double Weyl point can be enforced at high-symmetry points in the spinless case, when \mathcal{T} pairs the fourfold rotation eigenvalue i with $-i$. This situation appears at Γ in every band structure induced from orbitals transforming like $x \pm iy$ under the fourfold rotation in their site-symmetry group. Interestingly, in chiral SGs with fourfold screw rotation $4_{001}(0, 0, \frac{\pi}{4})$, double Weyl points are enforced at TRIMs with $k_z = 0$ for $n = 1, 3$ in all possible band structures, regardless of the Wyckoff position or site symmetry group representation inducing the band structure. In the case $n = 2$, the double Weyl can be found at one TRIM on the rotation axis, either with $k_z = 0$ or π . Non-zero SOC will push the double Weyl points in each spin subspace apart and onto the rotation axis away from the TRIMs, as we will discuss in Sec. 3.3.

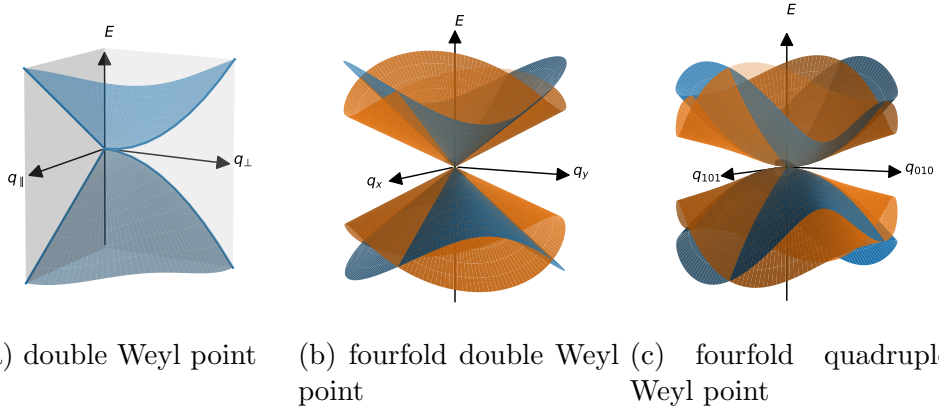


Figure 3.1: Dispersion of symmetry-enforced Weyl nodes with Chern number $|\mathcal{C}| \geq 2$. (a) A double Weyl point is a twofold degeneracy, with linear dispersion along the rotation axis q_{\parallel} and quadratic dispersion perpendicular to it, i.e., along q_{\perp} . The Chern number of a double Weyl is $C_{\text{dW}} = \pm 2$. (b) A fourfold double Weyl point is a fourfold degeneracy with linear dispersion in all directions. Along high-symmetry lines a twofold degeneracy is enforced. The colors distinguish between the two symmetry-related Weyl points. The Chern number is the sum of these two Weyl points, $C_{\text{fW}} = 2C_{\text{Weyl}} = \pm 2$. (c) The fourfold double Weyl is built from two symmetry-related double Weyl points of equal chirality, the total Chern number is $C_{\text{fdW}} = 2C_{\text{dW}} = \pm 4$. Twofold-degenerate lines in (b) and (c) are part of nodal planes (see Sec.3.4).

3.2.2 Fourfold double Weyl points

A pointlike crossing of more than two bands can also carry a larger topological charge, $|\mathcal{C}| > 1$. As a first example, we discuss a fourfold degenerate point with a Chern number of $\mathcal{C} = \pm 2$, called a fourfold double Weyl point [53, 34].

A fourfold double Weyl point is a pointlike degeneracy at the level of two occupied and two unoccupied bands. It splits into nondegenerate bands almost everywhere and the dispersion depends to lowest order linearly on the relative momentum \mathbf{q} . As we will see, some additional degeneracies remain in two-dimensional subspaces between the lower two and upper two bands. A schematic dispersion in the proximity of a fourfold double Weyl point is shown in Fig. 3.1(b). It can be understood as two Weyl points of equal chirality, which are pinned to the same high-symmetry point by an additional symmetry. Hence, they are also referred to as double-spin-1/2 Weyl points [34]. The Chern number prevents the Weyl point from being gapped by small perturbations of any kind, but perturbations breaking one of the symmetries relevant for the fourfold degeneracy can separate the two Weyl points in energy or k -space and move them away from the high-symmetry point.

Two different mechanisms need to be at play simultaneously to enforce such a feature. First, the representations of the three twofold rotations at a TRIM need to anticommute and thereby enforce a twofold degeneracy in orbital space, formed by the pairing of the two different rotation eigenvalues. Secondly, an antiunitary symmetry is required, which pairs identical eigenvalues of at least one rotation.

In spinful band structures, \mathcal{T} ensures a Kramers partner of the same eigenvalue, if the eigenvalue is purely real, i.e, ± 1 . These conditions are met at some TRIMs for the twofold rotations in the orthorhombic SGs 18 (S,R) and 19 (S,T,U), and in the tetragonal SGs 90, 94 (M,A) and 92, 96 (M,R). We illustrate this mechanism in more detail for the TRIM S in SG 18. In this SG the symmetries \mathcal{T} , $2_{100}(\frac{1}{2}, \frac{1}{2}, 0)$ and $2_{010}(\frac{1}{2}, \frac{1}{2}, 0)$ create the little group of all TRIMs. A direct evaluation shows the relation

$$2_{100}(\frac{1}{2}, \frac{1}{2}, 0) \cdot 2_{010}(\frac{1}{2}, \frac{1}{2}, 0) = \bar{E}t(1, -1, 0) \cdot 2_{010}(\frac{1}{2}, \frac{1}{2}, 0) \cdot 2_{100}(\frac{1}{2}, \frac{1}{2}, 0). \quad (3.2.2)$$

At the TRIMs S and R, the eigenvalue of the translation is +1 and we find $U_{2_{100}}U_{2_{010}} = -U_{2_{010}}U_{2_{100}}$ in spinful representations with $U_{\bar{E}} = -1$. Applying $U_{2_{010}}$ to a state with a positive 2_{100} eigenvalue results in a new state with negative eigenvalue and vice versa. As shown in Sec. 3.1.1, this requirement alone leads to a Weyl point with chirality $|\mathcal{C}| = 1$ [66]. Because $2_{100}(\frac{1}{2}, \frac{1}{2}, 0)$ is a screw rotation squaring to the translation $\bar{E}(1, 0, 0)$, its eigenvalues are the square roots of the translation eigenvalue times the \bar{E} eigenvalue. At R and S one finds $\pm ie^{ik_x/2}|_{k_x=\pi} = \mp 1$. Kramers partners therefore share the same symmetry eigenvalue. Labeled in terms of 2_{100} -eigenvalue signs, we therefore find the quadruple degeneracy $(+, +, -, -)$. Since the chiralities of two Weyl points related by \mathcal{T} are identical, they add up to ± 2 .

A matrix representation for a little group fulfilling the above can be written in terms of the 4×4 matrices

$$U_{2_{100}} = \sigma_0 \otimes \tau_x, \quad (3.2.3)$$

$$U_{2_{010}} = \sigma_0 \otimes \tau_y, \quad (3.2.4)$$

$$U_{2_{001}} = i\sigma_0 \otimes \tau_z, \quad (3.2.5)$$

$$U_{\mathcal{T}}\mathcal{K} = i\sigma_y \otimes \tau_x\mathcal{K}. \quad (3.2.6)$$

The Pauli matrices σ_i and τ_i ($i = 0, x, y, z$) act in spin and orbital space, respectively. The low-energy Hamiltonian around the invariant point \mathbf{K} can be given, up to linear order in relative coordinates $\mathbf{q} = \mathbf{k} - \mathbf{K}$, as

$$\begin{aligned} H(\mathbf{q}) = & v_x q_x \sigma_z \otimes \tau_x + v_y q_y \sigma_z \otimes \tau_y + v_z q_z \sigma_0 \otimes \tau_z \\ & + \lambda_x q_x \sigma_x \otimes \tau_x + \lambda_y q_y \sigma_x \otimes \tau_y, \end{aligned} \quad (3.2.7)$$

with the real parameters v_i and λ_i . The velocities v_i describe the slope of the dispersion of the individual Weyl points. Without SOC, the first three terms would be uncoupled and all bands twofold degenerate. The terms with parameters λ_i result from non-vanishing SOC and remove the overall twofold degeneracy. In the tetragonal SGs, the same situation can be found, but there is an additional fourfold rotation symmetry present at some TRIMs, which further requires $|v_x| = |v_y|$ and $|\lambda_x| = |\lambda_y|$. Using the unitary transformation

$U = \frac{1}{\sqrt{2}}(\sigma_z \otimes \tau_0 + \sigma_y \otimes \tau_z)$, we can bring the Hamiltonian into block diagonal form with the two blocks

$$H_{\pm}(\mathbf{q}) = (\pm v_x q_x - \lambda_y q_y) \tau_x + (\pm v_y q_y - \lambda_x q_x) \tau_y + v_z q_z \tau_z. \quad (3.2.8)$$

The Chern number can be evaluated for each block separately and the colors in Fig. 3.1(b) mark the bands of each block. In the planes $q_x = 0$ and $q_y = 0$, the different signs do not matter for the dispersion and a state from one block becomes degenerate with a state of the other block. This degeneracy in planes is enforced by the presence of time-reversal symmetry together with twofold screw rotations, as we will discuss in more detail in Sec. 3.4. For this reason, a Chern number cannot be evaluated at the level of one or three filled bands.

In spinless band structures, \mathcal{T} is not enough to ensure a Kramers partner for states with real eigenvalues. The pairing of equal eigenvalues can be enforced instead by the combination of \mathcal{T} with one of the screw rotations. This situation is ensured in SG 19, and identically in SGs 92 and 96 at $\mathbf{k}_0 = (\pi, \pi, \pi)$. The principle remains the same as in the example above, with the difference that the commutation relation for the screw rotations reads

$$2_{100}(\frac{1}{2}, \frac{1}{2}, 0) 2_{010}(0, \frac{1}{2}, \frac{1}{2}) = \bar{E} t(1, -1, -1) 2_{010}(0, \frac{1}{2}, \frac{1}{2}) 2_{100}(\frac{1}{2}, \frac{1}{2}, 0). \quad (3.2.9)$$

In spinless band structures we have $U_{\bar{E}} = 1$, but the negative sign is now provided by the translation eigenvalue of $t(1, -1, -1)$ at \mathbf{k}_0 and we find again anti-commuting representations for the twofold rotations. The antiunitary symmetry $2_{001}(\frac{1}{2}, 0, \frac{1}{2})\mathcal{T}$ squares to the translation $t(0, 0, 1)$ with eigenvalue -1 at \mathbf{k}_0 and enforces therefore Kramers pairs also in the spinless case. A Kramers partner of a state with rotation eigenvalues $\pm i$ of $U_{2_{100}}$ or $U_{2_{010}}$ has the same eigenvalues, because $U_{2_{001}}$ anticommutes with both representations, $U_{2_{100}}$ and $U_{2_{010}}$, and this cancels the sign change from complex conjugation. Upon inclusion of SOC, the fourfold double Weyl point is moved to one of the rotation axis in SG 19, as will be discussed in Sec. 3.3, whereas in SGs 92 and

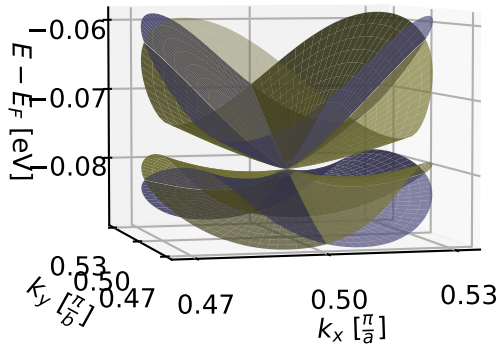


Figure 3.2: Dispersion of the fourfold double Weyl point in Pd_7Se_4 within the $k_z = 0$ plane around $S = 2\pi(\frac{1}{2}, \frac{1}{2}, 0)$. The colors indicate the two Weyl cones, related by the rotation 2_{100} or 2_{010} . The twofold degenerate lines along $(k_x, \pi, 0)$ and $(\pi, k_y, 0)$ are part of nodal planes. Figure adapted from [53].

96 it will split up into two sets of twofold degenerate bands and a fourfold quadruple Weyl point, which will be the topic of the following section.

In our systematic search for candidate materials, we found a fourfold double Weyl in Pd_7Se_4 , crystallizing in SG 18. The bands at the TRIM S are close to the Fermi energy and SOC leads to a large splitting of bands, revealing the symmetry-enforced fourfold double Weyl point, see Fig. 3.2. In contrast to the sketch in Fig. 3.1(b), the uniform parabolic dispersion of all bands is included.

3.2.3 Fourfold quadruple Weyl points

In the previous section we have shown how a fourfold double Weyl point can be made out of two single Weyl points at the same TRIM. At the TRIM $A = (\pi, \pi, \pi)$ in SGs 92 and 96 with SOC there is another fourfold degenerate point in spinful band structures, but in contrast to the fourfold double Weyl point at M it is made up from two double Weyl points. The splitting of bands is therefore also quadratic in q_x and q_y , shown in Fig. 3.1(c). As before, the Chern numbers of the two double Weyl points have to be identical by

symmetry, hence they add up to a total of $|\mathcal{C}| = 4$ [53] and we give this point the attribute quadruple. Because of the splitting into nondegenerate bands and the non-zero Chern number we do not use the name Dirac point, even though this name has been used in the literature also for this type of linearly dispersing fourfold degeneracy [70].

For each set of bands in SG 92, there are two different twofold degenerate representations and one fourfold degenerate representations at A. They result from splitting up the symmetry-enforced fourfold degeneracy from the spinless case by nonzero SOC, which amounts to eight bands when the spin degeneracy is accounted for. We proceed by labeling the states with their eigenvalues of the fourfold screw rotation $4_{001}(\frac{1}{2}, \frac{1}{2}, \frac{1}{4})$. Because applying the screw rotations four times results in a 2π rotation and a translation in z -direction, the representation has to respect $U_{4001}^4 = -e^{ik_z}$ and the eigenvalues can be labeled by

$$U_{4001} |p\rangle = e^{i(2p+1)\frac{\pi}{4}} e^{i\frac{k_z}{4}} |p\rangle, \quad (3.2.10)$$

which evaluates at A to i , -1 , i and $+1$ for $p = 0$ to 3 , respectively. In the spinful EBR of this SG every rotation eigenvalue is present twice. In the presence of \mathcal{T} , the complex eigenvalues appear in two degenerate pairs, denoted by $(0, 2)$ in terms of the label p . Through Kramers theorem, the states with real eigenvalues also get Kramers partners, but they have the same eigenvalue and the pairs are $(1, 1)$ and $(3, 3)$. A second antiunitary symmetry, the combined operation $2_{010}(\frac{1}{2}, \frac{1}{2}, \frac{1}{4})\mathcal{T}$ is then responsible for creating the fourfold degeneracy. By direct evaluation of the spatial symmetry, one finds the commutation relation

$$4_{001}(\frac{1}{2}, \frac{1}{2}, \frac{1}{4})2_{010}(\frac{1}{2}, \frac{1}{2}, \frac{1}{4})\mathcal{T} = 2_{010}(\frac{1}{2}, \frac{1}{2}, \frac{1}{4})\mathcal{T}t(1, 0, -1) [\bar{E}4_{001}(\frac{1}{2}, \frac{1}{2}, \frac{1}{4})]^3. \quad (3.2.11)$$

Consequently, a state $|p\rangle$ with rotation eigenvalue $\alpha = \exp(i\frac{\pi}{2}(p+1))$ has a Kramers partner $U_{2010}U_{\mathcal{T}}\mathcal{K}|p\rangle$ with rotation eigenvalue $-\alpha_p^{3*} = \alpha_{p'}$. In the notation (p, p') introduced above, we find the same pairing as from \mathcal{T} for the complex eigenvalues, $(0, 2)$, and the degeneracy remains twofold. The real eigenvalues on the other hand get paired as $(1, 3)$. This establishes the fourfold degeneracy for states with fourfold rotation eigenvalues ± 1 . The

chirality of a Weyl point invariant under fourfold rotations can be evaluated from the ratio of its eigenvalues and is $|\mathcal{C}| = 2$ for a ratio of -1 with quadratic dispersion perpendicular to the rotation axis [66].

To illustrate the topology of the fourfold crossing, we construct a low-energy gap Hamiltonian up to second order in $\mathbf{q} = \mathbf{k} - (\pi, \pi, \pi)$. In the basis of rotation eigenvalues, the representation for the generators of the little group reads

$$4_{001}^+, \left(\frac{1}{2}, \frac{1}{2}, \frac{3}{4}\right) : U_4 = \sigma_0 \otimes \tau_z, \quad (3.2.12)$$

$$2_{010}, \left(\frac{1}{2}, \frac{1}{2}, \frac{3}{4}\right) : U_2 = \sigma_0 \otimes \tau_y. \quad (3.2.13)$$

With this basis choice, the unitary part of the time-reversal symmetry takes the form $U_{\mathcal{T}} = i\sigma_y\tau_z$. The symmetry allowed terms are then

$$\begin{aligned} H(\mathbf{q}) = & v_x q_x q_y \sigma_z \otimes \tau_x + v_y (q_x^2 - q_y^2) \sigma_0 \otimes \tau_y + v_z q_z \sigma_z \otimes \tau_z \\ & + \lambda_x q_x q_y \sigma_x \otimes \tau_x + \lambda_z q_z \sigma_x \otimes \tau_z, \end{aligned} \quad (3.2.14)$$

with the real parameters v_i and λ_i . This Hamiltonian can be block-diagonalized with the q -independent transformation $U = \frac{1}{\sqrt{2}}(\sigma_0\tau_0 + i\sigma_x\tau_y)$. The two 2×2 blocks have the form of double Weyl points, H_{dW}^{\pm} making up the blocks,

$$H_{\text{dW}}^{\pm} = (\pm v_x q_x q_y + \lambda_z q_z) \sigma_x + v_y (q_y^2 - q_x^2) \sigma_y + (\pm v_z q_z - \lambda_x q_x q_y) \sigma_z. \quad (3.2.15)$$

The dispersion in the plane $(u + \pi, v + \pi, u + \pi)$ is shown in Fig. 3.1(c), where the colors indicate the two blocks. As for the fourfold double Weyl point, twofold degeneracies remain in the planes $q_x = 0$, $q_y = 0$ and $q_z = 0$. Apart from these nodal plane, the bands split into individual bands. In the $q_z = 0$ -plane, the gap grows quadratically. The Chern numbers of both double Weyl points are necessarily identical for both subspaces and together the Chern number of a fourfold quadruple Weyl point is $\mathcal{C} = 2\mathcal{C}_{\text{dW}} = \pm 4$.

3.3 Movable point crossings on rotation axes

A movable Weyl point is not fixed to a high-symmetry point and can therefore not be explained from the little group of its location alone. Such Weyl points can be symmetry-enforced nonetheless, when compatibility relations between representations at high-symmetry points and on the axis connecting them require an exchange of bands with different symmetry eigenvalues. The resulting band crossing is then not only protected by symmetry, but its existence is guaranteed somewhere along the axis. Since the actual position depends on free parameters of the system and is not fixed by symmetry, such a crossing is called movable.

3.3.1 Hourglass dispersion from twofold screw rotations

The simplest example of a movable Weyl point is generated from twofold screw rotations, which square to \bar{E} combined with a lattice translations in the direction of the rotation axis. Their eigenvalues are the square roots of translation eigenvalues and therefore k -dependent. For example, $2_{001}(a, b, c)$ has eigenvalues

$$U_{2_{001}} |\pm\rangle = \pm i^\zeta \exp(ik_z c) |\pm\rangle, \quad (3.3.1)$$

where c is a half integer lattice translation for a screw rotation. With the factor $\zeta = 0, 1$ we distinguish the spinless from the spinful case. Along the rotation axis the eigenvalue of each band evolves smoothly with k_z , and a state can be labeled uniquely by the sign \pm according to this definition. In lattices, where $k_z = \pi$ is equivalent to $k_z = -\pi$, e.g., all primitive lattices, a band with eigenvalue label $+$ will have acquired a phase of -1 when traversing the first BZ and is turned into a band labeled with $-$ and vice versa. Therefore, there must be at least two bands as they must exchange an odd number of times. With time-reversal symmetry, all spinful representations form Kramers pairs at TRIMs with complex conjugate rotation eigenvalues.

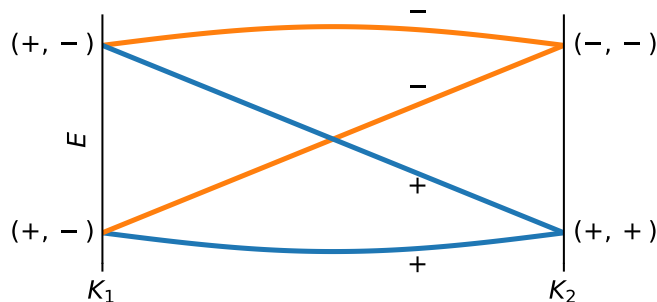


Figure 3.3: Schematic hourglass dispersion along a path between two degenerate points K_1 and K_2 along a twofold rotation axis or in a mirror plane. Colors indicate the sign of the symmetry eigenvalue of the twofold symmetry.

At $k_z = 0$, the eigenvalues $\pm i$ are paired. We label such a pair in terms of the signs $(+, -)$. At TRIMs with $k_z = \pi$ on the other hand, the eigenvalues are $\pm(-1)$ and identical eigenvalues are paired, $(+, +)$ or $(-, -)$. In total four bands are required to connect these pairs smoothly along the rotation axis and two bands with opposite eigenvalues need to exchange, leading to a so-called hourglass dispersion [71]. In Fig. 3.3 we present an illustration, where blue and orange correspond to the positive and negative label, respectively.

In the presence of inversion or when the axis rests in a mirror plane, the hourglass dispersion will be hidden within an overall twofold degeneracy on the whole axis. Without them, i.e., in all chiral SGs and screw axes with chiral little groups, the movable crossings are enforced by symmetry. We list all movable Weyl points in noncentrosymmetric orthorhombic SGs in Tables I and II and in tetragonal SGs in Table V under “points” in terms of their symmetry axis. The topological properties of movable crossings can again be determined from a low-energy Hamiltonian restricted by the symmetries of the little group. Since the degeneracy cannot be understood from local terms alone, the condition $H_{\text{gap}}(\mathbf{q} = 0) = 0$ needs to be included additionally. Knowing that the crossings have rotation eigenvalues with opposite signs, the representation can immediately given as $U_{2001} = i^\zeta \exp(ik_z c) \sigma_z$. For the twofold screw rotation, the movable Weyl point has chirality $|\mathcal{C}| = 1$ [66].

3.3.2 Accordion states from fourfold screw rotations

In a similar manner, we can construct the band connectivity for fourfold nonsymmorphic rotation symmetries $4_{001}(a, b, \frac{n}{4})$, acting on a point in space according to

$$(x, y, z) \rightarrow (-y + a, x + b, z + \frac{n}{4}) \quad (3.3.2)$$

and in spin space via $\frac{1}{\sqrt{2}}(\sigma_0 + i\sigma_z)$. Applying such a symmetry four times results again in a full lattice translation combined with \bar{E} , i.e., spinful representations acquire a negative sign. Their eigenvalues are therefore given by the fourth roots of $-\exp(ink_z)$, which we label with the integer $p \in \{0, 1, 2, 3\}$, defined through the parameterization

$$\alpha_p = \exp\left(i\frac{\pi}{4}(2p + 1)\right) \exp\left(i\frac{n}{4}k_z\right). \quad (3.3.3)$$

At the two TRIMs on the rotation axes, time-reversal symmetry \mathcal{T} pairs bands with complex conjugate eigenvalues. For $k_z = 0$, i.e., at Γ and $M = (\pi, \pi, 0)$ in primitive tetragonal lattices, we find $\alpha_0^* = \alpha_3$ and $\alpha_1^* = \alpha_2$. We label these degeneracies with $(p, p') = (0, 3)$ and $(1, 2)$, respectively. For the TRIMs with $k_z = \pi$, i.e., at $Z = (0, 0, \pi)$ and $A = (\pi, \pi, \pi)$, the three different fractional translations have to be considered separately.

For a fractional translation by a quarter of the unit cell, i.e., $n = 1$, we find $\alpha_0^* = \alpha_2 = -i$ at the other TRIM, leading to the pairing (0,2). The two real eigenvalues $\alpha_1 = -1$ and $\alpha_3 = 1$ each have a Kramers partner with the same eigenvalue, leading to the pairs (3,3) and (1,1). Connecting these pairs smoothly in k_z creates a minimum of three band crossings on the rotation axis. This pattern is called an accordion state [72, 73] and is sketched in Fig. 3.4(a). Each of these crossings is protected by different rotation symmetry eigenvalues. The screw rotation with $n = 3$ is the enantiomorphic partner symmetry and creates the same pattern, but with interchanged labels $p \rightarrow (p - 1) \bmod 4$.

For $n = 2$, that is the translation by half a unit cell with each fourfold rotation, the eigenvalues at either TRIM are purely complex. The pairing at Γ (M) remains unchanged, but at Z (A) the pairing is now (0,1) and (2,3).

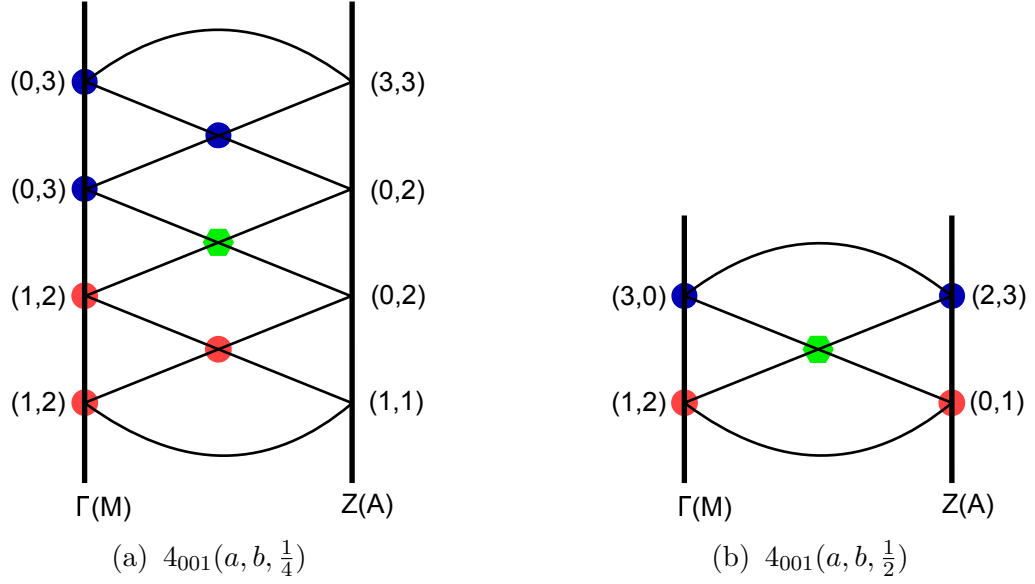


Figure 3.4: Connectivity diagrams with minimal band crossings for fourfold screw rotations. The case for a fourfold screw rotation with translational part $c = \frac{3}{4}$ along the rotation axis is identical to the case $c = \frac{1}{4}$ in (a) with redefined labels. The colored symbols indicate the chiral charge of each crossing. Blue and red dots mark chirality +1 and -1 and green hexagons indicate a double Weyl point with $\mathcal{C} = \pm 2$, where the sign cannot be determined by symmetry alone.

This allows a simpler band connectivity made up of four bands forming an hourglass dispersion with only and one band crossing along the path, see Fig. 3.4(b). The chirality C of these Weyl points at TRIMs and on the axis can be inferred from the ratio of eigenvalues involved in a crossing [66]. Fourfold screw-rotations lead to at least one movable double Weyl point with chirality ± 2 on the rotation axis, see the green hexagons in Fig. 3.4. The double Weyl points are crossings of bands with the labels $(0, 2)$ or $(3, 1)$, which directly determines the matrix representation of the fourfold rotation, $U_{4_001} = \exp(k_z \frac{n}{4}) i \sigma_z$ or $U_{4_001} = \exp(k_z \frac{n}{4}) \sigma_z$, respectively. Double Weyl points were already discussed in Sec. 3.2.1. There, we identified them at a TRIM on the rotation axis in spinless representations, e.g., at Γ . Treating SOC strength as a tunable parameter connects the two cases smoothly. For vanishing SOC, bands are spin degenerate everywhere and the Chern number

can be evaluated separately in each spin subspaces, each of which contributes $\mathcal{C}_\sigma = \pm 2$. This leads to a total Chern number of $\mathcal{C} = \mathcal{C}_\uparrow + \mathcal{C}_\downarrow = \pm 4$, because \mathcal{T} flips the spin and relates Weyl points with the same chirality. Non-zero SOC removes the spin degeneracy everywhere except on TRIMs, but far from the original degeneracy the total Chern number remains unchanged, as long as the gap remains open on an enclosing surface. The double Weyl point splits then into two movable double Weyl points at $\mathbf{K}_0 \pm \delta_z$ with respect to the TRIM \mathbf{K}_0 hosting the double Weyl point in the spinless case. As before, the double Weyl points are related by \mathcal{T} and must have the same chirality. For small SOC, they will therefore be found close to the TRIM.

3.3.3 Compatibility relations spanning several rotation axis

Previously, we have shown how nonsymmorphic rotations can enforce band crossings on a rotation axis. In the chiral SGs 19 and 24, the three perpendicular twofold rotations together impose restrictions in a way, that bands need to exchange at least once on one of the three rotation axis [74].

Movable Weyl points in spinless bands structures

As a first case, we look at spinless band structures in SG 19 with time-reversal symmetry. Because Γ is nondegenerate, there are no hourglass states enforced by the screw rotations. On the TRIMs X, Y and Z, the eigenvalues of the screw rotations $2_{100}(\frac{1}{2}, \frac{1}{2}, 0)$, $2_{010}(0, \frac{1}{2}, \frac{1}{2})$ and $2_{001}(\frac{1}{2}, 0, \frac{1}{2})$, respectively, are $\pm i$ and therefore paired by \mathcal{T} . This band crossing facilitates the exchange of bands required by each screw rotation when traversing the BZ along its rotation axis. At Γ on the other hand, all three rotation eigenvalues are ± 1 and simultaneously good quantum numbers. The representations commute and multiply to the identity, $U_{2_{100}}U_{2_{010}}U_{2_{001}} = U_{\bar{E}} = +1$. Therefore, the three eigenvalues must multiply to $+1$ in each of the nondegenerate bands. Consequently, none or exactly two of the rotation eigenvalues can be negative in a representation at Γ . Since they must evolve smoothly according to Eq. (3.3.1) and connect to the pairs $(+, -)$ at the other TRIM on their

rotation axis, all four possible combinations must exist in every set of bands. This is in agreement of the lowest possible multiplicity for Wyckoff positions, which is four, and every EBR contains all these irreducible representations at Γ , regardless of the type of point group representation used to induce it. Fulfilling these requirements requires at least one crossing on one rotation axis, protected by the different eigenvalues. In Fig. 3.5(a) we present a possible arrangement of four bands respecting these requirements. The colors blue and orange correspond to the positive and negative sign in Eq. (3.3.1), respectively and each color combination uniquely defines one of the four irreducible representations at Γ . Exchanging their order can only move the crossing to another axis, but not eliminate it. Additional crossings may only be introduced pairwise.

In the absence of additional accidental crossings, which might appear on any of the rotation axes, spinless band structures in SG 19 have only three pointlike degeneracies for $4n + 2$ filled bands and the topological charge from the two symmetry-related copies of the movable point is compensated by the fourfold double Weyl point at R discussed in Sec. 3.2.2. In Sec. 3.5.1 we provide an archetypical band structure for this SG, where this charge balance can be observed, see the blue bands in Fig. 3.7.

Next, we consider SG 24, which is one of the two nonsymmorphic space groups without nonsymmorphic symmetries. In the BZ of body-centered lattices, all three rotation axes connect Γ to Z, which has the equivalent coordinates $(0, 0, 2\pi)$, $(0, 2\pi, 0)$ or $(2\pi, 0, 0)$. Both TRIMs Γ and Z are non-degenerate in spinless representations of SG 24, because the eigenvalues are real on the whole axis. Because of the translational parts of the mutually off-centered rotations, the product of all three rotations results always in a lattice translation,

$$2_{100}(0, 0, \frac{1}{2}) \cdot 2_{010}(\frac{1}{2}, 0, 0) \cdot 2_{100}(0, \frac{1}{2}, 0) = t(\frac{1}{2}, -\frac{1}{2}, \frac{1}{2}). \quad (3.3.4)$$

At Γ , the translation eigenvalue is +1 and the product of all three rotation eigenvalues ± 1 has to be positive, as it was the case previously, i.e., only none or two of the eigenvalues can be negative. At Z on the other hand,

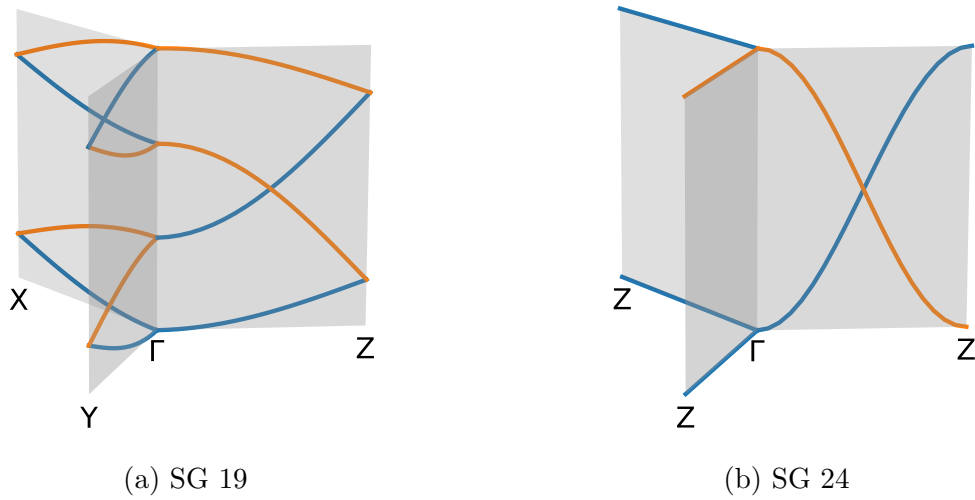


Figure 3.5: Band crossings enforced by compatibility relations comprising three rotation axes in spinless band structures. (a) Exemplary arrangement of bands with minimal crossings in spinless band structures of SG 19, leaving one movable Weyl point on one of the three rotation axes connecting to Γ . Blue (orange) colored bands correspond to bands labeled with positive (negative) eigenvalue according to the definition in Eq. (3.3.1). (b) Possible arrangement for a spinless band representation in SG 24 with rotation eigenvalue $+1$ in blue and -1 in orange of the corresponding axis. The product of eigenvalues is fixed to $+1$ at Γ and -1 at Z , enforcing a movable Weyl point on one of the axes.

eigenvalue of the translation is -1 , therefore the only valid combinations are those with one or three negative rotation eigenvalues. The two different requirements can only be fulfilled simultaneously by two bands exchanging on at least one rotation axis. An example representing a possible combination of two irreducible representations is shown in Fig. 3.5(b). There are three other possible representations, but the resulting restriction on the dispersion is always the same as in the example. In a real material the representations at Γ and Z are induced from the orbital present at a certain Wyckoff position [75]. The charge of this movable Weyl point is, in the absence of accidental crossings, compensated by the pinned Weyl point at W , which also appears in two symmetry-related copies. Finally, we consider the spinful cases. On the rotation axes through Γ , no such restrictions are found. As we have mentioned earlier, the results are still relevant for small SOC, since the chirality of these Weyl points protects them topologically. In order to remove these Weyl points, they have to annihilate with Weyl points of opposite chirality, which would require a large transformation of bands. The two time-reversal related copies however can move from the rotation axis to two symmetry-related k -points.

In addition, we find a movable Weyl point in spinful bands of SG 24 on one of the three axes W - R , W - S or W - T . The compatibility relations require the same connectivity as shown in Fig. 3.5(a) with W in the center. In that case, orange bands have the rotation eigenvalue $+i$ and blue ones i . All three rotation eigenvalues at W multiplied equal to $-i$. If SOC vanishes exactly, the Weyl point in each spin subspace is pinned to W , as has been shown above in Sec. 3.1.1. For non-zero SOC, they can split up and move onto a rotation axis, where they are still related by time-reversal symmetry.

Movable fourfold double Weyl

In a similar manner, the fourfold double Weyl point at R in SG 19 moves to one of the three axis S - R , U - R and T - R for non-vanishing SOC [74]. For the rotation eigenvalues at R , there is again the restriction, that in every irreducible representation the three rotation eigenvalues must multiply to an

odd number. Considering \mathcal{T} , all corepresentations are twofold degenerate on the three axes with pairs sharing the same eigenvalues. As discussed in Sec. 3.2.2, the TRIMs S, T and U host fourfold double Weyl points, where opposite eigenvalues are paired. Together, this necessitates a crossing of twofold degenerate bands on at least one rotation axis, forming a fourfold degenerate crossing. The little group of the axis consists of the twofold rotation and the combination of \mathcal{T} with each of the other two rotations. This restricts the crossing also to a fourfold double Weyl point with Chern number ± 2 .

Figure 3.6(a) shows an example of an arrangement of bands fulfilling the compatibility relations on the three rotation axes through R. Double lines show the twofold degenerate bands with identical eigenvalues and possible combinations at R. In Fig. 3.6(b) we show the DFT band structure of Ag_2Se in SG 19 with and without SOC in the vicinity of R. Without SOC, the point R is eightfold degenerate, namely a fourfold double Weyl in each spin subspace. Including SOC in the calculation lifts the spin degeneracy, leading to two symmetry-related, tilted fourfold double Weyl points on the axis connecting R and T.

3.4 Topological nodal planes

The combined symmetry of time-reversal symmetry followed by a twofold screw rotation leads to twofold degeneracies on a plane, which can contribute to the band topology [30, 76, 31]. We will discuss the mechanism enforcing the degeneracy and identify SGs where the nodal planes are necessarily topologically nontrivial.

The combination of time-reversal symmetry with any spatial symmetry is also antiunitary. Because \mathcal{T} commutes with all spatial symmetries, the order is not relevant and leads to the same element of the gray group. In the case of a twofold screw rotation, the square of the combined symmetry is a lattice translation along the rotation axis. This holds equally in double groups, because both the rotation and \mathcal{T} contribute \bar{E} , which in turn squares to the identity. In k -space, the combined symmetry acts like a reflection on

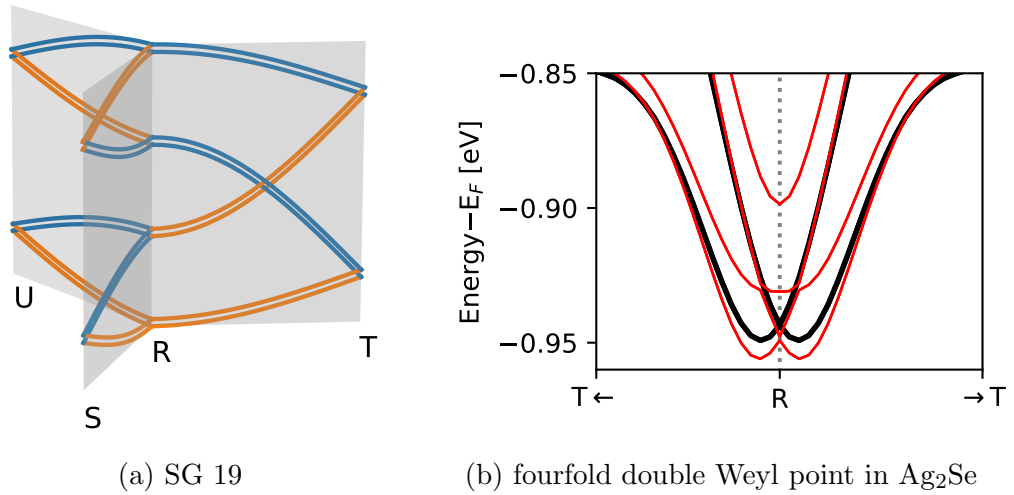


Figure 3.6: (a) Compatibility relations at R in SG 19 for spinful bands. Colors indicate the sign of the rotation eigenvalue according to Eq. (3.3.1). Note that all bands are twofold degenerate on the paths shown, with identical rotation eigenvalues being paired. Figure adapted from Ref. [74]. (b) Fourfold double Weyl point in Ag_2Se without SOC at R (black). Including SOC (red) moves the fourfold double Weyl point to the axis R-T.

a plane perpendicular to the rotation axis, because \mathcal{T} acts like inversion. For example, $2_{001}(0, 0, \frac{1}{2})\mathcal{T}$ squares to $t(0, 0, 1)$ and transforms a point \mathbf{k} according to $(k_x, k_y, k_z) \rightarrow (k_x, k_y, -k_z)$. The invariant planes are $k_z = 0$ and, if $\mathbf{K} = (0, 0, 2\pi)$ is a reciprocal lattice vector, $k_z = \pi$. The latter case is given in all primitive and base-centered orthorhombic lattices and in primitive tetragonal, hexagonal or cubic lattices. In the $k_z = \pi$ plane, the eigenvalue of the translation is $e^{ik_z} = -1$. Any antiunitary symmetry squaring to -1 enforces degeneracies on invariant momenta through Kramers theorem [53]. Consequently, the whole plane $k_z = \pi$ is twofold degenerate. Note that this holds equally for spinless and spinful representations. The degeneracy of the plane already contains the Kramers degeneracy at the TRIMs within it and there are no Kramers Weyl points. For this reason, there are no Weyl points at Z and A in the accordion states in Fig. 3.4(a). The twofold degeneracies in planes found in the low-energy models of fourfold double and quadruple Weyl points are also explained by this mechanism, c.f. Figures 3.1(b) and (c).

The nodal planes themselves can act as a source or sink of Berry curvature and thereby carry a topological charge. These topological nodal planes can in principle exist in all chiral SGs with nodal planes. Their Chern number can be directly evaluated on a closed surface slightly offset from the nodal plane, but close enough to stay clear of all degeneracies in the interior of the BZ. Because of the Nielsen-Ninomiya theorem [33], the chirality is the negative of the sum of Chern numbers from point crossings in the BZ interior closing the same gap. In some of these SGs, the topological charges of point crossings in the interior of the BZ cannot be balanced other than by the nodal plane, their topology is therefore symmetry-enforced. In the orthorhombic and tetragonal crystal systems, we identified four SGs with symmetry-enforced nodal planes, namely SG 19, the enantiomorphic pair SG 92 and SG 96, and SG 94.

There are three perpendicular twofold screw rotations in SGs 19, 92 and 96. Together they form a nodal plane trio, which encloses the BZ interior. Γ is the only TRIM not residing in a nodal plane and there is a Weyl point of chirality ± 1 [24, 77, 65]. Every other point in the BZ interior has a star of order two or larger, related by either a rotation or \mathcal{T} , both of which

relate Weyl points with identical chirality. Consequently, in the sum of all chiralities of the interior, accidental crossings only contribute even numbers and the sum is always odd,

$$\mathcal{C}_{\text{interior}} = 1 + 2n \quad n \in \mathbb{Z}. \quad (3.4.1)$$

Therefore, the topological charge of the nodal plane trio has to be odd as well and $|\mathcal{C}_{\text{NP}}| \geq 1$ [78].

In SGs 18, 90 and 94, there are the two screw rotations $2_{100}(\frac{1}{2}, \frac{1}{2}, \frac{1}{2})$ and $2_{010}(\frac{1}{2}, \frac{1}{2}, \frac{1}{2})$, enforcing a nodal plane duo build from the two degenerate planes $k_x = \pi$ and $k_y = \pi$. The TRIMs Γ and Z are now the only ones not in a nodal plane, both hosting Kramers Weyl points of chirality $\mathcal{C} = \pm 1$. In SG 18 and 90, these two are not related by symmetry and their topological charges might cancel, allowing the nodal plane duo to be trivial. In SG 94 however, the fourfold screw rotation $4_{001}(0, 0, \frac{1}{2})$ enforces an hourglass dispersion, in which the two Weyl points at both TRIMs have the same chirality for a minimal number of crossings, see Fig. 3.4(b). Introducing accidental crossings on the fourfold rotation axis cannot change the sum of chiralities and everywhere else they come in four symmetry-related copies with equal chirality. The charge of the nodal plane duo is therefore restricted to the values

$$\mathcal{C}_{\text{NP}} = 2 + 4n \quad n \in \mathbb{Z}, \quad (3.4.2)$$

and is at least doubly charged. The doubly charged nodal plane is especially interesting, because in an 001-termination the gap can in principle be preserved, which could reveal the two Fermi arcs connecting the projected Weyl points to the projected nodal plane. Unfortunately, SG 94 is very elusive and no suitable candidate material could be identified. As an alternative, a similar situation can be found in magnetic SGs by breaking one of the screw rotations in a nodal plane trio [31].

3.5 Case study for the chiral space groups 19 and 92/96

All of the above features are enforced in SG 92 and its enantiomorphic partner SG 96, and almost all of them also exist in their subgroup SG 19. Therefore, we construct the complete band connectivity with a minimal number of crossings from compatibility relations for these SGs and compare them to lattice models and materials. These models also demonstrate the balance of topological charges of the different types of degeneracies.

3.5.1 Tight-binding model for SG 19

For SG 19, we present a simple tight-binding model, containing all symmetry allowed next-nearest neighbor hopping terms. By separating inter- and intra-spin space contributions, the fate of each crossing upon inclusion of SOC can be demonstrated.

There is just one EBR in SG 19, i.e., any band structure is built from several instances of this set of bands. The EBR has four bands in the spinless case, corresponding to the multiplicity of its only Wyckoff position. Its site-symmetry group is 1, therefore it is not sensitive to the type of orbital placed there. Nearest-neighbor hopping terms are sufficient to create a maximally split band structure. We focus on the gap Hamiltonian, i.e., disregard any uniform dispersion, which is mostly determined by hopping of one lattice translation, i.e., next-nearest neighbor hopping. Note that a crystal in SG 19 based on atoms cannot be built with only four equivalent atoms per unit cell, as this would actually be the face-centered SG 69, which is symmorphic and inversion symmetric. In the four-band model, anisotropic hopping ensures the lower symmetry of SG 19. Without SOC, the gap Hamiltonian reads

$$H_0(\mathbf{k}) = \begin{pmatrix} 0 & (t_0+t_1e^{ik_x})(1+e^{ik_z}) & (t_2+t_3e^{ik_y})(1+e^{ik_x}) & (t_4+t_5e^{ik_z})(1+e^{ik_y}) \\ & 0 & (t_4e^{-ik_z}+t_5)(1+e^{ik_y}) & (t_2e^{ik_y}+t_3)(1+e^{-ik_x}) \\ & & 0 & (t_0e^{-ik_x}+t_1)(1+e^{ik_z}) \\ h.c. & & & 0 \end{pmatrix}, \quad (3.5.1)$$

containing the six free real parameters t_i . For non-zero SOC, we include a time-reversed copy and an off-diagonal block Λ covering all symmetry allowed intra-spin hopping terms,

$$H_{\text{gap}}(\mathbf{k}) = \begin{pmatrix} H_0(\mathbf{k}) & \Lambda(\mathbf{k}) \\ \Lambda^\dagger(\mathbf{k}) & H_0^*(-\mathbf{k}) \end{pmatrix}. \quad (3.5.2)$$

Introducing the short notations $c_i = 1 + e^{+ik_i}$ and $s_i = 1 - e^{+ik_i}$, this term is given by

$$\Lambda(\mathbf{k}) = \begin{pmatrix} 0 & (\lambda_0 + \lambda_1 e^{+ik_x})c_z & (\lambda_2 + \lambda_3 e^{+ik_y})c_x & (\lambda_4 + \lambda_5 e^{+ik_z})s_y \\ -(\lambda_0 + \lambda_1 e^{-ik_x})c_z^* & 0 & (\lambda_4 e^{-ik_z} + \lambda_5)s_y & -(\lambda_2 e^{+ik_y} + \lambda_3)c_x^* \\ -(\lambda_2 + \lambda_3 e^{-ik_y})c_x^* & -(\lambda_4 e^{+ik_z} + \lambda_5)s_y^* & 0 & -(\lambda_0 e^{-ik_x} + \lambda_1)c_z \\ -(\lambda_4 + \lambda_5 e^{-ik_z})s_y^* & (\lambda_2 e^{-ik_y} + \lambda_3)c_x & (\lambda_0 e^{+ik_x} + \lambda_1)c_z^* & 0 \end{pmatrix} \quad (3.5.3)$$

$$+ i \begin{pmatrix} 0 & (\lambda_6 + \lambda_7 e^{+ik_x})c_z & (\lambda_8 + \lambda_9 e^{+ik_y})s_x & -(\lambda_{10} + \lambda_{11} e^{+ik_z})c_y \\ -(\lambda_6 + \lambda_7 e^{-ik_x})c_z^* & 0 & (\lambda_{10} e^{-ik_z} + \lambda_{11})c_y & -(\lambda_8 e^{+ik_y} + \lambda_9)s_x^* \\ -(\lambda_8 + \lambda_9 e^{-ik_y})s_x^* & -(\lambda_{10} e^{+ik_z} + \lambda_{11})c_y^* & 0 & (\lambda_6 e^{-ik_x} + \lambda_7)c_z \\ (\lambda_{10} + \lambda_{11} e^{-ik_z})c_y^* & (\lambda_8 e^{-ik_y} + \lambda_9)s_x & -(\lambda_6 e^{+ik_x} + \lambda_7)c_z^* & 0 \end{pmatrix}.$$

The spinful model has 12 additional real parameters λ_i , allowed by symmetry. The spinless case with a twofold spin degeneracy is recreated by setting all of them to zero. Only few of these need to be non-zero in order to split the spin degeneracy with no fine-tuned degeneracies left. In Fig. 3.7 we show the schematic band structure together with the dispersion of the tight-binding model and a material example along the high-symmetry path of the primitive orthorhombic BZ. The band structure without SOC, shown in blue, has two movable Weyl points on the axis Γ -X with identical chirality and a fourfold double Weyl at R compensating their charges. The orange bands show the band structure for nonzero values for the λ_i . At half filling, there are four movable Weyl points, which moved from the axis to the interior and are not visible along the high-symmetry path. They have to exist to balance the Chern number of the fourfold double Weyl points which split and moved onto the axis U-R [65]. There are hourglass states visible on all three rotation axis connecting to Γ . Charge balance for two or six filled bands is achieved with

the fourfold double Weyl points at S, U and T. Nodal planes remain twofold degenerate in both cases, indicated by the thick lines in the sketch. In the spinful case they are necessarily topological, balancing the charge at Γ for an odd number of filled bands.

As an example material, we identified the narrow gap semiconductor Ag_2Se in the material search, whose room temperature polymorph crystallizes in SG 19 [79]. In Fig. 3.7(c) we present the DFT band structure including SOC. Although the splitting of spin degenerate bands is small relative to the band width, hourglass states are well resolved along Γ -Z. The fourfold degeneracy at R is shown in detail in Fig. 3.6(b)

3.5.2 Example material Ba_3Sn_2 in SG 96

Space group 96 is a supergroup of SG 19 with a fourfold screw rotation $4_{001}(0, 0, \frac{3}{4})$ as additional generator. This puts further restrictions on the band connectivity and symmetry-enforced crossings. In the spinless case, the schematic band structure remains mostly unchanged. There are again four bands in every EBR. The previously movable crossing at half filling is now pinned to Γ , where it forms a spinless double Weyl point, compare the blue bands in Fig. 3.8(a) and Fig. 3.7(a). Its charge balances the fourfold double Weyl point at A.

As discussed in Sec. 3.3.1 and Sec. 3.3.2, SOC splits bands such, that hourglass and accordion states are formed on the twofold and fourfold rotation axis, respectively. There is no movable fourfold double Weyl point, instead the spin-degenerate fourfold double Weyl point splits up into two twofold degenerate bands and a fourfold quadruple Weyl point at R, as discussed in Sec. 3.2.3.

In Fig. 3.8(b) we present the band structure of the binary compound Ba_3Sn_2 , which crystallizes in SG 96 [80] and has been identified in our material search. This material is insulating with a narrow band gap and the first eight bands below the Fermi energy are all from one EBR and can be compared directly to the connectivity diagram. In the uppermost occupied bands, the movable crossings of the hourglass dispersion are too close to X to

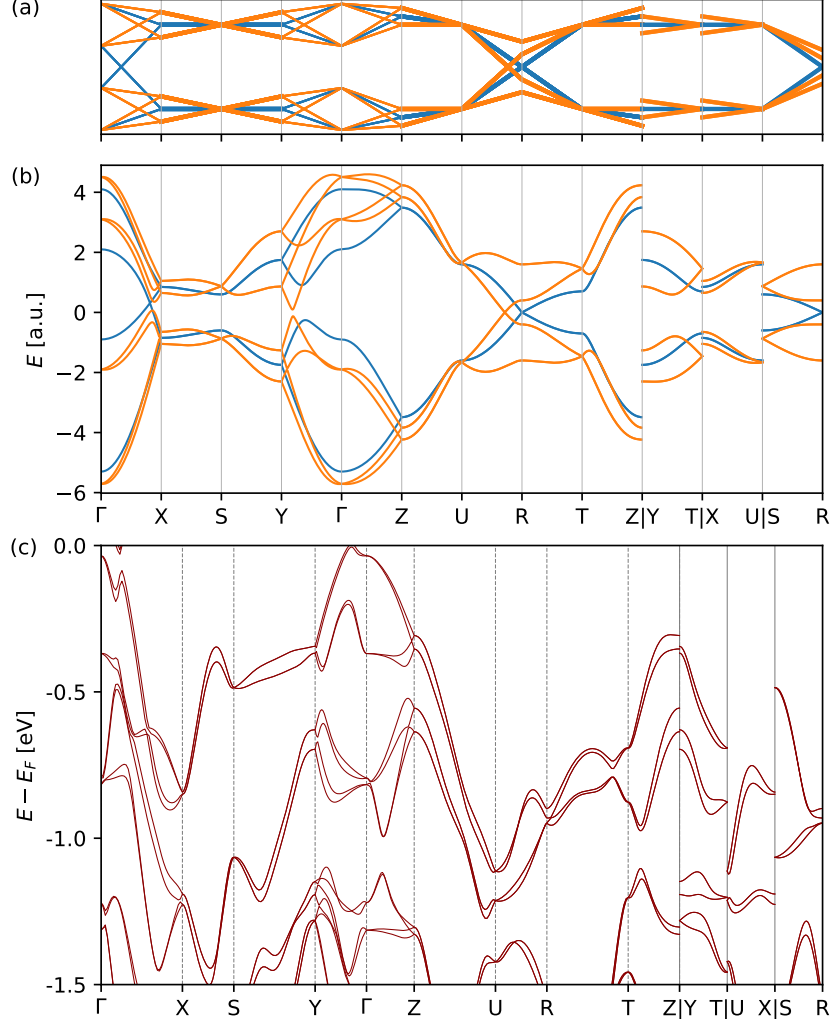


Figure 3.7: Elementary band representation in SG 19. (a) Band connectivity diagram based on compatibility relations of representations. Spinless bands are shown in blue, spinful bands in orange. Thick lines indicate twofold degenerate bands in nodal planes. (b) Minimal tight-binding model for SG 19 defined in Eq. (3.5.2) with hopping parameters $t_0 = -t_5 = 0.25$, $t_1 = -t_4 = 0.55$, $t_2 = -0.6$, $t_3 = -0.95$, $\lambda_i = 0$ for the spinless case (blue), for the case with SOC (orange) $\lambda_0 = \lambda_1 = \lambda_7 = 0$, $\lambda_2 = -\lambda_5 = 0$, $\lambda_3 = 0.7$, $\lambda_4 = -\lambda_8 = 0.2$, $\lambda_5 = -0.3$, $\lambda_9 = \lambda_{10} = -\lambda_{11} = 0.1$. Parameters were chosen for maximal visibility of the features mentioned in the text. (c) DFT band structure for Ag_2Se including SOC.

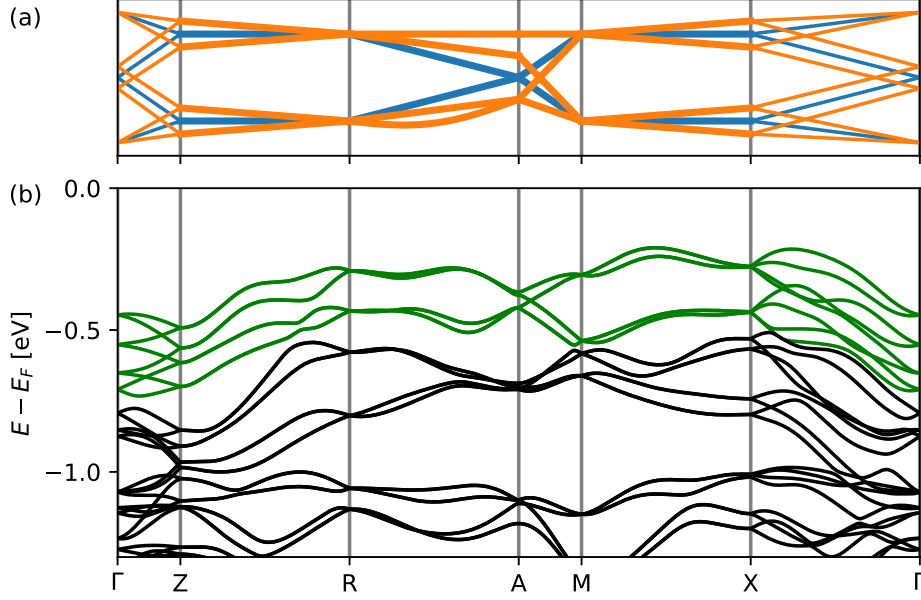


Figure 3.8: Elementary band representation in SG 96: (a) Schematic band structure based on the connectivity of irreducible representations without (blue) and with SOC (orange). Thick lines indicate twofold degenerate bands within nodal planes. (b) Band structure of Ba_3Sn_2 calculated from first principles including SOC. All Bands show the same connectivity as in the above sketch. The accordion states along Γ -Z can be seen most clearly in the uppermost eight bands (green), whereas the hourglass states are only resolved in some bands lower in energy.

be resolved, but they are visible in the bands below. An additional feature is the fourfold degenerate band crossing along A-M. This feature is protected by symmetry eigenvalues, but not mandated by band connectivity. It can in principle be removed by exchanging the bands at A such that the fourfold degenerate representation falls between the two twofold representations. In either case, the fourfold degeneracy at half filling has to carry a Chern number of $\mathcal{C} = \mp 2$ to cancel the topological charges of the double Weyl point with $\mathcal{C} = \pm 2$ in the accordion state at half filling. Again, the path segments on the BZ surface are twofold degenerate as they are part of topological nodal planes, balancing the chirality of the Weyl point at Γ .

3.6 Dirac points

The wave function of a free, massive fermion is described by the Dirac equation [81],

$$(i\gamma^\mu \partial_\mu - m)\Psi = 0, \quad (3.6.1)$$

written in terms of the four-dimensional Dirac matrices. These are defined through the anticommutation relation

$$\{\gamma^\mu, \gamma^\nu\} = 2\eta^{\mu\nu} \mathbf{1}_{4 \times 4}. \quad (3.6.2)$$

Here $\eta^{\mu\nu}$ is the Minkowski metric. The corresponding Hamiltonian in momentum space reads

$$H = \gamma^0(\gamma^i p_i + m) \quad (3.6.3)$$

In condensed matter systems, a Dirac fermion refers to a set of four bands, which can be described by a linearized Hamiltonian in a subset of the BZ that can be mapped to Dirac Hamiltonian by a similarity transformation. Expanded in relative coordinates \mathbf{q} the Hamiltonian is of the form

$$H_{\text{Dirac}}(\mathbf{q}) = \sum_{i=1}^3 v_i q_i \gamma_0 \gamma_i + m \gamma_0, \quad (3.6.4)$$

If we choose the representation for the Dirac matrices $\gamma_0 \gamma_i = \tau_z \otimes \sigma_i$ and $\gamma_0 = \tau_z \sigma_0$, written in terms of two sets of Pauli matrices σ_i and τ_i , $i \in \{x, y, z, 0\}$, the connection to the Weyl-Hamiltonian introduced in Eq. (3.1.2) becomes immediately apparent. Without the mass term, those are just two Weyl points with opposite signs in all three velocity factors v_i and therefore opposite Chern numbers. Since the total Chern number vanishes, it is possible to introduce a gap via a non-vanishing mass term $m\gamma_0$.

A Dirac *point* corresponds to the special case $m = 0$ and has a gapless spectrum with a fourfold degeneracy and linear dispersion in all three spatial directions. From the definition above it follows, that a Dirac point splits into twofold degenerate bands. In the literature, the term is often used more loosely and any fourfold degenerate point with linear dispersion is called a

Dirac point. In this work, we require the linear dispersion and a vanishing Chern number. The latter distinguishes Dirac points from the fourfold double Weyl points in Sec. 3.2.2. In addition, we will explicitly highlight the cases, where bands are not twofold degenerate as an exception.

3.6.1 Dirac points at high-symmetry points

Symmetry-enforced Dirac points at high-symmetry points appear in spinful band structures of many centrosymmetric SGs at TRIMs. Inversion combined with time-reversal symmetry, \mathcal{PT} , already leads to twofold degenerate bands in the whole BZ in all centrosymmetric SGs and all Chern numbers must be zero, because the Berry curvature vanishes identically at each point in the BZ. For a symmetry-enforced Dirac point, a second kind of pairing mechanism needs to be present to ensure a vanishing mass term, thereby guaranteeing the fourfold degeneracy.

Here, we present this mechanism exemplarily for the orthorhombic SG 49. The four TRIMs in the $k_z = 0$ plane are all only twofold degenerate and therefore not different from the bands in their vicinity. Each of the TRIMs in the $k_z = \pi$ plane, however, host symmetry-enforced Dirac points. Any TRIM in centrosymmetric SGs has always inversion in its little group, since the action in k -space is the same for \mathcal{T} and \mathcal{P} . The fourfold degeneracy can be understood from the product of one of the glide mirror symmetries and the rotation with its axis perpendicular to the mirror plane, which multiplies to the inversion symmetry and potentially a translation,

$$\begin{aligned} 2_{100}(0, 0, \frac{1}{2}) \cdot M_{100}(0, 0, \frac{1}{2}) &= \mathcal{P}(0, 0, 1), \\ M_{100}(0, 0, \frac{1}{2}) \cdot 2_{100}(0, 0, \frac{1}{2}) &= \mathcal{P}(0, 0, 0). \end{aligned} \quad (3.6.5)$$

At TRIMs with $k_z = \pi$, the translation eigenvalue is -1 and consequently the representations anticommute, whereas at TRIMs with $k_z = 0$ the translation eigenvalue is $+1$ and they commute. The representations for the three perpendicular twofold rotations always anticommute and are therefore proportional to the Pauli matrices, as previously shown in Sec. 3.1.1. In the

commuting case, the representation of the reflection must be proportional to the same Pauli matrix as the one from the rotation, therefore the product is $U_P = \pm\sigma_0$, and two identical inversion eigenvalues are paired. Kramers theorem does not lead to an additional pairing and the points remain twofold degenerate. In the anti-commuting case, the two representations are made from two different Pauli matrices and their product is proportional to the third one, implying the pair has inversion eigenvalues with opposite sign. Kramers partners, on the other hand, share the inversion eigenvalue, resulting in the fourfold degeneracy of the Dirac point. A similar situation can be found in many other orthorhombic and tetragonal SGs with inversion and nonsymmorphic mirror symmetries, all of which are listed in Tables IV and VI.

Another notable example are the eightfold degenerate double Dirac points which can only be found in the two tetragonal SGs 130 and 138 [82]. At the point $A = (\pi, \pi, \pi)$, the representations of the three glide mirror symmetries anticommute, because the products differ by a translation with eigenvalue -1 , creating a twofold degeneracy of eigenvalues with opposite sign for each eigenvalue. Additionally, two of the glide mirror symmetries have real eigenvalues and Kramers theorem implies that there must be four orthogonal states. It further follows, that the product of the three perpendicular reflections is proportional to the identity, $U_P = \pm i\tau_x\tau_y\tau_z = \pm\tau_0$. Including the Kramers degeneracy, the fourfold degeneracy consists entirely of states with the same inversion eigenvalues. A similar argument holds for two of the rotation axes with little group $mm2 + \mathcal{PT}$, preventing a gap from opening along the invariant axis. Finally, the fourfold rotation 4_{001} anticommutes with inversion and therefore requires an eightfold degeneracy at A. The dispersion looks identical to the one of a fourfold double Weyl point, shown in Fig. 3.1(b) with a linearly growing gap between the fourth and the fifth band. Here however, all bands are twofold degenerate and the Chern number is zero, hence the name double Dirac point.

Fourfold degenerate points without inversion

Without inversion and in spinless band structures, there are no Dirac points in the strict sense. We found however many cases of fourfold degenerate points with vanishing Chern number and linear dispersion in spinful band structures of SGs with two perpendicular glide mirror symmetries. A direct evaluation of the product of two perpendicular mirror symmetries with translational parts (a, b, c) and (d, e, f) reveals

$$M_{100}(a, b, c) \cdot M_{010}(d, e, f) = \bar{E}(-2d, 2b, 0) \cdot M_{010}(d, e, f) \cdot M_{100}(a, b, c). \quad (3.6.6)$$

Depending on the eigenvalue of $\bar{E}(-2d, 2b, 0)$, the representation at a TRIM commutes or anticommutes. In the second case, the representations must be at least two-dimensional and eigenvalues with opposite signs are paired for each symmetry,

$$U_i U_j |\pm m_i\rangle = -U_j U_i |\pm m_i\rangle = \mp m_i U_j |\pm m_j\rangle. \quad (3.6.7)$$

Glide reflections are nonsymmorphic symmetries and square to a \bar{E} combined with a lattice translation, e.g.,

$$M_{100}(a, b, c)^2 = \bar{E}(0, 2b, 2c), \quad (3.6.8)$$

where b and c can have half integer values. The eigenvalues of glide reflections are therefore square roots of -1 or $+1$ at TRIMs, depending on the translation eigenvalue.

A fourfold degenerate point follows in the second case, when both mirror symmetries have real eigenvalues ± 1 and Kramers partners share the same eigenvalues. If only one of them has real eigenvalues, the gap will remain closed along a line, as we will see in Sec. 3.7.2. Although the Berry curvature does not vanish identically, the resulting fourfold degeneracy cannot carry a Chern number. Contributions from both sides of a mirror plane to the surface integral cancel, since the Berry curvature transforms as a pseudo vector under reflections. Both statements can again be demonstrated from

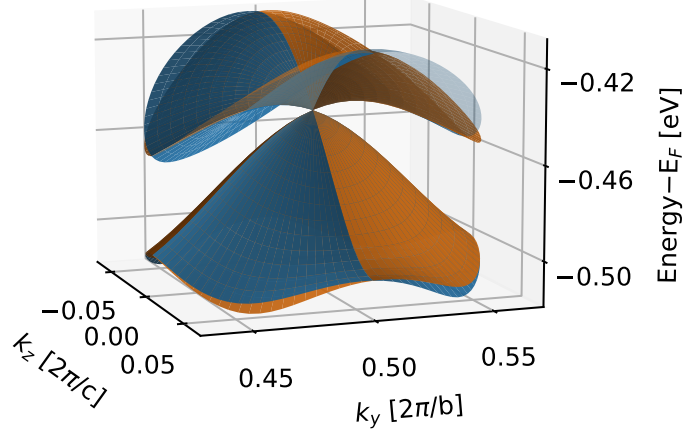


Figure 3.9: Dispersion around the point $S = (\pi, \pi, 0)$ in the $k_x = \pi$ plane in AuTlSb, crystallizing in SG 33. Colors indicate the relative sign of M_{100} eigenvalues. All twofold degeneracies are part of nodal lines with opposite mirror eigenvalues.

a low-energy Hamiltonian. The representations for the symmetry generators at the TRIM can be given by

$$U_{M_{100}} = \tau_0 \sigma_x, \quad (3.6.9)$$

$$U_{M_{010}} = \tau_0 \sigma_y, \quad (3.6.10)$$

$$U_{\mathcal{T}\mathcal{K}} = i\tau_y \sigma_x \mathcal{K}, \quad (3.6.11)$$

which restricts the linearized Hamiltonian to the form

$$\begin{aligned} H(\mathbf{q}) = & v_z q_z \tau_z \sigma_0 + v_x q_x \tau_z \sigma_y + v_y q_y \tau_z \sigma_x \\ & + \lambda_x q_x \tau_x \sigma_y + \lambda_y q_y \tau_x \sigma_x + \lambda_z q_z \tau_x \sigma_0, \end{aligned} \quad (3.6.12)$$

with the real parameters v_i and λ_i . The gap between the second and third band closes only at the TRIM, i.e., for $\mathbf{q} = 0$. The bands are maximally split from linear terms only and the vanishing Chern number can be verified numerically. A real material example is shown in Fig. 3.9.

Another noteworthy case is the only fourfold degenerate point with van-

ishing Chern number in spinless band structures in orthorhombic SGs. The body centered SG 73 is a supergroup of SG 24 and inherits its Weyl point at $W = (\pi, \pi, \pi)$. However, SG 73 contains also inversion symmetry. In spinless band structures, \mathcal{PT} does not lead to Kramers degenerate bands at generic positions, but the twofold degeneracy is doubled at W by \mathcal{PT} . The dispersion looks like the one of a fourfold double Weyl point, shown in Fig. 3.1(b), since there are only rotations in the little group. The difference is, that both Weyl points have opposite chirality, such that the total Chern number vanishes. The low-energy Hamiltonian up to linear order is equivalent to the one described in Eq. (3.6.12) previously.

3.6.2 Movable Dirac points

Dirac points can also be symmetry-enforced on a rotation axis in centrosymmetric SGs, similar to movable Weyl points. In most SGs with inversion, the hourglass dispersion from screw rotations is suppressed by the overall twofold degeneracy with rotation eigenvalue pairs $(+, -)$, according to the definition in Eq. (3.3.1). If the screw rotation is however off-centered from the inversion center, the co-representation of \mathcal{PT} anticommutes on some rotation axes and pairs identical eigenvalues as $(+, +)$, and $(-, -)$ [83]. For an hourglass dispersion as shown in Fig. 3.3, fourfold degeneracies at two TRIMs are needed additionally. Since the eigenvalue of the screw rotation is $\pm i$ at one TRIM, \mathcal{T} creates the fourfold degeneracy $(+, +, -, -)$ there. At the other TRIM, however, the screw rotation eigenvalue alone is not sufficient to enforce a fourfold degeneracy. In orthorhombic and tetragonal centrosymmetric SGs with primitive lattices, two perpendicular mirror symmetries are also part of the little group of any rotation axis, one of which must be a glide reflection. Their representations need to commute with the rotation, otherwise there would be a fourfold degeneracy on the whole line, see Sec. 3.7.5. If the partners within a pair $(+, +)$ or $(-, -)$ have distinct real valued glide mirror eigenvalues, they cannot be Kramers partners. Consequently, a co-representation at the second TRIM needs to contain four states with rotation eigenvalues $(+, +, +, +)$ or $(-, -, -, -)$. The resulting hourglass dispersion

is identical to the one for a movable Weyl point, but all the bands are twofold degenerate. The crossing on the axis itself is not invariant under inversion, but splits into twofold degenerate bands in all directions and forms therefore a Dirac point. We find these conditions to be met in the four orthorhombic SGs 52, 54, 56, and 60, and in the three tetragonal SGs 130, 133, and 138.

We also identified one movable Dirac point from a compatibility relation spanning the three rotation axis connecting to W in SG 73. In $SU(2)$ -symmetric band structures, there is a pinned Dirac point at W . Counting the spin degrees of freedom, this corresponds to an eightfold degeneracy. Non-vanishing SOC lifts this degeneracy, which splits into two symmetry-related Dirac points on one of the rotation axes. Each of the TRIMs R , S , and T has one rotation in its site symmetry group and the corresponding rotation eigenvalues are paired as $(+, +, -, -)$. On the axis connecting to W , the pairing is $(+, +)$ and $(-, -)$. At W , all three rotation eigenvalues are simultaneously present, but their overall sign is restricted to $+$. This can only be arranged with a minimum of one band crossing on one of the axes W - R , W - S , and W - T , equivalent to the requirement shown in Fig. 3.5(a). The resulting band crossing forms also movable Dirac point.

3.7 Line degeneracies

Nodal lines are —after nodal points and planes— a third type of symmetry-enforced degeneracies. Linearly dispersing twofold degenerate lines are generally enforced by mirror symmetries, which can be motivated by a parameter counting argument. In a subspace of two bands with opposite mirror eigenvalues, the matrix representation of a mirror symmetry is proportional to one of the Pauli matrices. The other two Pauli matrices in the gap Hamiltonian change sign under the application of the symmetry and must therefore vanish in the mirror plane. For the remaining component, there are no further restrictions on the two in-plane coordinates and it can therefore vanish along an one-dimensional sub-manifold. Therefore, we find symmetry-enforced nodal lines in non-chiral SGs, i.e., those with at least one mirror symmetry.

The topological invariant of nodal lines is the Berry phase, evaluated on an integral along a loop enclosing the nodal line. The mirror symmetry restricts the value of any loop integral to 0 or π . The presence of a line defect therefore changes the homotopy of Berry phase loops. Because this results in a \mathbb{Z}_2 invariant, nodal lines are not stable against large perturbations, since they can annihilate pairwise or be removed by shrinking them to a point. But as long as all symmetries of a SG remain unbroken, symmetry-enforced nodal lines are necessarily present in the following cases.

In the orthorhombic and tetragonal SGs, all symmetry-enforced nodal lines can be grouped in one of three categories. First, we give examples of nodal lines pinned to a high-symmetry axis, which are enforced by the little co-group structure. In Sec 3.7.2, we introduce the more interesting case of almost movable and movable lines, which are at most pinned to high-symmetry points, but can be moved freely within a mirror plane.

3.7.1 Pinned nodal lines

Twofold degeneracies along high-symmetry axis are common in many SGs and can be understood from the irreducible co-representations of their little groups. These can be found in tables, for example on the Bilbao Crystallographic Server [4, 3, 75]. For later reference, we introduce two common examples.

The first case is independent of time-reversal symmetry. If the matrix representations of symmetries in the little group $mm2$ anticommute, they must be at least two-dimensional and eigenvalues with opposite signs are paired for each symmetry, c.f., Eq. (3.6.7). Previously, we have shown that the commutation relation of two perpendicular mirror symmetries depends on the \bar{E} eigenvalue and fractional translations in off-centered and nonsymmorphic symmetries, see Eq. (3.6.6). On any axis through Γ , each of the spinful representations always square to $U_{\bar{E}} = -1$, because any translational part has always eigenvalue $+1$. At the same time, a product of any two of the three symmetries results in the third, which also squares to $U_{\bar{E}} = -1$. The smallest matrix representation that fulfills these requirements is generated by

the three Pauli matrices with a complex factor, $U_i = i\sigma_i$. Therefore, an anti-commutation relation is found in all spinful representations of the little group $mm2$ at least on the rotation axes through Γ , c.f. Table II. Pinned nodal lines are not listed in Table V, but it holds equally for axis through Γ with little group $4mm$ in the tetragonal SGs. In spinless representations, such a nodal line requires at least one glide mirror symmetry. An anticommutation relation is then given on those axis, where the translation in Eq. (3.6.6) has eigenvalue -1 , see Table I. Pinned nodal lines of this type do not rely on \mathcal{T} and are also degenerate when it is broken.

A second important example results from combining \mathcal{T} with a glide mirror symmetry. This antiunitary symmetry acts like a rotation in k -space, with its axis perpendicular to the mirror plane, and squares to a lattice translation. In the spinful case, \mathcal{T} and the mirror symmetry each contribute a factor i and no distinction between the two cases is necessary. With a translation eigenvalue of -1 , the conditions for Kramers theorem are fulfilled and the whole invariant axis is twofold degenerate. At the TRIMs on the axis, the two symmetries exist independently and in the spinless case identical mirror eigenvalues $+1$ or -1 are paired, whereas in spinful representations the pair consists of the complex partners $\pm i$.

Fourfold degenerate nodal lines from rotoinversion

Combining \mathcal{T} with a rotoinversion also acts like a rotation in k -space. A fourfold degenerate line follows from the combination of two antiunitary symmetries $\bar{4}_{001}\mathcal{T}$ and a perpendicular screw rotation $2_{010}(\frac{1}{2}, \frac{1}{2}, c)\mathcal{T}$. This combination exists in time-reversal symmetry band structures of SGs 113 and 114 in the tetragonal SGs with SOC, whose generators contain the spatial symmetries mentioned above. The factor $c = 0, \frac{1}{2}$ distinguishes between SG 113 and SG 114 and is not relevant in the following discussion.

In Sec. 3.4, we showed how $2_{010}(\frac{1}{2}, \frac{1}{2}, c)\mathcal{T}$ leads to nodal planes in the $k_y = \pi$ plane. The same holds true for $2_{100}(\frac{1}{2}, \frac{1}{2}, c)\mathcal{T}$ in the $k_x = \pi$ plane, meaning there is a nodal plane duo in these SGs. Simultaneously, $\bar{4}_{001}\mathcal{T}$ squares to $\bar{E}2_{001}$ and leaves the line (π, π, w) at the intersection of the nodal

planes invariant. It further fulfills the conditions of Kramers theorem on these lines, since the eigenvalues of 2_{001} are $\pm i$.

Both antiunitary symmetries enforce Kramers pairs, but with different eigenvalues, creating a pinned fourfold degenerate line. To illustrate this, we label the states with the sign of their 2_{001} -eigenvalues $\pm i$. Since the representations of 2_{001} and $\bar{4}_{001}\mathcal{T}$ always commute, the eigenvalues are related only via complex conjugation, i.e., the pairing is $(+, -)$. $2_{010}(\frac{1}{2}, \frac{1}{2}, c)\mathcal{T}$, on the other hand, anticommutes with 2_{001} , adding another sign change to the complex conjugated eigenvalue. Hence it pairs $(+, +)$ and $(-, -)$. In combination, we find the fourfold degeneracy of the nodal line with the pairing $(+, +, -, -)$. Apart from the planes $k_y = \pi$ and $k_x = \pi$, the bands are nondegenerate. For constant k_z , this is the same structure seen in the fourfold double Weyl point shown in Fig. 3.1(b). Since the Berry phase is a \mathbb{Z}_2 invariant, two nodal lines on top of each other are not topologically protected. A linearized Hamiltonian of the fourfold degenerate line, however, can always be brought in block diagonal form, which allows to define the topological invariant in each subspace. Note that only the directions perpendicular to the nodal line are expanded in relative coordinates q_x and q_y , as k_z spans the full range from $-\pi$ to π along the nodal line.

The irreducible matrix co-representation can be given as

$$U_{2_{001}} = \tau_0(-i\sigma_y) \quad (3.7.1)$$

$$U_{M_{110}} = \tau_0(i e^{ik_z c} \sigma_x) \quad (3.7.2)$$

$$U_{\bar{4}_{001}^+} \mathcal{T} \mathcal{K} = -i\tau_y \frac{\sigma_0 - i\sigma_y}{\sqrt{2}} \mathcal{K}. \quad (3.7.3)$$

The linearized Hamiltonian close to the nodal line at $\mathbf{q} = (q_x, q_y, k_z) = \mathbf{k} - (\pi, \pi, 0)$ is restricted by these symmetries to the form

$$H(\mathbf{q}) = \begin{pmatrix} \alpha q_+ \sigma_z + \beta q_- \sigma_x & \lambda(q_+ \sigma_z - q_- \sigma_x) \\ \lambda(q_+ \sigma_z - q_- \sigma_x) & \beta q_+ \sigma_z + \alpha q_- \sigma_x \end{pmatrix} + \varepsilon_0 \mathbf{1}, \quad (3.7.4)$$

with the perpendicular momentum components $q_{\pm} = q_x \pm q_y$ and the param-

eters α, β, λ and ε_0 all depending arbitrarily on k_z .

This Hamiltonian can be block diagonalized via the unitary, \mathbf{k} -independent matrix $T = \cos \phi \tau_0 \sigma_0 + \sin \phi i \tau_y \sigma_0$, where $\tan(2\phi) = \frac{2\lambda}{\alpha - \beta}$, and reads in the new basis

$$H(\mathbf{q}) = \begin{pmatrix} \tilde{\alpha} q_+ \sigma_z - \tilde{\beta} q_- \sigma_x & 0 \\ 0 & \tilde{\beta} q_+ \sigma_z - \tilde{\alpha} q_- \sigma_x \end{pmatrix} + \varepsilon_0 \mathbf{1}. \quad (3.7.5)$$

The two blocks describe decoupled linearly dispersing nodal lines with the modified velocities

$$\begin{aligned} \tilde{\alpha} &= \frac{\alpha + \beta}{2} + \operatorname{sgn}(\alpha - \beta) \sqrt{\left(\frac{\alpha - \beta}{2}\right)^2 + \lambda^2}, \\ \tilde{\beta} &= \frac{\alpha + \beta}{2} - \operatorname{sgn}(\alpha - \beta) \sqrt{\left(\frac{\alpha - \beta}{2}\right)^2 + \lambda^2}. \end{aligned} \quad (3.7.6)$$

In the nodal planes we find $|q_+| = |q_-|$ and the spectrum becomes degenerate, as demanded by symmetry. Furthermore, a $\frac{\pi}{2}$ -rotation around the k_z -axis relates the eigenvalues of the upper block to the ones in the lower one and vice versa. The nodal line in each subspace is protected by a Berry phase of π . Including symmetry allowed terms of higher order in \mathbf{q} only adds a quadratic dispersion ε_0 , identical to both bands, but cannot remove the degeneracy. In Fig. 3.10 we present the dispersion of such a fourfold degenerate line in NaSn₅, which crystallizes in SG 113 [84].

3.7.2 Movable nodal lines

As we have seen earlier, glide mirror symmetries play an important role in enforcing pinned nodal lines. Like nonsymmorphic rotations, they can also enforce movable nodal lines, which can move freely in the mirror plane.

The half-integer lattice translation $\frac{1}{2}\mathbf{t}$ of a glide mirror symmetry M with surface normal \mathbf{n} can be decomposed in a parallel component $\mathbf{t}_{\parallel} = (\mathbf{t} \cdot \mathbf{n})\mathbf{n}$ and a perpendicular in-plane component $\mathbf{t}_{\perp} = \mathbf{t} - \mathbf{t}_{\parallel}$. If the former is non-zero, the mirror symmetry is off-centered, which has no influence on its eigenvalues. The latter means it is a nonsymmorphic symmetry and its eigenvalues are

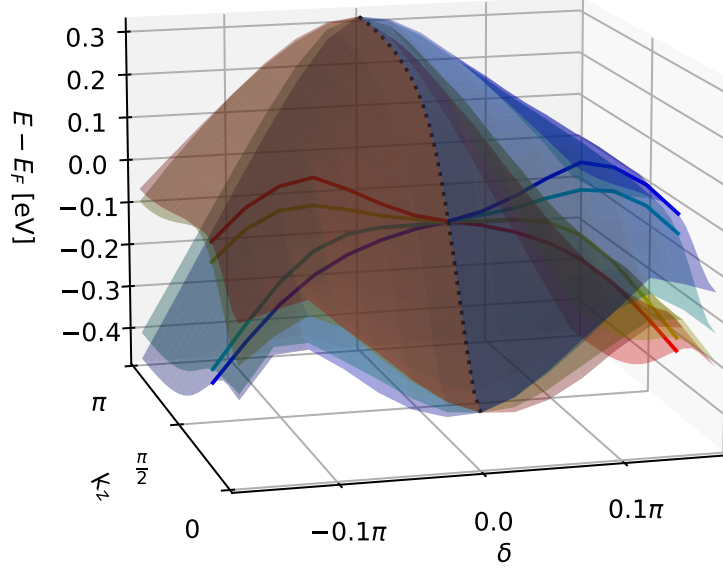


Figure 3.10: Dispersion around the fourfold nodal line in the plane defined by $\mathbf{k} = (\pi + \delta, \pi + \delta, k_z)$ in NaSn₅. The dashed line highlights the fourfold degeneracy on the high-symmetry axis. The colored solid lines show the dispersion perpendicular to the nodal line at constant k_z , where the nodal line crosses the Fermi level. The linear splitting of bands is partly obscured by the large collective bending of bands from the quadratic terms.

k -dependent,

$$U_M |\pm\rangle = \pm i^\zeta \exp(i\mathbf{k} \cdot \frac{1}{2}\mathbf{t}_\perp) |\pm\rangle, \quad (3.7.7)$$

because $(M \cdot \frac{1}{2}\mathbf{t})^2 = \bar{E} \cdot \mathbf{t}_\perp$ requires the mirror eigenvalues contain the square roots of the translation eigenvalue. The factor $\zeta = 0, 1$ reproduces the spinless or spinful \bar{E} eigenvalue, respectively.

In primitive lattices, the eigenvalue acquires a negative sign when traversing the mirror plane. Therefore, the bands need to exchange along paths parallel to each non-zero component of \mathbf{t}_\perp . Additionally, symmetry eigenvalues can be paired at high-symmetry points or pinned nodal lines in a different

way, such that an hourglass dispersion is enforced in between them. For example, the glide reflection $M_{010}(\frac{1}{2}, 0, 0)$ of SG 28 has eigenvalues $\pm i$ in spinful representations at the twofold degenerate line connecting Γ and Z. In the following, we denote these axis compactly by the TRIMs on them, connected with a dash, e.g., Γ -Z. There, states with opposite eigenvalues are paired by the anticommutation relation mentioned earlier, likewise on the axis Y-T. This pairing is compatible with the one from \mathcal{T} at each TRIM on the axis. At the TRIMs X, U, S, and R on the other hand, the eigenvalues are ± 1 , which means \mathcal{T} pairs identical eigenvalues. This requires a total of four bands and an hourglass dispersion like the one sketched in in Fig. 3.3 is enforced on paths in the mirror plane $k_y = 0$, which connect the axis Γ -Z with X or U. Since this holds for arbitrary paths, the movable degeneracy forms a nodal line in the mirror plane, see the illustration in Fig. 3.11(a). This holds equally for paths in the other mirror plane $k_y = \pi$, which connect Y-T with R or S. Such movable nodal lines are indicated in Tables I to IV and Table V in terms of a tuple containing the degenerate points or lines, separated by a semicolon. Entries left of the semicolon have eigenvalues with different signs paired, whereas the entries to the right are pairs with the same eigenvalue. The mirror plane can be inferred from the high-symmetry points and lines in the bracket. In the example above, the two entries are (Γ -Z;X,U) and (Y-T;R,S).

For certain combinations of glide reflections, there can be points where identical and opposite eigenvalues are paired by different criteria, leading to fourfold degeneracies. These points can either be nodal points as described in Sec 3.6.1, or be a part of an otherwise movable nodal line. In the second case, the point in question appears on the left and right side of the semicolon, and we further highlight such points by writing them in italic font. An example is found in SG 33 with (*R-S-X*;R-U). The movable nodal line in the $k_x = \pi$ plane must pass through the point R, see Fig.3.11(b). In this SG, the point S is also fourfold degenerate. As mentioned above, this is however a true point degeneracy at the level of the movable nodal line.

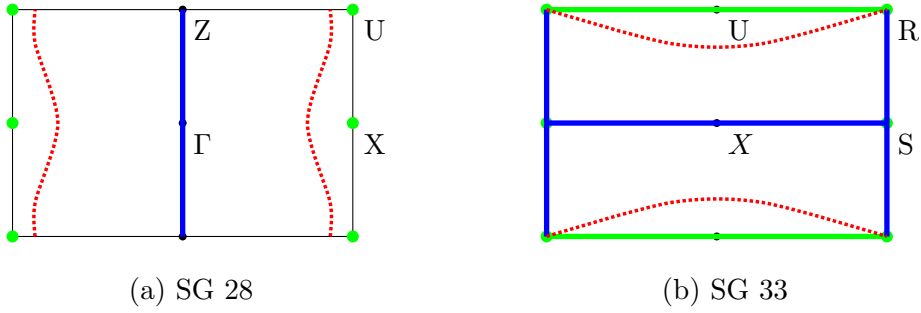


Figure 3.11: Pinned and movable lines forming an hourglass dispersion in mirror planes. Blue (green) lines have eigenvalues with opposite (equal) sign. The dashed red nodal lines are made from states with different eigenvalues. (a) Nodal lines in the mirror plane $k_y = 0$ in SG 28. Green dots are part of perpendicular nodal lines from the combination of the mirror symmetry with \mathcal{T} , which also pairs identical eigenvalues. Note that the movable line could gap itself out at the BZ boundary, splitting thereby into separate, disconnected lines around the green dots and lines. (b) Nodal lines in the $k_x = \pi$ plane of SG 33. The movable nodal line joins an intersection of two pinned nodal lines with different eigenvalue pairing at R, enforcing a fourfold degeneracy there. The point S is also fourfold degenerate, but without an hourglass dispersion between the nodal lines it is a pointlike degeneracy.

At R, the representations of the generators can be given as

$$U_{M_{100}} = i\tau_0\sigma_x, \quad (3.7.8)$$

$$U_{M_{010}} = \tau_0\sigma_y, \quad (3.7.9)$$

$$U_{\mathcal{T}\mathcal{K}} = i\tau_y\sigma_z\mathcal{K}, \quad (3.7.10)$$

and the linearized Hamiltonian in relative coordinates $\mathbf{q} = \mathbf{k} - (\pi, \pi, \pi)$ reads

$$\begin{aligned} H(\mathbf{q}) = & v_z q_z \tau_z \sigma_0 + v_x q_x \tau_z \sigma_y + v_y q_y \tau_0 \sigma_x \\ & + \lambda_x q_x \tau_x \sigma_y + \lambda_z q_z \tau_x \sigma_0, \end{aligned} \quad (3.7.11)$$

with real parameters v_i and λ_i . There are twofold degeneracies on the axes $(q_x, 0, 0)$ and $(0, 0, q_z)$, and an additional hourglass nodal line between the second and third band in the $q_x = 0$ plane, also running through $\mathbf{q} = 0$. Comparing this dispersion with the low-energy model for S, c.f., Eqs. (3.6.12), reveals the difference in pairing of eigenvalues on the $(q_y, 0, 0)$ -axis. In Figures 3.9 and 3.12 we show the dispersion around both of these points for the

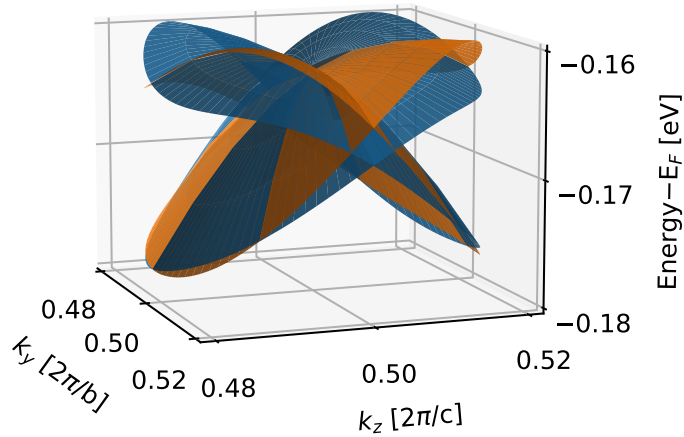


Figure 3.12: Dispersion around the point R = (π, π, π) in the $k_x = \pi$ plane in AuTlSb with SG 33. Colors indicate the relative sign of M_{100} eigenvalues. Unlike the dispersion around the point S, shown in Fig. 3.9, for the same material, there is no pointlike degeneracy.

same bands in the example material AuTlSb.

3.7.3 Interlinked nodal lines

The movable nodal lines discussed in the previous section stem from compatibility relations between high-symmetry points. Along the intersection of two mirror planes, both mirror symmetries are good quantum numbers of a band. If there are hourglass relations for both planes, they need to be fulfilled simultaneously, which leads to structures of interlinked nodal lines. Because the bands in an hourglass dispersion need to exchange, there must be an odd number of crossings. This can only be achieved, if the two nodal lines of each mirror plane intersect. With the notation introduced earlier, such situations can easily be identified by two points appearing on either side of the semicolon in two hourglass relations.

In SG 34, for example, there are movable lines defined through $(\Gamma\text{-Z-T};\text{Y})$ and $(\text{Y-S-R};\text{T})$ in the $k_x = 0$ and $k_y = \pi$ plane respectively. Both relations require a movable nodal line in the form of a loop around Y in the $k_x = 0$ plane and around T in the $k_y = \pi$ plane. On the common axis Y-T, these two loops have to touch, such that the two bands exchange only once along the axis. The two loops therefore form a so-called nodal chain [85]. A second chain is formed in the $k_y = 0$ and $k_x = \pi$ plane by $(\Gamma\text{-Z-U};\text{X})$ and $(\text{X-S-R};\text{U})$ with intersections along the common axis X-U. The same scenario is found in SG 43 with the relations $(\Gamma\text{-Z-T};\text{Y})_{k_x=0}$ and $(\Gamma\text{-Z-Y};\text{T})_{k_y=0}$. Here, the planes have to be specified explicitly, as the mirror invariant planes in the BZ of the body-centered lattice contains the same four TRIMs.

In a slightly different scenario, there can be only one loop, whereas the second nodal line wraps around the BZ boundary. For example, in SG 30, there are the relations $(\Gamma\text{-Z-T};\text{Y})$, forming a nodal loop around Y in the $k_x = 0$ plane, and $(\text{Y-S};\text{T,R})$, which can be either one movable line extending through the whole BZ facet or two loops around T and R. In either case, the loop around Y has to touch the other nodal line on the axis Y-T.

A third possibility are two loops around the same point. We call such an arrangement an armillary sphere, because the loops intersect similar to

the rings in the astronomical device. This arrangement is found in SG 110 around P, stemming from the two relations $(\Gamma\text{-Z}, X; P)$ in the $k_x = k_y$ plane and $(X\text{-M}; P)$ in the $k_x = -k_y$ plane.

Nodal line arrangement in SGs 61 and 73

In the orthorhombic SGs, there are cases where three mirror symmetries have hourglass relations, which simultaneously have to be fulfilled on three axis.

Space group 61 is a supergroup of SG 19 with inversion as an additional generator. Because of the screw rotations, spinless bands still have to fulfill the requirements of exchanging bands on one of the three rotation axis in $\Gamma\text{-X}$, $\Gamma\text{-Y}$, and $\Gamma\text{-Z}$, discussed in Sec. 3.3.3 and shown in Fig. 3.5(a). Combining inversion with the screw rotations results in glide mirror symmetries with the enforced movable nodal lines $(Y\text{-T}; T\text{-Z})$, $(Z\text{-U}; U\text{-X})$, and $(X\text{-S}; S\text{-Y})$. Each of the mirror planes contain two of the rotation axis and the nondegenerate bands have two mirror eigenvalues on these axis. For example, in the plane $k_x = 0$ bands form an hourglass dispersion for any path connecting the lines $Z\text{-T}$ and $T\text{-Y}$. This includes the path from Z to Y via Γ along the rotation axes. The same holds for the other two planes, but bands can only be exchanged an odd number of times in each mirror plane and two bands cannot be paired at two different TRIMs. This requires a minimum of three crossings on the rotation axes, all of which are part of the movable nodal lines. In Fig. 3.13(a) we show a possible arrangement of bands fulfilling all these requirements simultaneously. The representation is completely determined by the mirror eigenvalues. We encode this in the figure via the colors of the double lines, where orange corresponds to the negative sign and blue to the positive sign of the definition in Eq. (3.7.7). The rotation eigenvalue is then given by the product of the two mirror eigenvalues, i.e., positive for identical colors and negative for different ones. The exchange of bands as required from the rotation eigenvalues alone is fulfilled as well, c.f. Fig. 3.5(a). Reordering the bands in energy can move the crossings to other axis, but cannot remove them because all bands differ at least in one eigenvalue. Each crossing belongs to a movable nodal line extending into the mirror plane where the eigenvalues

differ.

In a slightly different manner, we find a compatibility relation for SG 73, which results from adding \mathcal{P} to SG 24. All mirror symmetries in SG 73 are nonsymmorphic and have k -dependent eigenvalues. This implies a sign change when connecting two identical points in the BZ, that are separated by 2π in the relevant coordinate. For example, a state with $M_{010}(0, \frac{1}{2}, \frac{1}{2})$ eigenvalue $+1$ at $Z = (0, 0, 2\pi)$ is labeled with $+$ according to the definition in Eq. (3.7.7), whereas at the equivalent point $Z' = (2\pi, 0, 0)$ a state with eigenvalue $+1$ is labeled $-$. The labels are continuously assigned in each mirror plane and therefore the bands have to exchange on any path connecting these points. On the three rotation axis connecting Γ with Z , these relations have to be fulfilled simultaneously for each pair of symmetries and at the TRIMs Γ and Z , the products of rotation eigenvalues are restricted as they

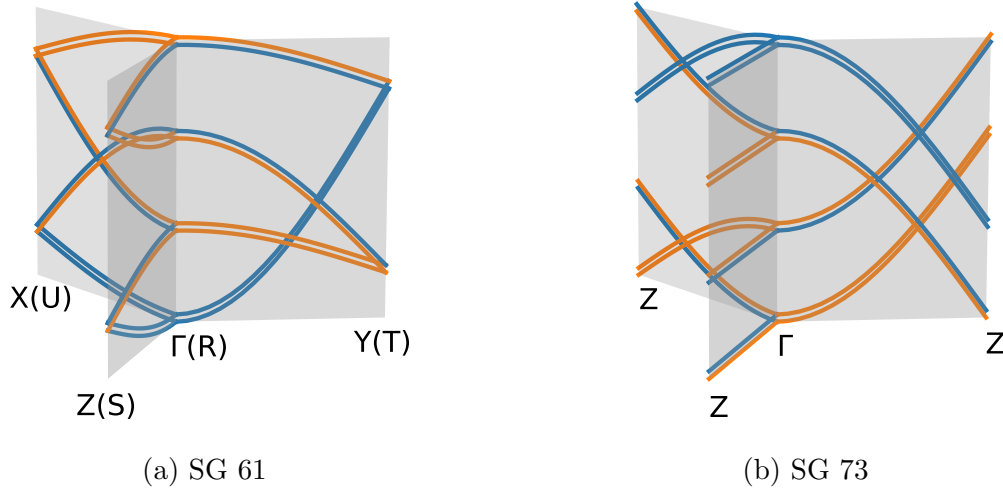


Figure 3.13: Possible arrangement of bands along three rotation axes simultaneously fulfilling three relations for hourglass nodal lines. Colors encode the sign of the mirror eigenvalues according to the definition in Eq. (3.7.7). Each crossing is part of an hourglass nodal line. (a) shows spinless bands in SG 61 for the labels Γ , X , Y , and Z . Labels in brackets corresponds to the different axes in the spinful case and each band is twofold degenerate with identical mirror eigenvalues. (b) shows a possible arrangement of spinless bands in SG 73 with a minimal number of crossings.

were for SG 24. Both conditions lead to at least six crossings on the three axes, a possible arrangement is shown in Fig. 3.13(b). Again, the crossings belong to nodal lines, which are mostly free to move in each mirror plane, but join one of the TRIMs S, R, and T, as we will show in the following section.

3.7.4 Almost movable lines

Beyond the pinned nodal lines and movable hourglass nodal lines, there is a third mechanism, that enforces nodal lines originating from TRIMs in mirror planes. Complex mirror eigenvalues $\pm i$ are paired at TRIMs by \mathcal{T} . From the little group representation it can be shown, that this crossing needs to be part of a nodal line. In the basis of mirror eigenstates, the representation for the reflection can readily be given as $U_M = i\sigma_z$. Here, it is necessary to find the restrictions on the Hamiltonian beyond the lowest order to proof that no gap can open along a line. The general gap Hamiltonian $H(\mathbf{q}) = \mathbf{d}(\mathbf{q})\boldsymbol{\sigma}$ has to be odd in the reflected coordinate for d_x and d_y and therefore only d_z can be non-zero in the mirror plane. The co-representation for time-reversal symmetry is $U_{\mathcal{T}}\mathcal{K} = i\sigma_y\mathcal{K}$ in the spinful case and it requires all terms in the Hamiltonian to be odd in \mathbf{q} . This means, $d_z(q_x, q_y, q_z = 0)$ is an odd function in the in-plane components, which means it has to vanish along a line in the plane.

This relation can also be understood from eigenvalues alone. A state $|\mathbf{q}, m = +i\rangle$ at relative momentum \mathbf{q} with mirror eigenvalue $m = i$ is mapped by \mathcal{T} to a state $|\mathbf{-q}, m = -i\rangle$ with the same energy. The same holds for the state with the opposite mirror eigenvalue. Along any path from \mathbf{q} to $\mathbf{-q}$, the two bands need to exchange smoothly. In the mirror plane, their crossing cannot be gapped because of the different mirror eigenvalues.

In the spinless case, a similar situation can be found, when \mathcal{P} or \mathcal{T} require d_z to be odd. Without further restrictions from other symmetries, such a nodal line is enforced, but can be moved in the plane freely, apart from the TRIM it is anchored to. Therefore, we call it an almost movable line [53, 54]. It is indicated in Tables II to VI again as a tuple, containing the TRIM left

of the semicolon, but only a dash to the right, since no other degeneracy might be present. The considerations above are valid in the presence of further symmetries, but often there are symmetry-enforced pinned nodal lines, which already fulfill the requirement. The nodal lines of SG 73, discussed in the previous section are all such almost movable nodal lines, the entries in Table III are (S;-), (R;-), and (T;-).

3.7.5 Dirac lines

Nodal lines also exist in spinful band structures of centrosymmetric SGs. The lines are fourfold degenerate and split into a pair of twofold degenerate bands. In analogy to the Dirac points, they are called Dirac lines and are listed in Tables IV and VI. All of the above types of nodal lines exist as Dirac lines in the orthorhombic SGs. They are formed by essentially the same mechanisms described in previous sections, However, to get a fourfold degeneracy there needs to be a pairing mechanism that is not covered by the \mathcal{PT} Kramers pairs. This can be realized by nonsymmorphic symmetries, which are additionally off-centered with respect to the inversion center.

Pinned Dirac lines in orthorhombic SGs all have a site-symmetry co-group $mm2 + \mathcal{PT}$, in which the spatial symmetries anticommute and \mathcal{PT} pairs identical eigenvalues of at least one symmetry. This can be achieved by either an anticommutation relation of $U_{\mathcal{PT}}\mathcal{K}$ with the representations of $mm2$, or via the doubling of states with identical real eigenvalues through Kramers theorem.

Almost movable Dirac lines were only found once, in SG 63 at the point $\mathbf{R} = (\pi, \pi, \pi)$. There, the mirror eigenvalues of $\pm i$ get a Kramers partner with the same eigenvalue in the whole mirror plane, because \mathcal{PT} anticommutes with the mirror symmetry. The rest of the argument is identical to the one for almost movable Weyl lines in Sec. 3.7.4.

There are also movable Dirac lines from hourglass dispersions between fourfold degenerate points and lines. In SG 60, they even form a Dirac chain [86]. In SG 61 we find an arrangement of band crossings as part of movable Dirac lines on the rotation axes through \mathbf{R} similar to the spinless

case, where the arrangement concerns the axes through Γ . With the labels R, S, T, and U in brackets, Fig. 3.13(a) describes the arrangement of Dirac lines as well. The bands are then twofold degenerate and each crossing is part of a fourfold degenerate line. The colors still describe the eigenvalues for each pair.

3.8 Enforced topology in planes

In Sec. 3.6.1 and Sec. 3.7.5 we have shown how spatial symmetries can enforce fourfold point and line degeneracies in centrosymmetric band structures. In these cases, we often find a fixed relation between the inversion eigenvalues of degenerate states at TRIMs and use them to label quantum states. At the same time, the combination of inversion eigenvalues is at the basis of defining the strong and weak \mathbb{Z}_2 indices of centrosymmetric topological insulators [87]. In this section, we show that there are some SGs with necessarily nontrivial weak invariants. This means that some two-dimensional slices of the BZ with a band gap are topological insulators and must therefore have in-gap surface states. The weak invariant is calculated from the symmetry indicators δ_i for each TRIM Γ_i , defined as $\delta_i = \prod_{m=1}^{N/2} \xi_{2m}(\Gamma_i)$, where m indexes one member of each occupied Kramers pair and runs therefore only over one half of the N states in the degeneracy. This definition makes use of the fact that Kramers partners always share the same inversion eigenvalue. The fourfold degeneracies were previously often written in terms of the inversion eigenvalues and we find the two possibilities $\delta_i = -1$ for pairs $(+, +, -, -)$ and $\delta_i = +1$ for pairs $(+, +, +, +)$ or $(-, -, -, -)$. If there is a gap in a plane that has four TRIMs, the weak \mathbb{Z}_2 invariant ν is then defined through the product of all their δ_i , $(-1)^\nu = \prod_i \delta_i$.

For ν to be nonzero, there must be only one or only three TRIMs, where four identical inversion eigenvalues are paired. In the example of the double Dirac point of SG 130, we have already shown how glide mirror symmetries and time-reversal symmetry can enforce such a fourfold degeneracy. Without the fourfold rotation symmetry the three mirror symmetries generate SG 56 and there is no eightfold degeneracy at $R = (\pi, \pi, \pi)$. Instead, one finds

two sets of fourfold degenerate states with identical eigenvalues in each set, i.e., $\delta_R = +1$. All other TRIMs with the exception of Γ are also fourfold degenerate and have $\delta_i = -1$. Translational components of glide mirror symmetries are irrelevant for representations at Γ and they are therefore always twofold degenerate pairs $(+, +)$ or $(-, -)$. Therefore, no definite statement can be made for δ_Γ for four occupied bands, because either value is possible by arranging the bands accordingly. There are three high-symmetry planes in the BZ that include R, but not Γ . Indicated by their four TRIMs, they are ZURT, XUSR and YTSR. The first one is not gapless, as there are symmetry-enforced movable Dirac points in the axis Z-U and Z-T. In the absence of accidental crossings, the latter two planes have a gap between the fourth and the fifth band in each gap and fulfill necessarily all the criteria of a weak topological insulator.

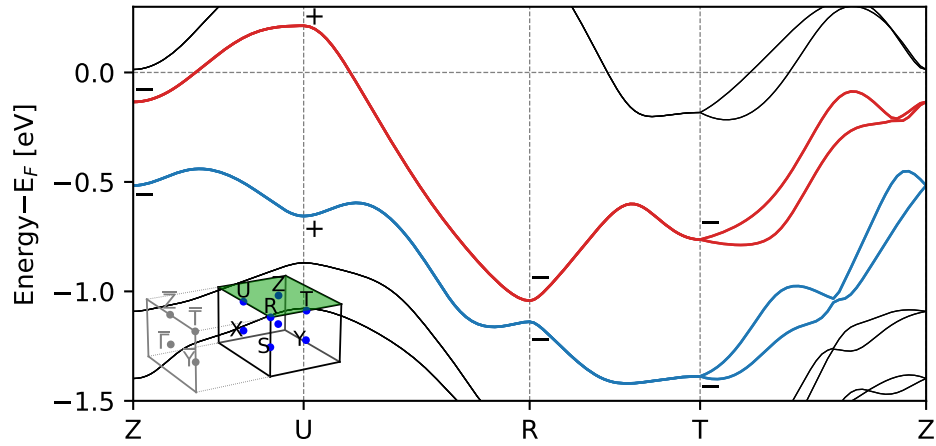
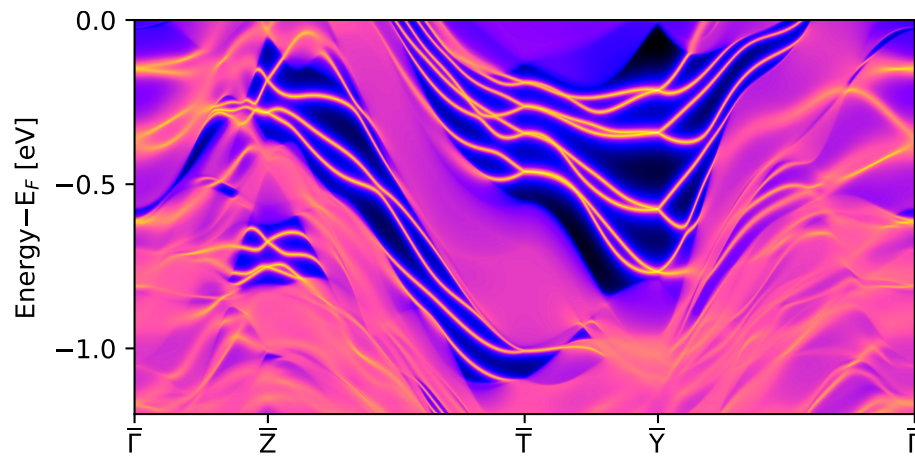
This mechanism can also be found in the orthorhombic SGs 52 and 60–62, as well as the tetragonal SG 138. We indicate these nontrivial planes in Tables IV and VI in the above notation and highlighted the TRIMs where four identical eigenvalues are paired.

In the search of suitable candidate materials, one has to identify the gap corresponding to one elementary band representation of eight bands. These can be identified from knowing the full connectivity of bands. In almost all examples, an elementary band representation is tied together by a movable Dirac point or line, as can be easily verified from our comprehensive tables. For the existence of surface states, it is necessary to have a gap. This is, however, not sufficient, because there might be no surface where the gap of the nodal plane is preserved under the projection of all bulk bands. Therefore, one needs to identify candidates by carefully inspecting the band structures within the nontrivial plane.

In Fig. 3.14, we present Ir_2Si as an example. This material crystallizes in SG 62 with the two nontrivial planes ZURT and XUYT. However, only the gap in the former is preserved for open boundary conditions on a (100) surface. Figure 3.14(a) shows the dispersion in the plane ZURT. The blue and red band belong to the same EBR and at each TRIM we labeled the bands with the corresponding δ_i . Note that the lines Z-U-R-T are pinned

Dirac lines. The inset shows the full BZ with the nontrivial plane highlighted in green, together with the surface BZ for the finite system. The plane ZURT projects onto the segment $\bar{Z}-\bar{T}$ and surface states crossing the gap can be seen there in the local density of states (LDOS) calculation for the surface, shown in Fig. 3.14(b).

As a second example, we present Sr_2Bi_3 , crystallizing in SG 52. In this SG, there is no enforced nontrivial weak invariant, because the representations at T are only twofold degenerate with pairs $(+, +)$ or $(-, -)$. The value δ_T can take either value, depending on the actual representation and ordering of bands. The spinless representations, however, are also all twofold degenerate with identical inversion eigenvalue. Including SOC splits these into two sets of identical eigenvalues, because the inversion eigenvalue is not changed. This implies, that for small SOC relative to the splitting of spinless bands, we find $\delta_T = +1$ and thereby a nontrivial weak invariant. In Fig. 3.15 we show the two bands above and below the Fermi energy, together with the symmetry indicators δ_i for each TRIM in the plane ZURT. The bulk gap is preserved in the spectrum of a (100) termination, where the plane is mapped to the line $\bar{Z}-\bar{T}$. The LDOS of the surface clearly shows the two surface states in the gap. They are related by time-reversal symmetry, which also ensures the twofold degeneracy at the TRIMs. A similar situation is also found in SGs 56, 60 and 62, which are highlighted in Table III with the entry “precedes \mathbb{Z}_2 invariant (with SOC)” in the column “notable features”.

(a) Bulk bands in the $k_z = \pi$ plane

(b) Surface density of states on the (100)-surface

Figure 3.14: Symmetry-enforced weak topology in Ir_2Si . The sign of the product of inversion eigenvalues is shown in (a) for the bands of the first EBR below the Fermi energy at all TRIMs in the plane ZURT. The nontrivial plane is mapped onto the line $\bar{Z}-\bar{T}$. A pair of time-reversal symmetric surface states connect the bands below the projected bulk gap to the upper ones in the surface density of states shown in (b). Figure adapted from Ref [54].

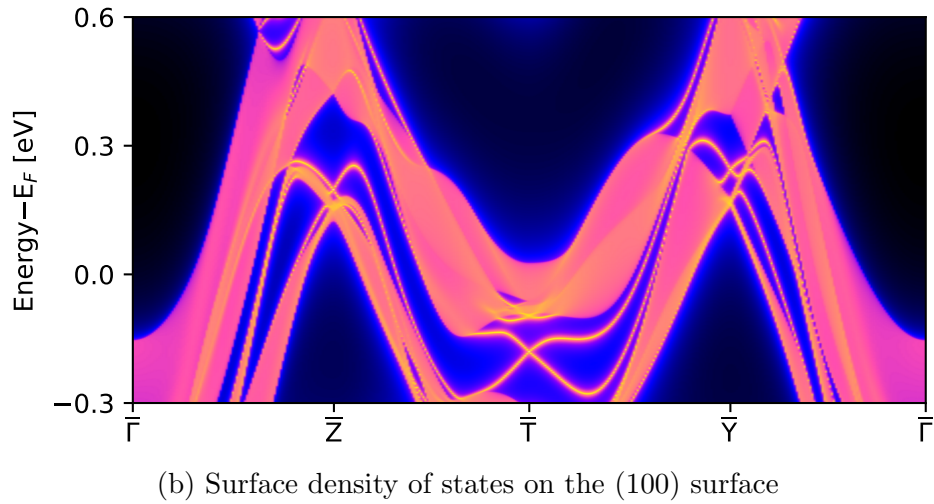
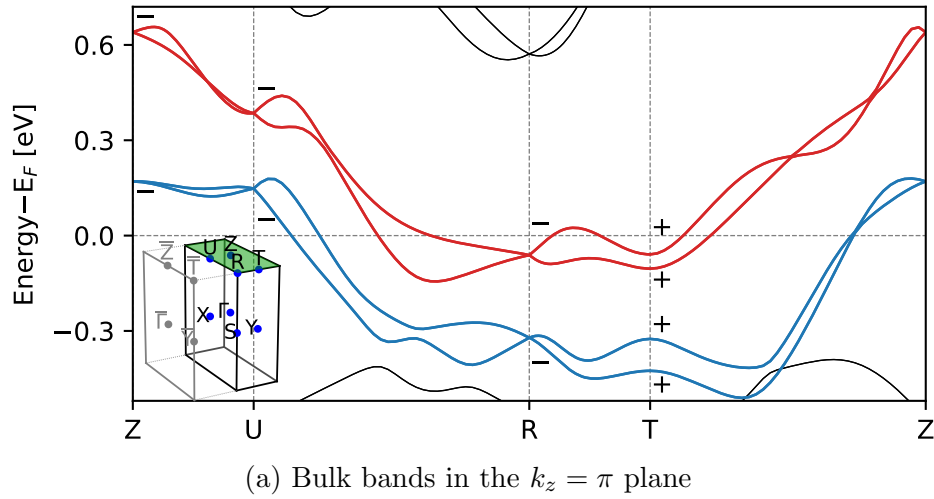


Figure 3.15: Symmetry-enforced weak topology in Sr_2Bi_3 in the plane $k_z = \pi$. The symmetry indicators δ_i at each TRIM in the nontrivial plane are shown in (a) for each band in the EBR crossing the Fermi energy. The nontrivial plane maps on the line \bar{Z} - \bar{T} , see inset in (a). Two surface states crossing the projected bulk gap in this segment can be seen in the surface density of states in (b). Figure adapted from Ref [54].

3.9 Summary

In this chapter we explored various types of symmetry-enforced band crossings and presented the results of a systematic and exhaustive search in orthorhombic and tetragonal SGs with time-reversal symmetry. The analysis is based on symmetries alone and relied extensively on representation theory of symmetry groups, as introduced in Sec. 2.1. It therefore applies to all translation invariant systems with the symmetries of one of these SGs. For each type of degeneracy, we explained the pairing mechanism and explored the topological invariants. The main results are collected in the comprehensive Tables I – VI, presented in Appendix B.

The extensive search revealed interesting new types of topologically protected crossings. Nonsymmorphic SGs proved to be a very interesting subset of SGs, rich in band crossings that cannot be understood from the local little group alone and are therefore easily overlooked. The analysis of compatibility relations along the whole band structure reveals the movable crossings, which can alternatively be understood from their \mathbf{k} -dependent eigenvalues. Their existence is enforced, even though there is some freedom in the exact location in the BZ. Especially the chiral nonsymmorphic SGs show exceptional topology with higher-order Weyl points and topologically charged nodal planes, e.g., the fourfold degenerate point crossing with a Chern number of $\mathcal{C} = \pm 4$ in SGs 92/96 and topologically charged nodal plane duos with a Chern number of at least $\mathcal{C} = \pm 2$ in SG 94. Unfortunately, they seem to be seldom realized in real materials and we hope to inspire additional research towards the growth of new (meta-)materials with these symmetries.

Understanding the interplay of symmetries and the resulting topology reveals the robustness of the degeneracy against symmetry breaking perturbations. This was demonstrated for several examples of SU(2) symmetry breaking, which shows the connection between spinless and spinful band structures in the presence or absence of SOC, respectively. The detailed description in terms of local representations, eigenvalues and compatibility relations provides a valuable toolkit for extending this analysis to other SG families and magnetic SGs, which lie beyond the scope of this work.

4. Quasiparticle interference of drumhead surface states

In the next two chapters we will describe consequences and observable effects of nodal-line semimetals (NLSM), starting with the surface states of nodal loops. These are two-dimensional and bounded by the projection of the nodal line, resembling a drumhead. We will introduce a two-band model for the NLSM. Taking nonzero SOC into account extends this model to four bands, which can have two split nodal lines or a finite gap. We discuss the symmetry protection of the nodal loop and its topological invariants.

We then discuss how this might lead to the drumhead surface states. Finally, we calculate the patterns formed by these drumhead surface states in quasiparticle interference patterns [88]. We will also demonstrate how SOC leads to spin-polarized drumhead surface states, that can be resolved by spin-sensitive measurements of the quasiparticle interference at magnetic impurities.

4.1 Nodal loops

A nodal-loop semimetal has a band crossing along a one-dimensional loop in the Brillouin zone. Parameter counting for a general two band model

$$H(\mathbf{k}) = \bar{\varepsilon}(\mathbf{k}) \cdot \tau_0 + \mathbf{d}(\mathbf{k}) \cdot \boldsymbol{\tau} \quad (4.1.1)$$

shows that for a nodal line in a three-dimensional material, the image space of the vector $\mathbf{d}(\mathbf{k})$ needs to be restricted to a two-dimensional manifold. This

restriction can be imposed by one of two spatial symmetries, inversion or reflection symmetry, combined with time-reversal symmetry \mathcal{T} . While the former allows for nodal lines anywhere in the BZ, the latter one restricts them to mirror planes. Throughout this and the following chapter, we will deal with the second case protected by the mirror symmetry M_z and time-reversal symmetry.

In contrast to the previous chapter, these nodal loops are protected by symmetry, but not enforced. A mirror or inversion symmetry allows for the definition of a topological \mathbb{Z}_2 invariant, protecting the nodal line against small symmetry-preserving perturbations. A large deformation of bands can however remove the nodal line by shrinking it to a point. Alternatively, the nodal line can be removed by bringing it into contact with a second nodal line, which is reflected in the \mathbb{Z}_2 invariant. Such nodal lines have been found for example in CaP_3 [89], CaAgP and CaAgAs [90–92] and the latter two materials serve as motivation for the minimal model.

A simple two-band model with a nodal loop can be induced from two sites separated by half a lattice constant $\frac{1}{2}\mathbf{c}$. Additionally, we require the site-symmetry representation on one site to be odd under reflection, the other one being even. An illustration is presented in Fig. 4.1(a). In a hexagonal lattice system, the entries in the Hamiltonian with next nearest neighbor hopping in \mathbf{c} -direction and nearest neighbor hopping perpendicular to it can be given as

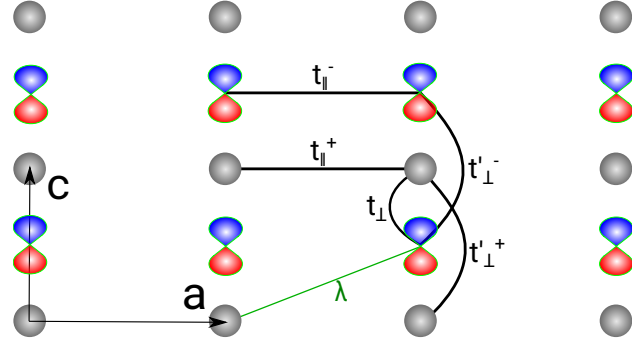
$$\begin{aligned} \bar{\varepsilon}(\mathbf{k}) &= 2t_{\parallel}(\cos(\mathbf{k} \cdot \mathbf{a}) + \cos(\mathbf{k} \cdot \mathbf{b}) + \cos(\mathbf{k} \cdot (\mathbf{a} + \mathbf{b}))) \\ &\quad + 2t'_{\perp} \cos(\mathbf{k} \cdot \mathbf{c}) + \mu \end{aligned} \quad (4.1.2)$$

$$\begin{aligned} d_z(\mathbf{k}) &= 2\delta t_{\parallel}(\cos(\mathbf{k} \cdot \mathbf{a}) + \cos(\mathbf{k} \cdot \mathbf{b}) + \cos(\mathbf{k} \cdot (\mathbf{a} + \mathbf{b}))) \\ &\quad + 2\delta t'_{\perp} \cos(\mathbf{k} \cdot \mathbf{c}) + \delta\mu \end{aligned} \quad (4.1.3)$$

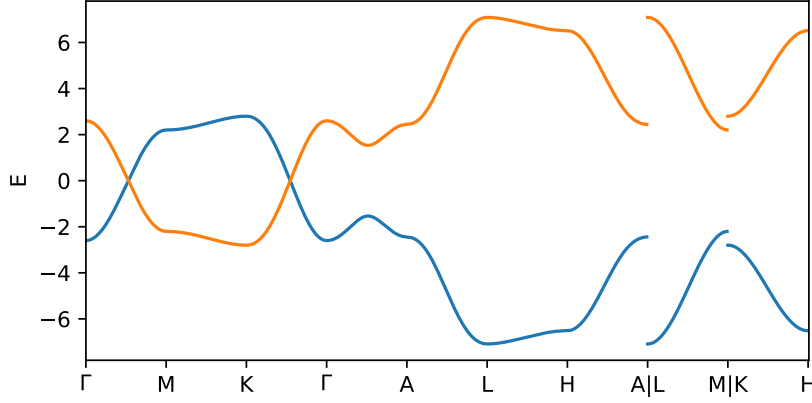
$$d_y(\mathbf{k}) = 2t_{\perp} \sin\left(\frac{1}{2}\mathbf{k} \cdot \mathbf{c}\right) \quad (4.1.4)$$

$$d_x = 0 \quad (4.1.5)$$

The hopping strength in the plane spanned by \mathbf{a} and \mathbf{b} for each band is given by $t_{\parallel} \pm \delta t_{\parallel}$, the coupling between the two orbitals is given by the nearest



(a) Slice of the crystal structure in the \mathbf{a} - \mathbf{c} -plane, where $t_{\parallel}^{\pm} = t_{\parallel} \pm \delta t_{\parallel}$, $t_{\perp}^{\pm} = t_{\perp} \pm \delta t_{\perp}$.



(b) Dispersion for $t_{\parallel} = t'_{\perp} = \mu = 0$, $\delta t_{\parallel} = -0.6$, $\delta t'_{\perp} = -1.0$, $\delta\mu = 3$, $t_{\perp} = -0.5$. The BZ with the shape of the nodal loop is shown in Fig. 4.2.

Figure 4.1: Illustration and dispersion of the nodal-loop model defined in Eq. (4.1.5).

neighbor out-of-plane hopping strength t_{\perp} and the intra-orbital next-nearest hopping strength $t'_{\perp} \pm \delta t'_{\perp}$. A nodal line is formed, when the difference in on-site energy is smaller than the difference in bandwidth, i.e., $-\delta t_{\perp} < \delta\mu < \delta t_{\perp}$. The nodal line forms a loop around Γ or K .

In this basis, the reflection M_{001} has the matrix representation $U_{M_{001}} \propto \tau_z$ in the $k_z = 0$ plane due to the different representations at the two sites. This requires the off-diagonal entry in the Hamiltonian to be odd in k_z and vanish in the $k_z = 0$ plane. In the other invariant plane $k_z = \pi$, the representation is proportional to the identity, $U_{M_{001}} \propto \tau_0$, because the reflection maps one site

to another unit cell and acquires thereby an additional translation eigenvalue of -1 . Consequently, the off-diagonal entry needs to be even in $q_z = k_z - \pi$. Therefore, the nodal line is protected by the different symmetry eigenvalues in the former case, but not in the latter.

Further crystalline symmetries are encoded in ε_{\parallel} , but they are not central for the following discussion.

4.2 Berry phase and surface states

The topology of a nodal line in a three-dimensional system ($d = 3$) is characterized on a loop, i.e., a sphere S^D with $D = d - d_{\text{defect}} - 1 = 1$ [14]. The topological invariant is the Berry phase P_{γ} calculated by a line integral of the Berry curvature of the lower band along paths γ that encircle the line degeneracy,

$$P_{\gamma} = -i \int_{\gamma} \langle u_{\mathbf{k}}^- | \nabla_{\mathbf{k}} | u_{\mathbf{k}}^- \rangle \cdot d\mathbf{l}. \quad (4.2.1)$$

The value of this integral does not change for smooth deformations of the path, as long as no degeneracy is encountered. On paths that do not wrap the nodal line, the Berry phase must vanish, since these can be smoothly shrunk to a point without encountering a degeneracy. In Fig. 4.2 we show two equivalent paths around a nodal loop. The circle can be continuously deformed into the two straight lines. The dashed sections lie in the equivalent planes $k_z = \pm\pi$ and their contributions to the line integral cancel due to the opposite orientation. Each straight segment can be evaluated independently,

$$P(k_x, k_y) = -i \int_{-\pi}^{\pi} dk_z \langle u_{\mathbf{k}}^- | \partial_{k_z} | u_{\mathbf{k}}^- \rangle. \quad (4.2.2)$$

In the gauge of the cell-periodic functions $|u_{\mathbf{k}}(\mathbf{r} + \mathbf{c})\rangle = |u_{\mathbf{k}}(\mathbf{r})\rangle$, this is the Zak phase of one-dimensional subsystems indexed by the remaining momentum components [6]. In this gauge, however, the Hamiltonian and its eigenstates are not periodic in \mathbf{k} . This expression is directly linked to the

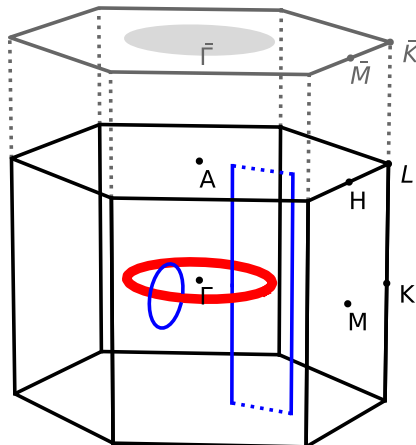


Figure 4.2: Bulk and surface BZ for the nodal-loop system defined in Eq-(4.1.5). Nodal loop (red) in the $k_z = 0$ plane encircled by topologically equivalent paths (blue). The dashed blue lines are identical segments whose contributions cancel. The gray patch in the surface BZ is the area bounded by the projection of the nodal line and hosts the drumhead surface states.

expression for the center of the Wannier function within the unit cell [93],

$$P(k_x, k_y) = \frac{2\pi}{|\mathbf{c}|} \left\langle w_{k_x, k_y}^- \left| \hat{z} \right| w_{k_x, k_y}^- \right\rangle. \quad (4.2.3)$$

Here, $|\mathbf{c}|$ is the height of the unit cell and we constructed the Wannier function in the unit cell at the origin ($\mathbf{R} = 0$) by a partial Fourier transformation

$$\left| w_{k_x, k_y}^- \right\rangle = \frac{V\sqrt{N}}{(2\pi)^3} \int_{-\infty}^{\infty} dk_z \left| u_{\mathbf{k}}^- \right\rangle. \quad (4.2.4)$$

The mirror symmetry restricts the center of the Wannier function to one of two invariant coordinates, 0 or $\frac{|\mathbf{c}|}{2}$, and quantizes the Zak phase of the straight path to 0 or π . There is however only a direct link between the quantized Zak phase and surface states, if the system can be terminated at a reflection center. In this model, both atoms reside in mirror planes and the system can therefore not be terminated at a reflection center. Furthermore, every termination either breaks global reflection symmetry or requires half

a unit cell at one end, see Fig. 4.1(a). In this scenario, the bulk-boundary correspondence cannot be applied [94, 95].

In order to illustrate the connection between the Zak phase of a one-dimensional subsystem and the Berry phase in this case, we rewrite the one-dimensional gap Hamiltonian as

$$H(k_z) = (m + 2t' \cos k_z)\tau_z + t \sin \frac{k_z}{2}\tau_y. \quad (4.2.5)$$

Neglecting any uniform dispersion does not influence the energy eigenstates. The parameter m contains all terms depending on the remaining components \mathbf{k}_{\parallel} and we dropped the subscript \perp in the hopping parameters. The existence of surface states is independent of the total energy scale and we can express all parameters in multiples of t' for now. The gap closes only for $m = -2t'$, marking the only point where the quantized Zak phase can change. For positive t' and $m > 2t'$, the Zak phase is π and we find two in-gap states for the open chain. They are exponentially localized to either side of the open chain. Their energies differ due to the different termination on either side. Their decay length grows with increasing m . At the same time, the states approach the upper and lower bulk bands. Eventually, they merge and become indistinguishable from bulk states. This transition is not topological and the surface state cannot be claimed to be topologically protected. This transition happens at $m = 2 + t^2$, and since t is usually substantially larger than t' due to the smaller real space distance, the surface state often exist in a wide range of values for m without ever merging into the bulk states in NLSMs with drumhead surface states. For negative t' , we find the same situation, only now the surface state is in the region $m < -2t'$, that is, in a region where the Berry phase is 0. In the third scenario $t' = 0$, the gap closing coincides with the merging of the surface states with the bulk and there is no surface state at all.

The Zak phase can be decomposed into the dipole moment of the unit cell P_{cell} and a contribution ΔQ of surface charges to the total polarization via the unitary transformation $U = \sum_i |i\rangle e^{ik_z z_i} \langle i|$, which adds a phase to each orbital $|i\rangle$ depending on its position z_i in the unit cell [96]. This decomposition is

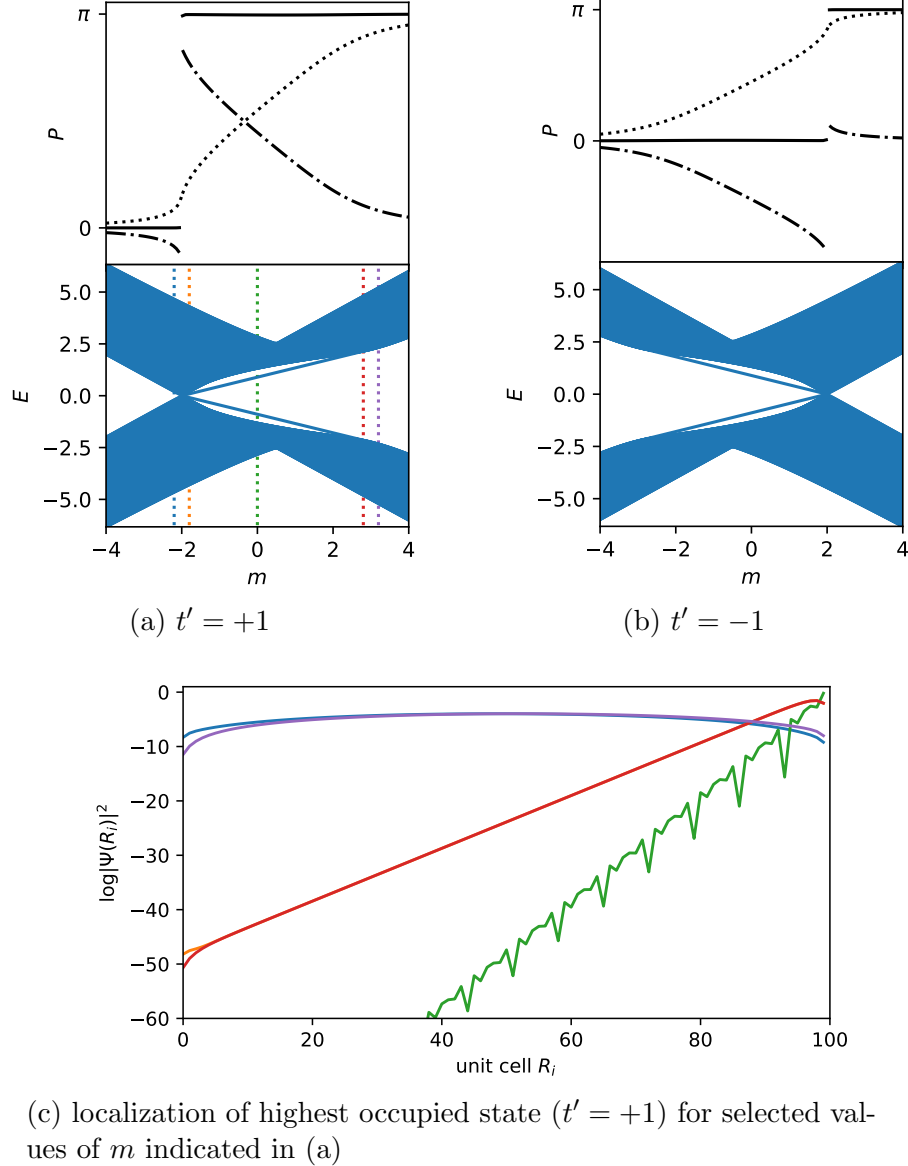


Figure 4.3: Surface states of the simplified model of an open chain. (a) and (b) The upper plot shows the Zak phase (continuous line) and its individual contributions ΔQ (dash-dotted) and the polarization of the unit cell (dotted). The surface states can show up on either side of the crossing, not necessarily where the Zak phase is non-zero. The surface state merges with the bulk around $m = \pm(2 + t^2) = \pm 3$. Without next-nearest neighbor hopping ($t' = 0$) this point coincides with the gap closing point at $m = 0$ and there is no surface state on either side. (c) Local weight of the lowest occupied state in each unit cell in the finite system for $t' = +1$ for selected values $m \in \{-2 \pm 0.2, 0, 3 \pm 0.2\}$. The state is only exponentially localized for $g_2^2 > m > 3$. In the case $t' = -1$ we find the same situation with the substitution $m \rightarrow -m$ and the surface state lower in energy is localized on the other end.

not gauge invariant and depends on the choice of origin and unit cell. With this transformation, Eq. (4.2.3) reads

$$\begin{aligned}
 P &= -i \int_{-\pi}^{\pi} dk_z \langle u_{\mathbf{k}}^- | U^\dagger \partial_{k_z} U | u_{\mathbf{k}}^- \rangle - \langle u_{\mathbf{k}}^- | U^\dagger (\partial_{k_z} U) | u_{\mathbf{k}}^- \rangle \\
 &= -i \int_{-\pi}^{\pi} dk_z \langle \tilde{u}_{\mathbf{k}}^- | \partial_{k_z} | \tilde{u}_{\mathbf{k}}^- \rangle + 2\pi \sum_i z_i |\langle i | u_{\mathbf{k}}^- \rangle|^2. \quad (4.2.6)
 \end{aligned}$$

The surface charge ΔQ is given by the first term, which is formally equivalent to the definition of the Zak phase, but in the gauge of the k -periodic wave function $|\tilde{u}_{\mathbf{k}}\rangle = |\tilde{u}_{\mathbf{k}+\mathbf{K}}\rangle$. This expression is not quantized any longer. It can be interpreted as an excess charge in one half of the finite system, exponentially localized at the surface for a sufficiently large system. Note that the value of a closed loop not wrapping around the Brillouin zone edges is independent of gauge choice.

In Figures 4.3(a) and 4.3(b) we show the dispersion of the open chain for different values of m in the two scenarios. Figure 4.3(c) shows the localization of the first state below the gap for selected values of m . Surface states have the highest weight close to one end and decay exponentially in the bulk. The first state above the main gap is localized at the opposite end. The existence of a localized surface state corresponds to regions with large ΔQ . The total polarization given by the Zak phase can vanish however, when the dipole moment of the unit cell cancels this contribution. Without second neighbor hopping, $t' = 0$, there is no surface state on either side despite the jump in Berry phase [94, 97, 98].

For the full nodal-loop model defined in Eq. (4.1.5), we find an exponentially localized surface state in the whole region bound by the projection of the nodal line as indicated by the gray circle in the surface BZ shown in Fig. 4.2. Because of their shape, they are called drumhead surface states [99]. From a topological point of view there is no difference between the inside of the loop and the outside on the two-dimensional torus $k_z = \pi$ and a drumhead surface state could also be centered around \mathbf{K} .

4.3 Spin-orbit coupled nodal-loop semimetal

Including spin degrees of freedom extends the model of a nodal-loop semimetal introduced in Eq. (4.1.5) to a four-band model,

$$H = \begin{pmatrix} H(\mathbf{k}) & \Lambda(\mathbf{k}) \\ \Lambda^\dagger(\mathbf{k}) & H^*(-\mathbf{k}) \end{pmatrix}, \quad (4.3.1)$$

where the additional symmetry-allowed terms due to SOC are

$$\Lambda(\mathbf{k}) = \left(e^{-i\frac{2\pi}{3}} \sin(\mathbf{k} \cdot \mathbf{a}) + e^{+i\frac{2\pi}{3}} \sin(\mathbf{k} \cdot \mathbf{b}) - \sin(\mathbf{k} \cdot (\mathbf{a} + \mathbf{b})) \right) \\ \times (\lambda_{\text{inter}} 2 \cos(\frac{1}{2} \mathbf{k} \cdot \mathbf{c}) \tau_x + \lambda_{\text{intra}} \tau_z)$$

The dispersion is of the Rashba-type, $\propto (k_y \sigma_x - k_x \sigma_y)$ for small momenta. The inter-orbital term $\propto \lambda_{\text{inter}} \tau_x$ is an intrinsic contribution, which can be non-zero without breaking the bulk symmetries and does not remove the spin degeneracy of bulk bands, because Kramers theorem still holds. Because the nodal line is protected by a \mathbb{Z}_2 invariant, the coupling of spin spaces results in a gapped line, although all symmetries are preserved. Regardless of the sign of λ_{inter} , the system is turned into a mirror Chern insulator, characterized by a mirror Chern number, evaluated in the $k_x = 0$ plane or symmetrically equivalent ones [95]. This leads to a pair of chiral surface states, which is well defined in the limit of vanishing SOC. At the surface, inversion symmetry is broken and the surface states are not spin degenerate, except at TRIMs. In Fig. 4.4(a) we show the LDOS at the surface of a slab with open boundary conditions in the [001] direction, calculated via the spectral function weighted by the expectation value of the projection operator \hat{P}_{bottom} on the lower three layers of the slab,

$$\rho(\omega, \mathbf{k}_{\parallel}) = \sum_i \text{Im} \frac{\langle \Psi_{\mathbf{k}_{\parallel}}^i | \hat{P}_{\text{bottom}} | \Psi_{\mathbf{k}_{\parallel}}^i \rangle}{\omega - E_i + i\epsilon}. \quad (4.3.2)$$

The term $\propto \lambda_{\text{intra}} \tau_z$, on the other hand, acts within each orbital space. This term can only be nonzero if inversion and the mirror symmetry are

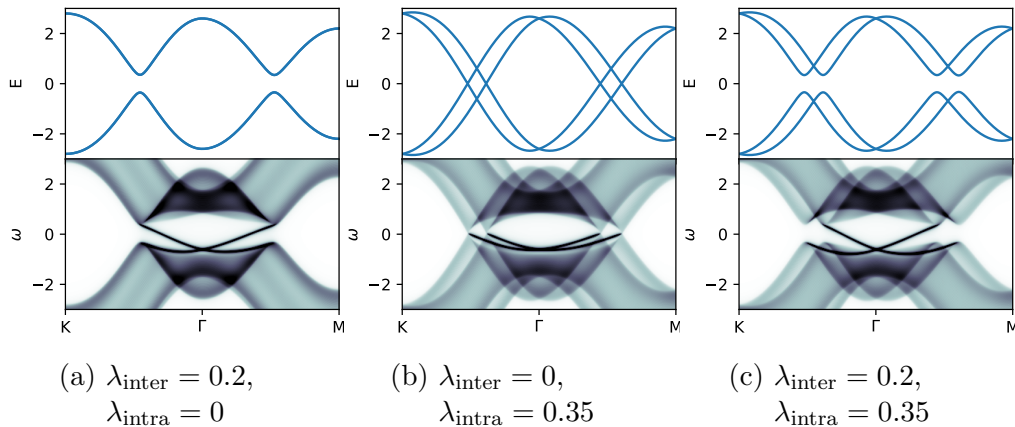


Figure 4.4: Dispersion in the $k_z = 0$ plane (top) and surface density of states (bottom) for the NLSM for intrinsic, Rashba and combined SOC contributions. Parameters are identical to the ones in Fig. 4.1(b).

broken, either by finite size effects or by some perturbation. It lifts the spin degeneracy in the bulk without removing the nodal line. With this term alone, the nodal loop splits into two separate concentric nodal lines, see Fig. 4.4(b). With both terms non-zero, the two nodal lines become also gapped. Since this situation can be smoothly connected to the first case with the intrinsic contribution only, they are topologically equivalent and the chiral surface states cross the gap in the same way, shown in Fig. 4.4(c).

4.4 Quasiparticle interference

Due to the high weight on the surface, the drumhead surface states are expected to dominate surface effects. In this section, we will calculate the quasiparticle interference (QPI) patterns of a nodal-loop semimetal with drumhead surface states, resulting from elastic scattering on a pointlike surface impurity [100–102]. QPI patterns can be experimentally obtained from Fourier transformed spatial modulations in the tunneling current of scanning tunneling microscope (STM) measurements.

In the following, calculations are done in a slab geometry with periodic boundary conditions in the plane spanned by \mathbf{a} and \mathbf{b} , indexed by the 2-dimensional crystal momentum \mathbf{k}_{\parallel} . In the perpendicular direction

we perform a partial Fourier transformation to the real space coordinate z and choose open boundary conditions with the NLSM being located at $0 \leq z \leq N_{\text{layers}}$. The spatial coordinate z is given in terms of the unit cell height $|\mathbf{c}|$.

The surface impurity is modeled as a pointlike potential in the directions perpendicular to the surface and exponentially decaying with decay length a_0 into the system perpendicular to the termination,

$$V = \delta(\hat{x})\delta(\hat{y})\frac{V_0}{a_0}e^{-i\frac{z}{a_0}} \quad (4.4.1)$$

The Fourier transformed spatial fluctuations $\delta N(\mathbf{q}, \omega)$ of the tunneling current for a given bias ω around a surface impurity, can be directly related to the change in Greens functions of the perturbed Hamiltonian $H = H_0 + V$ compared to the unperturbed system [102]. We work in the regime of a weak scattering potential, such that the Born approximation $G - G_0 = G_0 V G_0$ is justified.

For a given instrument response function $F(z)$, the QPI patterns $\rho(\mathbf{q}, \omega)$ are then defined through

$$\begin{aligned} \rho(\mathbf{q}, \omega) &= i(\Lambda(\mathbf{q}, \omega) - \Lambda(-\mathbf{q}, \omega)^*), \\ \Lambda(\mathbf{q}, \omega) &= \int dz F(z) \frac{1}{N} \sum_{k_{\parallel}} \text{Tr} \left(G_{\mathbf{k}_{\parallel}}(\omega, z) V(z) G_{\mathbf{k}_{\parallel} + \mathbf{q}}(\omega, z) \right) \\ &= \frac{1}{N} \sum_{k_{\parallel}, i, j} \text{Tr} \left(\frac{\langle \Psi_{k_{\parallel} + \mathbf{q}}^j | \hat{F} | \Psi_{k_{\parallel}}^i \rangle \langle \Psi_{k_{\parallel}}^i | \hat{V} | \Psi_{k_{\parallel} + \mathbf{q}}^j \rangle}{(\omega - E_i(k_{\parallel}) + i\varepsilon)(\omega - E_j(k_{\parallel} + \mathbf{q}) + i\varepsilon)} \right) \end{aligned} \quad (4.4.2)$$

We model the instrument response as being sensitive to the first z_0 layers, $F(z) = \Theta(z - z_0)$ and local in the perpendicular directions. Qualitatively, the resulting QPI patterns can be understood as a convolution of states weighted with their overlap in the surface layers and their spectral weight. The strongest contributions are therefore expected for nesting vectors \mathbf{q} of twice the radius of the drumhead surface state for a constant energy cut at the bias voltage, $E_i(\mathbf{k}_{\parallel}) \approx E_j(\mathbf{k}_{\parallel} + \mathbf{q}) \approx \omega$. In Fig. 4.5 the QPI patterns for the spinless NLSM is shown for three different bias voltages. The strongest

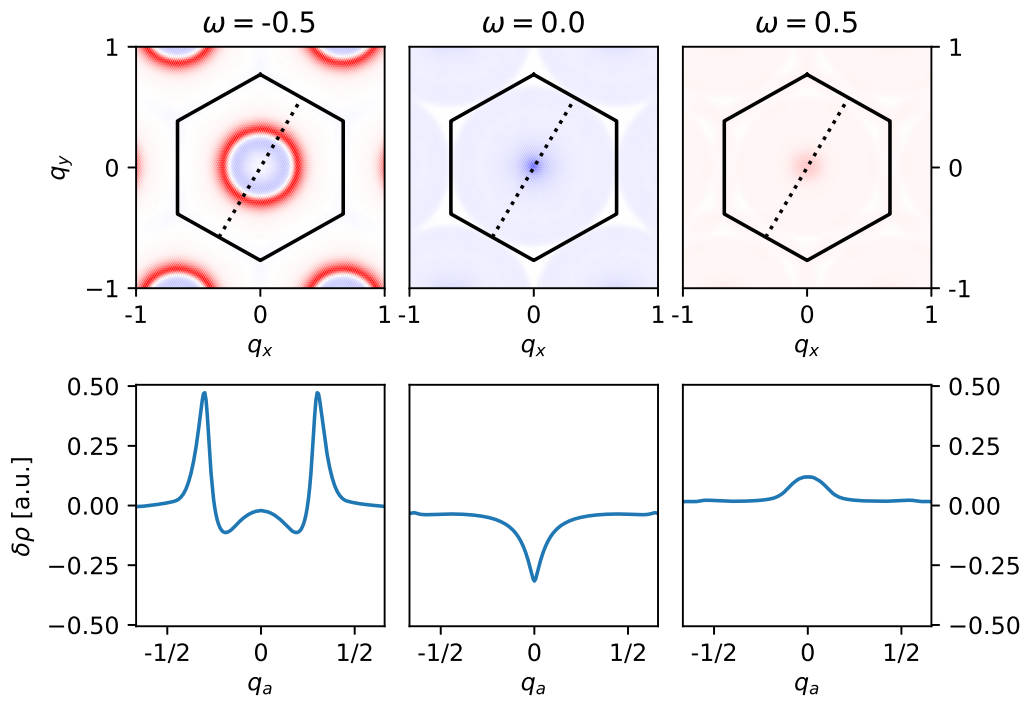


Figure 4.5: QPI patterns for the spinless case at different bias $\omega = -0.5$, 0.0 , and $+0.5$. The axis in the color plot are (q_x, q_y) in units of $\frac{\pi}{a}$. The lower plot shows a cut along the dashed line. The parameters of the Hamiltonian are identical to the ones in Fig. 4.1(b). Figure adapted from Ref. [88].

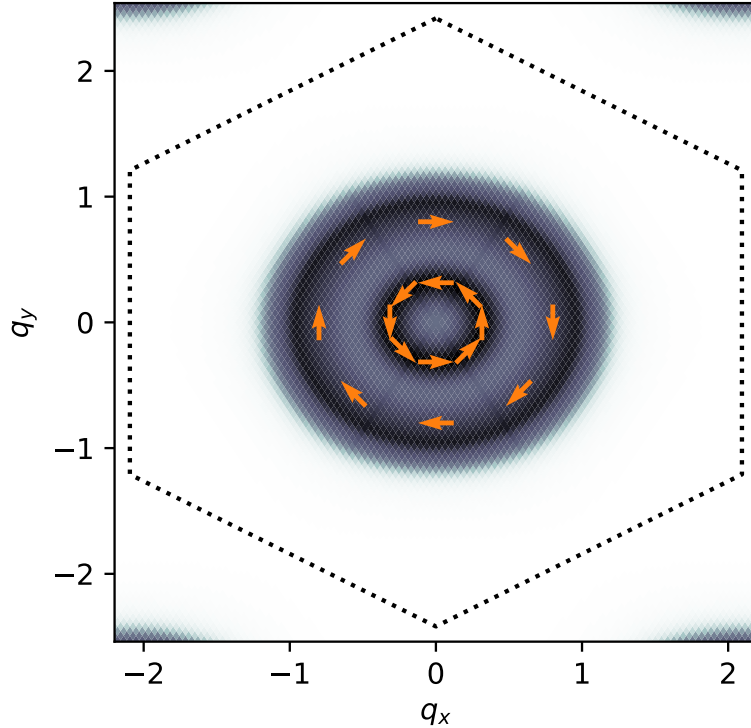


Figure 4.6: LDOS at constant $\omega = -0.5$ with SOC. Parameters are the same as in Fig. 4.4(b). Arrows show the spin polarization of the surface states.

response can be seen for $\omega = -0.5$, where the surface state is well localized. Note, that the radius of the drumhead surface state at this energy is approximately half of the radius of the nodal line. At the same distance from the Fermi level in the opposite direction, only bulk states contribute and there is no strong response, because bulk states have very little weight on the surface.

The pattern does not change much upon inclusion of SOC in the centrosymmetric case. Even though, there are now two nondegenerate drumhead surface states with distinct radii at constant energy ω , the QPI pattern shows only one ring. This becomes clear from the spin structure of the surface state. Since the impurity potential and instrument response function are diagonal in the spin indices, the only contribution arises from nesting vectors \mathbf{q} connecting the two rings. In Fig. 4.6 we show the spin polarization of the

surface states at $\omega = -0.5$ with $\lambda_{\text{intra}} = 0.1$, c.f. Fig. 4.4(b). For nonzero λ_{inter} , a qualitatively identical situation is found. In the next chapter, we will show how their spin structure can be measured.

4.5 Spin-resolved quasiparticle interference

To resolve the spin polarization of the surface states, we will look at spin-resolved patterns arising from scattering at a magnetic impurity. Spin-resolved STM measurements can be done using a magnetic or spin-polarized tip [103, 104].

Formally, we introduce in Eq. (4.4.3) the operator $S^\mu = \frac{1}{2}\tau_0 \otimes \sigma_\mu$, $\nu \in \{0, x, y, z\}$, acting on the spin degrees of freedom to the instrument response function $\hat{F}^\mu = \hat{F}S^\mu$. In the same manner, the impurity magnetic moment is encoded via $\hat{V}^\nu = \hat{V}S^\nu$. The QPI patterns $\rho^{\mu\nu}$ can then be evaluated for all combinations of tip and spin polarization, shown in Fig. 4.8. Exchanging the spin indices μ and ν changes the magnetization of the STM tip with the impurity, which differ only in their spatial dependence within the sample. Since both are sensitive to the first few layers only, the resulting patterns are qualitatively symmetric under this exchange. The component ρ^{00} corresponds to the case discussed in the previous section. In the spin degenerate case for vanishing SOC, all nonzero components can be summarized as $\rho^{\mu\nu} = \delta^{\mu\nu}\rho^{00}$.

We focus on the case $\lambda_{\text{inter}} = 0.2$, $\lambda_{\text{intra}} = 0$, where the bulk states remain spin degenerate and only the drumhead surface states are spin polarized. In this chapter, we remove the apparent particle-hole symmetry by using parameters in the Hamiltonian, that qualitatively resemble the nodal-line material CaAgAs, see Fig. 4.7. As mentioned before, the dominant contributions to the QPI pattern arise from \mathbf{q} connecting the two surface states and ρ^{00} remains qualitatively unchanged even for non-zero SOC. In ρ^{33} , the matrices S^z each flip the spins in the xy -plane, and the dominant contributions arise for nesting vectors \mathbf{q} connecting opposite spins. Each surface state contributes one ring with twice the radius of the state where it intersects ω , leading to two concentric rings in the QPI pattern. ρ^{11} and ρ^{22} present a mixed case.

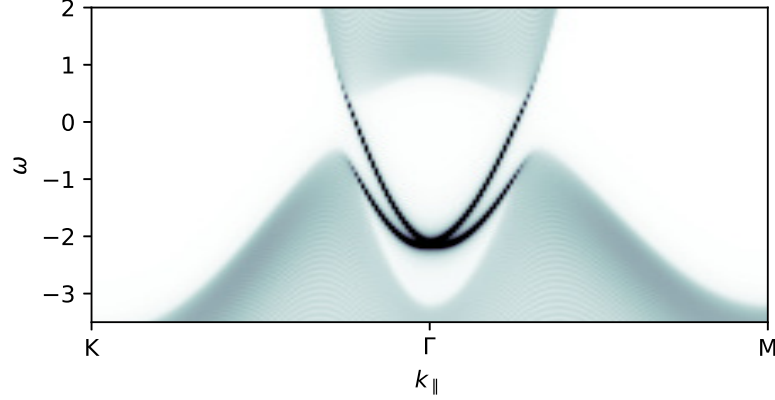


Figure 4.7: Surface density of states for the gapped NLSM model with parameters $\mu = 4.3$, $\delta\mu = -10.5$, $t_{\parallel} = -0.75$, $\delta t_{\parallel} = 1.25$, $t'_{\perp} = -0.5$, $\delta t'_{\perp} = 2.5$, $t_{\perp} = 2.5$ and $\lambda_{\text{inter}} = 0.2$. While the bulk remains spin degenerate, the drumhead surface states are spin polarized and close the bulk gap, which was opened by hybridizing the spin subspaces due to nonzero SOC.

The spins are flipped in the \mathbf{q}_y and \mathbf{q}_x direction, respectively, because of the Rashba-like spin polarization $k_y\sigma_x + k_x\sigma_y$. In this direction, there are again two separate peaks in the signal. In the perpendicular direction, the spin matrices contribute only the eigenvalue squared and the QPI pattern remains unchanged in this direction with respect to ρ^{00} .

For the off-diagonal entries, we find $\rho^{0i} = \rho^{i0} = 0$ for all $i = x, y, z$. The remaining entries have contributions from the spin polarized surface states only and S^x and S^y each contribute the sign of their eigenvalue in the q_y and q_x direction, respectively. This leads to antisymmetric patterns ρ^{13} and ρ^{23} with respect to a reflection of q_y or q_x , respectively, and for both components in ρ^{12}

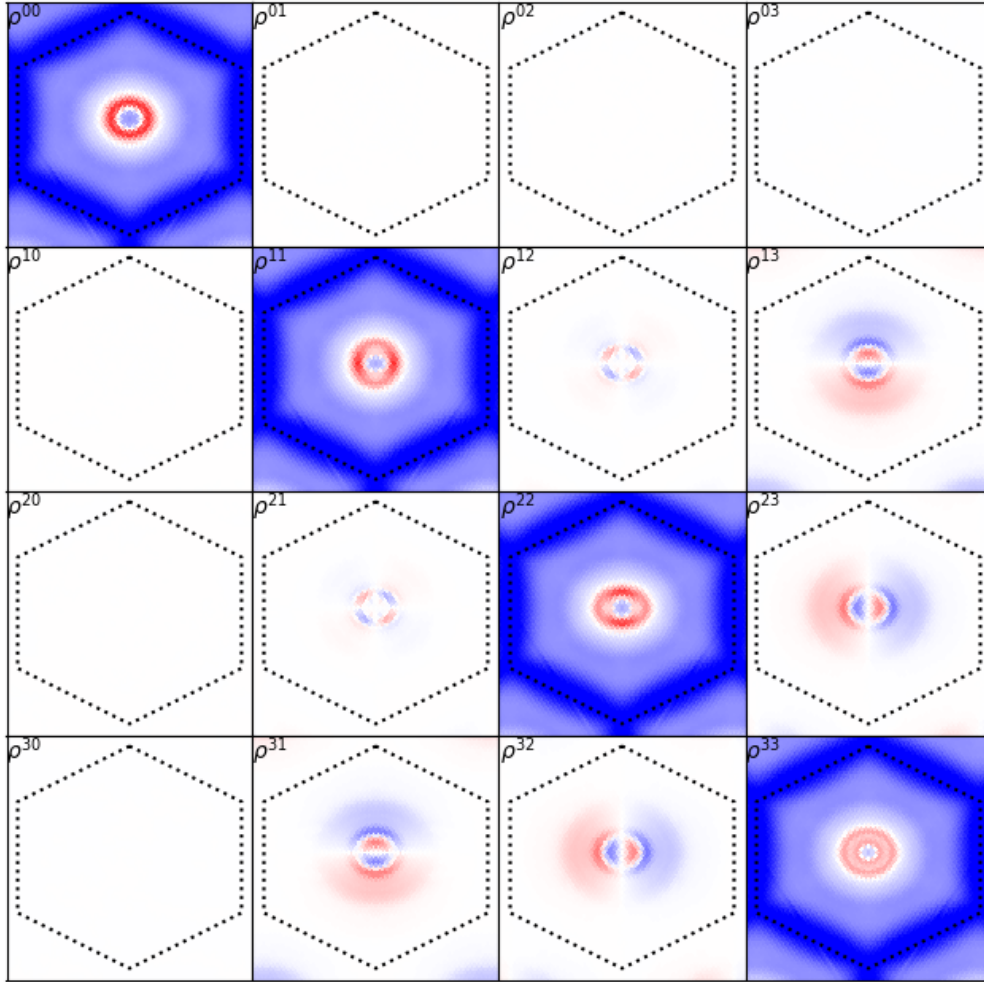


Figure 4.8: Spin-resolved QPI patterns $\rho^{\mu\nu}$ with spin component $\nu = 0, x, y, z$ and magnetic impurity with spin $\mu = 0, x, y, z$ for inter-orbital SOC contributions with a bias voltage of $\omega_- = 2.0$. The parameters of the Hamiltonian are identical to the one listed in Fig. 4.7

4.6 Summary

In this chapter, we took a closer look at the surface states of a nodal-loop semimetal. It is shown, that a non-vanishing Berry phase does not guarantee topological surface states, but there are drumhead surface states for this type of NLSM. With nonzero SOC, the nodal line becomes gapped and the system is turned into a mirror Chern insulator with chiral surface states in accordance to the drumhead surface states of the spinless loop. Drumhead surface states are often elusive, but have been measured in several NLSMs [105, 106] and also synthetic materials [107]. They are however often difficult to detect directly via angle-resolved photo emission spectroscopy. We calculated the signature of these surface states in QPI patterns, which provides a method to identify them indirectly, taking advantage of their high surface weight. Recently, this approach has been experimentally verified in a NLSM with double loops [108].

In the presence of inversion symmetry, the bulk is spin-degenerate and the surface states contribute in a unique way to spin-resolved QPI measurements. Taking all possible combinations of tip and impurity polarization into account, the spin structure of the drumhead surface states can be reconstructed from the QPI patterns.

5. Anomalous Hall effect in nodal line system

A nodal line with a non-zero Berry phase can be understood as a singularity with diverging Berry curvature. The Berry curvature is directly related to an anomalous component in the electric DC conductivity. However, the direction of the Berry curvature is only well defined for a gapped nodal line. Often times, the contributions from different sites of a nodal line gapped by a small symmetry breaking perturbation will cancel exactly. In this chapter, we will investigate the effect of periodic driving with circularly polarized light on the NLSM, which breaks the spatial symmetries and time-reversal symmetry such, that a nonzero anomalous conductivity can be observed.

5.1 Model Hamiltonian

Similar to the previous chapter, we use a two-band model to describe the nodal-loop semimetal. It is again induced from two sites half a unit cell apart, c.f., Fig. 4.1(a). In this chapter, we define the NLSM on a tetragonal lattice with up to second-nearest neighbor hopping. The coefficients of $H(\mathbf{k}) =$

$\bar{\varepsilon}(\mathbf{k})\tau_0 + \mathbf{d}(\mathbf{k}) \cdot \boldsymbol{\tau}$ read

$$\bar{\varepsilon} = -\frac{\bar{v}_r}{\sin k_F}(\cos k_x + \cos k_y) - 2\bar{w} \cos k_z + \mu, \quad (5.1.1a)$$

$$d_z = -\frac{\delta v_r}{\sin k_F}(\cos k_x + \cos k_y) - 2\delta w \cos k_z + \delta\mu, \quad (5.1.1b)$$

$$d_y = 2v_z \sin\left(\frac{k_z}{2}\right), \quad (5.1.1c)$$

$$d_x = 0. \quad (5.1.1d)$$

Here, we implicitly set the unit cell lengths $a = c = 1$. In the following, we will also set $e = \hbar = 1$, such that all quantities are expressed in units of the hopping.

The difference in on-site energy is set to $\delta\mu = \delta v_r \frac{1+\cos k_F}{\sin k_F} + 2\delta w$. With this, the nodal line in the $k_z = 0$ plane is at the Fermi energy and is parametrized via

$$\cos k_x = 1 + \cos k_F - \cos k_y, \quad (5.1.2)$$

with radius k_F at the intersections with the k_x - and k_y -axis. The group velocities $\frac{\partial E(\mathbf{k})}{\partial k_i}$ of the dispersion at these points is given by $v_r^\pm = \bar{v}_r \pm \delta v_r$ along the k_x - and k_y -axis and $\pm v_z$ in the k_z -direction. For small radii $k_F \approx \sin k_F$, the nodal line becomes approximately round and a low-energy model can be obtained by expanding around Γ up to second order in momentum. The coefficients of the low-energy Hamiltonian are

$$\bar{\varepsilon} = \frac{\bar{v}}{2k_F} (k_x^2 + k_y^2 - k_F^2) + \bar{w}_i k_z^2 + \mu, \quad (5.1.3a)$$

$$d_z = \frac{\delta v}{2k_F} (k_x^2 + k_y^2 - k_F^2) + \delta w_i k_z^2, \quad (5.1.3b)$$

$$d_y = v_z k_z, \quad (5.1.3c)$$

$$d_x = 0. \quad (5.1.3d)$$

5.2 Berry curvature and anomalous velocity

As discussed in Sec. 4.2, the nodal line is topologically characterized by the Berry phase evaluated on line integrals along closed paths. Such a loop integral picks up a phase of π if it winds around the nodal line an odd number of times, while the integral for a path that can be contracted to a single point without encountering a degenerate point vanishes identically. Stokes' theorem then implies that the Berry curvature $\mathcal{F} = d\mathcal{A}$ is divergent along the nodal line and zero elsewhere. Introducing a small symmetry-breaking constant term $d_x = m$ turns the nodal line into an avoided crossing and the Berry curvature becomes non-zero and well-defined everywhere in the Brillouin zone.

$$\begin{pmatrix} \mathcal{F}_{yz} \\ \mathcal{F}_{zx} \\ \mathcal{F}_{xy} \end{pmatrix} = \frac{mv_z \delta v_r}{2|\mathbf{d}|^3} \cos\left(\frac{k_z}{2}\right) \begin{pmatrix} -\sin k_y \\ +\sin k_x \\ 0 \end{pmatrix}. \quad (5.2.1)$$

From the low-energy model it becomes obvious that the Berry curvature is tangential to the nodal line, $\mathcal{F} = \frac{mv_z \delta v_r}{2|\mathbf{d}|^3} \frac{k_r}{k_F} \hat{\mathbf{e}}_\phi$. In Fig. 5.2(a) we illustrate the major contribution to the Berry curvature field for non-zero m . In the limit $m \rightarrow 0$, the above expression becomes a Dirac delta function, i.e., the Berry curvature vanishes identically everywhere except for the nodal line, where it diverges. The sign of the Berry curvature depends however directly on the sign of the perturbation m and the limit is not well defined.

At zero temperature and in the clean limit, the off-diagonal terms in the DC conductivity tensor in linear response theory are directly related to the integral over the Berry curvature of all bands weighted by the Fermi factor [109],

$$\sigma_{ij}^{\text{DC}} = \frac{e^2}{(2\pi)^3} \sum_{\alpha=\pm} \int_{\text{BZ}} d^3k f(\varepsilon_{\mathbf{k}}^\alpha) \mathcal{F}_{ij}^\alpha, \quad (5.2.2)$$

and consequently the Berry curvature gives rise to the intrinsic anomalous Hall effect. Here we labeled the upper and lower bands by \pm and used the

fact that their Berry curvature adds up to zero at each \mathbf{k} , i.e., $\mathcal{F}^\pm = \pm\mathcal{F}$. In the nodal-loop system with a constant symmetry breaking term, however, the Berry curvature is anti-symmetric in the radial component and contributions from opposite sides cancel exactly in the integral over the Brillouin zone, such that no net Hall current can be observed [110]. A slice in k -space in a plane horizontal to the reflection plane, i.e. the plane of the nodal line, gives a 2D system with two nodal points of opposite chirality. From a topological point of view, such a subsystem resembles graphene with its two Dirac points at K and $K' = -K$, leading to opposing valley currents [111, 112]. It can be shown that circularly polarized light with vertical indication couples only to the node with the same chirality, while transitions at the node of opposite chirality are strongly suppressed [113]. This strongly suggest that in a NLSM subjected to polarized light an anomalous Hall current can be measured.

5.3 Periodic driving

We introduce periodic driving by circularly polarized, monochromatic light incident in the plane of the nodal line. By neglecting the magnetic components of the light field and by assuming spatial homogeneity, we can describe the circularly polarized light by

$$\tilde{\mathbf{A}}(t) = -A_x \cos(\Omega t)\mathbf{e}_x - A_z \sin(\Omega t)\mathbf{e}_z, \quad (5.3.1)$$

which corresponds to the temporal gauge preserving translation invariance. The cases $A_x = \frac{E_x}{\Omega} = \mp \frac{E_z}{\Omega} = \mp A_z$ corresponds to fully right or left polarized light. Introducing the field via Peierls substitution and Fourier transforming to k -space results in the time-dependent Hamiltonian $H(\mathbf{k}, t) = H(\mathbf{k} - \tilde{\mathbf{A}}(t))$.

5.3.1 Floquet formalism

The Hamiltonian inherits discrete time-translation symmetry $H(t + T) = H(t)$ from the periodicity of $\tilde{\mathbf{A}}(t)$ with driving period $T = \frac{2\pi}{\Omega}$. Therefore, the Hamiltonian commutes with the discrete time-translation opera-

tors $U(t_0, t_0 + nT)$, $n \in \mathbb{Z}$. These operators form an Abelian group and have therefore one-dimensional irreducible representations. As shown in the group theoretic proof for the Bloch theorem in Sec. 2.1.1, this allows us to write eigenstates of the time dependent Schrödinger operator, $(H(t) - i\frac{d}{dt})|\psi\rangle = 0$, as a product of a time periodic Floquet state and a phase factor [114],

$$|\psi_\alpha(t)\rangle = e^{-i\varepsilon_\alpha t} |u_\alpha(t)\rangle. \quad (5.3.2)$$

The quasienergies ε_α can be chosen from the interval $[-\frac{\Omega}{2}, \frac{\Omega}{2}) = [-\frac{\pi}{T}, \frac{\pi}{T})$, because two quasienergies which differ by a multiple of Ω result in the same time translation eigenvalue. In analogy to the BZ in k -space, this interval is also referred to as the first Floquet Brillouin zone (FBZ). The Hamiltonian and the periodic states can be written in terms of a discrete Fourier series with coefficients

$$H_n = \frac{1}{T} \int_0^T dt e^{in\Omega t} H(\mathbf{k}, t). \quad (5.3.3)$$

$$|u_\alpha^n\rangle = \frac{1}{T} \int_0^T dt e^{in\Omega t} |u_\alpha(t)\rangle, \quad (5.3.4)$$

The states $|u_\alpha^n\rangle$ form a basis of the so-called Sambe space [114] of time-periodic integrable functions. This extends the original Hilbert space by the time coordinate $\mathbb{T} = [0, T)$ as an internal parameter. The inner product of this Hilbert space implicitly contains an integral over one period. Throughout this chapter, we will use indices m, n for discrete Fourier components and α, β to label the Floquet quasienergies and their eigenstates. Using these definitions, the Schrödinger equation can be expressed as time-independent eigenvalue problem

$$\sum_{n=-\infty}^{\infty} Q_{mn} |u_\alpha^n\rangle = \varepsilon_\alpha |u_\alpha^m\rangle, \quad (5.3.5)$$

of the Fourier transformed Floquet operator

$$Q_{mn} = H_{m-n} - n\Omega\delta_{mn}. \quad (5.3.6)$$

This equation has infinitely many solutions corresponding to physically equivalent states whose eigenvalues differ by integer multiples of Ω . They are related by a shift in the Fourier index,

$$Q_{mn} |u_\alpha^{n+l}\rangle = (\varepsilon_\alpha + l\Omega) |u_\alpha^{m+l}\rangle. \quad (5.3.7)$$

Starting with the low-energy Hamiltonian, we can evaluate the three non-vanishing components of the Fourier transformed Hamiltonian directly. The time-averaged component H_0 is identical to the undriven Hamiltonian up to the redefinition of some of its constants, c.f., Eq. (5.1.3),

$$k_F \rightarrow \tilde{k}_F^2 = k_F^2 - \frac{1}{2}A_x^2 - \frac{\delta w k_F}{\delta v_r} A_z^2, \quad (5.3.8)$$

$$\bar{v}_r \rightarrow \tilde{v}_r = \bar{v}_r \frac{\tilde{k}_F}{k_F}, \quad (5.3.9)$$

$$\delta v_r \rightarrow \delta \tilde{v}_r = \delta v_r \frac{\tilde{k}_F}{k_F}, \quad (5.3.10)$$

$$\mu \rightarrow \tilde{\mu} = \mu + \frac{1}{2}A_z^2(\bar{w} - \frac{\bar{v}_r}{\delta v_r} \delta w). \quad (5.3.11)$$

The two non-zero off-diagonal components are

$$\begin{aligned} H_{\pm 1}(\mathbf{k}) = & \left(\frac{v_r}{2k_F} A_x k_x \pm i w A_z k_z \right) \tau_0 \\ & + \left(\frac{\delta v_r}{2k_F} A_x k_x \pm i \delta w A_z k_z \right) \tau_z \\ & \mp i v_z A_z \tau_y, \end{aligned} \quad (5.3.12)$$

$$H_{\pm 2}(\mathbf{k}) = \frac{A_x^2}{8k_F} (\bar{v}_r \tau_0 + \delta v_r \tau_z) - \frac{A_z^2}{4} (\bar{w} \tau_0 + \delta w \tau_z). \quad (5.3.13)$$

For tight-binding lattice Hamiltonians, the entries of Q_{mn} can also be written out analytically. Using the identities for Bessel functions of the first

kind $J_n(x)$,

$$\begin{aligned} \frac{1}{T} \int_0^T dt e^{in\Omega t} e^{iA_i \cos \Omega t} &= i^n J_n(A_i), \\ \frac{1}{T} \int_0^T dt e^{in\Omega t} e^{iA_i \sin \Omega t} &= (-1)^n J_n(A_i), \end{aligned} \quad (5.3.14)$$

and considering that they are even (odd) in their argument for even (odd) n , we can put together a table for the entries of the Fourier transformed Hamiltonian H_n based on the sine and cosine terms in the lattice Hamiltonian,

	n even	n odd	
$\cos(k_i + A_i \cos(\Omega t))$	$i^n \cos(k_i)$	$i^{n+1} \sin(k_i)$	$\left. \vphantom{\begin{matrix} \cos(k_i + A_i \cos(\Omega t)) \\ \sin(k_i + A_i \cos(\Omega t)) \\ \cos(k_i + A_i \sin(\Omega t)) \\ \sin(k_i + A_i \sin(\Omega t)) \end{matrix}} \right\} \times J_n(A_i). \quad (5.3.15)$
$\sin(k_i + A_i \cos(\Omega t))$	$i^n \sin(k_i)$	$-i^{n+1} \cos(k_i)$	
$\cos(k_i + A_i \sin(\Omega t))$	$\cos(k_i)$	$-i \sin(k_i)$	
$\sin(k_i + A_i \sin(\Omega t))$	$\sin(k_i)$	$i \cos(k_i)$	

Strictly speaking, the off-diagonal entries in $Q_{(m+n)m}$ are non-zero for all orders of n . Those are however proportional to the n -th Bessel function of the first kind, $(H_n)_{ij} \propto J_n(A)$ and higher orders are suppressed exponentially in n . The zeroth component H_0 is again similar to the unperturbed Hamiltonian with some of its constants renormalized by the driving. The operator Q_{mn} is therefore local in the indices m and n and the eigenstates and quasienergies can again be calculated from a truncated version.

In dealing with a truncated matrix with a symmetric range of indices from $n = -N_m$ to $n = N_m$, the states with the highest weight on the central component $n = 0$, $w_\alpha = ||w_\alpha^0\rangle|$ are least sensitive to finite size effects. The dispersion of the quasienergies ε_α for the lattice model are shown in Fig. 5.1 and the band thickness indicates the weight w_α . For weak light intensity, the quasienergy dispersion close to the Fermi energy reproduces the original band structure. However, the mirror symmetry is broken by the driving and the nodal line is gapped almost everywhere.

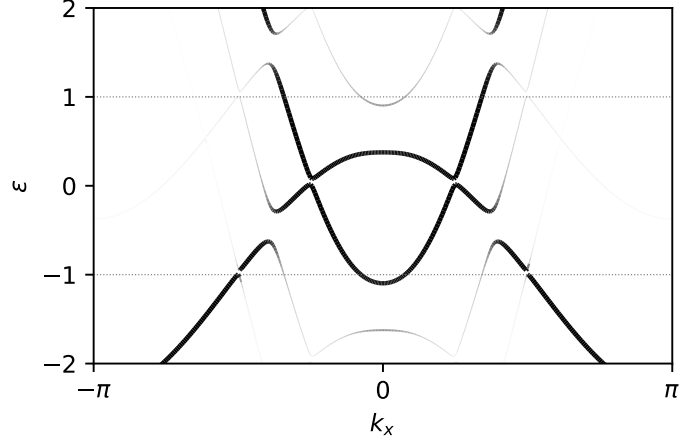


Figure 5.1: Floquet quasienergy band structure of the driven NLSM defined in Eq. (5.1.1) projected onto the $n = 0$ component. Parameters throughout the text are $v_r = -1$, $\delta v_r = 2$, $v_z = 4$ and $k_F = \frac{\pi}{4}$ for the Hamiltonian. The driving intensity and frequency are $E_z = -E_x = 0.2$ and $\Omega = 2.0$. Horizontal dashed lines mark the FBZ boundaries at $\varepsilon = \pm \frac{\Omega}{2}$.

5.3.2 Effective Hamiltonian

In order to see the effect of the periodic driving on the nodal line more clearly, we introduce an effective Hamiltonian. For this purpose, we treat the off-diagonal blocks $H_{\pm 1}$ as a perturbation to H_0 . This is justified, when the driving frequency is large compared to the energy scale of H_0 , which is satisfied for the bands in proximity of the nodal line. In this energy range, the low-energy Hamiltonian provides an accurate description of the bands. Using $\varepsilon_{\pm 1, \alpha} - \varepsilon_{0, \beta} \approx \pm \Omega$, the effective Hamiltonian reads



Figure 5.2: Berry curvature for a nodal loop gapped by small symmetry breaking term d_x . The Berry curvature is evaluated for a discrete set of angles in cylindrical coordinates, the arrow length and intensity indicates the strength. (a) The Berry curvature flows uniformly along the former loop in a circle for a constant symmetry breaking term. (b) Two ungapped points remain, acting as source and sink of Berry curvature, which flows in the same direction on both sides of the loop.

$$\begin{aligned}
 H_{\text{eff}} &= H_0 + \frac{1}{\Omega} [H_{-1}, H_1] & (5.3.16) \\
 &= \left(\frac{\tilde{v}}{2\tilde{k}_F} \left(k_x^2 + k_y^2 - \tilde{k}_F^2 \right) + \bar{w}_i k_z^2 + \tilde{\mu} \right) \tau_0 \\
 &\quad + \left(\frac{\delta\tilde{v}}{2\tilde{k}_F} \left(k_x^2 + k_y^2 - \tilde{k}_F^2 \right) + \delta w_i k_z^2 \right) \tau_z \\
 &\quad + v_z k_z \tau_y \\
 &\quad + \frac{\delta v_r v_z}{k_F} \frac{A_x A_z}{\Omega} k_x \tau_x. & (5.3.17)
 \end{aligned}$$

The new term in the last line gaps the nodal line everywhere except for $\mathbf{k}_{\pm} = \pm \tilde{k}_F \hat{\mathbf{e}}_y$. At these two points we find Weyl points [115]. Expanding to lowest order in $\mathbf{q} = \mathbf{k} \pm k_f \hat{\mathbf{e}}_y$ shows, that they have indeed linear dispersion,

$$H_{\pm}(\mathbf{q}) = \pm \tilde{v}_r q_y \tau_0 \pm \delta \tilde{v}_r q_y \tau_z + v_z q_z \tau_y + \frac{\delta v_r v_z}{k_F} \frac{A_x A_z}{\Omega} q_x \tau_x, \quad (5.3.18)$$

and therefore topological charges of $\mathcal{C}_{\pm} = \pm \text{sgn}(A_x A_z)$, c.f. Sec. 3.1. Note that the coefficients δv_r and v_z appear implicitly twice, therefore the Chern number is independent of their sign. This is relevant when taking the spin degrees of freedom into account, because for the \mathcal{PT} -symmetric copy in a

spin-degenerate band structure, these coefficients have an additional minus sign. With the uniform contribution $\tilde{v}_r q_y \tau_0$ the Weyl cones are tilted and turn into type-II Weyl points for $\tilde{v}_r > \delta \tilde{v}_r$ [116]. In the following discussion, we will restrict ourselves to type-I Weyl points only. The flow of Berry curvature still follows the nodal line, but in contrast to the constant symmetry breaking term discussed in Sec. 5.2, one Weyl point acts as source and the flow points to the other Weyl point along both parts of the circle, shown in Fig. 5.2(b). Therefore, their contributions to the anomalous Hall conductivity add up. The direction of the flow can be reversed by changing the sign of either A_x or A_z , which physically means switching the light polarization. If the Fermi energy is exactly at the Weyl nodes, the contribution to the anomalous Hall effect at zero temperature depends only on the distance of the two Weyl points [117] in the clean limit,

$$\begin{aligned}
 \sigma_{xz}^{\text{DC}} &= \frac{e^2}{(2\pi)^3} \int_{\text{BZ}} d^3k \mathcal{F}_{xz} \\
 &= \frac{e^2}{2\pi} \int_{-\pi}^{\pi} dk_x \mathcal{C}(k_x) \\
 &= \frac{e^2}{2\pi} 2\tilde{k}_F.
 \end{aligned} \tag{5.3.19}$$

The last line follows from the observation, that the integral of \mathcal{F}_{xz} over a slice of the BZ for constant k_x is the Chern number of the two-dimensional subsystem. For $\tilde{k}_F < k_x < \tilde{k}_F$, i.e., between the two Weyl nodes, the Chern number is ± 1 and 0 otherwise. This results also holds for small variations of the Fermi energy with respect to the Weyl nodes, as long as there are two disconnected Fermi surfaces surrounding each Weyl point [118, 119]. However, due to the small gap of the order $|E|^2$, we expect the anomalous Hall effect to be smaller, because the bands will not be fully occupied or unoccupied close to the nodal line, where the Berry curvature is strongest.

5.3.3 Keldysh formalism for the quasistatic system

We calculate the current or conductivity for a steady state solution of the driven system coupled to a heat bath. The heat bath is either provided by

leads in a finite-sized system or by some averaged disorder coupling to unspecified degrees of freedom. In this section, we will introduce the formalism in an abstract manner. We follow the derivation in Ref. [120], which provides a direct derivation equivalent to the Keldysh formalism. The Hamiltonian of the whole setup consists of three parts, the nodal line, the bath and the coupling between the two, $H = H_{\text{NL}} + H_{\text{bath}} + H_{\text{coupl}}$. For a general derivation we introduce a superindex I, J combining orbital degrees of freedom as well as momentum or spatial indices and use the Einstein convention of summing repeated indices. The nodal-loop Hamiltonian in second quantization reads,

$$H_{\text{NL}} = H_{IJ}(t)c_I^\dagger c_J. \quad (5.3.20)$$

We further define a heat bath in the wide band limit, i.e., with a continuous, uniform density of states across the whole relevant energy range. Each degree of freedom I is individually coupled to the bath with coupling strength V_I independent of energy,

$$H_{\text{leads}} = \int d\varepsilon \varepsilon d_{I,\varepsilon}^\dagger d_{I,\varepsilon}, \quad (5.3.21)$$

$$H_{\text{coupl}} = \int d\varepsilon V_I \left(d_{I,\varepsilon}^\dagger c_I + d_{I,\varepsilon} c_I^\dagger \right). \quad (5.3.22)$$

With these assumption, the bath is memory free and does not introduce correlations in time or across degrees of freedom. Furthermore, we assume the bath is not affected by the system's dynamics and therefore completely characterized by temperature and chemical potential. The Heisenberg equations of motion for the annihilation operators are

$$i \frac{d}{dt} d_{I,\varepsilon}(t) = V_I c_I(t) + \varepsilon d_{I,\varepsilon}(t), \quad (5.3.23)$$

$$i \frac{d}{dt} c_I(t) = H_{IJ}(t) c_J(t) + \int d\varepsilon V_I d_{I,\varepsilon}(t). \quad (5.3.24)$$

Integrating the former equation and inserting it in the latter results in the integro-differential equation for the nodal line operators,

$$\begin{aligned} i\frac{dc_I(t)}{dt} &= H_{IJ}c_J(t) - i \int d\varepsilon V_I \left(\int_0^{t-t_0} d\tau V_I e^{i\varepsilon\tau} c_I(t-\tau) + ie^{-i\varepsilon(t-t_0)} d_{I,\varepsilon}(t_0) \right) \\ &= (H_{IJ}(t) - \Sigma_{IJ}^R) c_J(t) + \int d\varepsilon V_I e^{-i\varepsilon(t-t_0)} d_{I,\varepsilon}(t_0). \end{aligned} \quad (5.3.25)$$

In the last line, we introduced the notation

$$\Sigma_{IJ}^R = \frac{i}{2} \delta_{IJ} V_I^2. \quad (5.3.26)$$

By choosing the coupling to be energy independent, the first term in the bracket is local in time, $\int d\varepsilon e^{i\varepsilon\tau} = \delta(\tau)$. Therefore, the equation reduces to an inhomogeneous differential equation. We can compactly define the Greens function to this differential operator,

$$\left(i\frac{d}{dt} - H_{NL}(t) + \Sigma^R \right) G(t, t') = \delta(t - t'). \quad (5.3.27)$$

Sending $t_0 \rightarrow -\infty$, the equation of motion for the annihilation operators of the nodal line system can be written in terms of the retarded Greens function

$$c_I(t) = \int_0^\infty d\tau G_{IJ}(t, t-\tau) \int d\varepsilon V_J e^{-i\varepsilon(t-\tau)} d_{I,\varepsilon} \quad (5.3.28)$$

$$= \int d\varepsilon G_{IJ}^R(t, \varepsilon) V_J e^{-i\varepsilon t} d_{J,\varepsilon}. \quad (5.3.29)$$

The solution for the creation operators follows from taking the Hermitian conjugate. Defining the advanced Greens function $G^A(t, \varepsilon) = G^R(t, \varepsilon)^\dagger$ and advanced self-energy $\Sigma^A = \Sigma^{R\dagger} = -\Sigma^R$, we can also write an expression formally equivalent to Eq. (5.3.27) for the advanced Greens function. Finally, we can then evaluate the full propagator,

$$\begin{aligned} -iG_{IJ}^<(t, t') &= \left\langle c_I^\dagger(t') c_J(t) \right\rangle \\ &= \int d\varepsilon \int d\varepsilon' G_{JK}^R(t, \varepsilon) V_K e^{i\varepsilon t} \left\langle d_{L,\varepsilon'}^\dagger d_{K,\varepsilon} \right\rangle e^{-i\varepsilon' t'} V_L G_{LI}^A(t', \varepsilon'). \end{aligned} \quad (5.3.30)$$

The correlation function of the heat bath is diagonal in both indices and contains otherwise only the Fermi distribution function,

$$\left\langle d_{L,\varepsilon}^\dagger d_{K,\varepsilon} \right\rangle = \delta_{KL} \delta(\varepsilon - \varepsilon') f_L(\varepsilon). \quad (5.3.31)$$

With the definition

$$\Sigma_{KL}^<(\varepsilon) = i\delta_{KL} V_L^2 f_L(\varepsilon), \quad (5.3.32)$$

we can express Eq. (5.3.30) compactly as a matrix equation,

$$G^<(t, t') = \int d\varepsilon G^R(t, \varepsilon) \Sigma^<(\varepsilon) e^{i\varepsilon(t-t')} G^A(t', \varepsilon). \quad (5.3.33)$$

This result can alternatively be obtained from solving the equation

$$\begin{pmatrix} G^R & G^K \\ 0 & G^A \end{pmatrix}^{-1} = \begin{pmatrix} \varepsilon+0^+ - H_{\text{NL}} & 0 \\ 0 & \varepsilon+0^- - H_{\text{NL}} \end{pmatrix} + \begin{pmatrix} \Sigma^R & \Sigma^K \\ 0 & \Sigma^A \end{pmatrix} \quad (5.3.34)$$

in the Keldysh formalism [121], where the Keldysh component of the self-energy is $\Sigma_{IJ}^K(\varepsilon) = i\delta_{IJ}(1 - 2f_I(\varepsilon))$. The upper triangular structure of this block matrix allows to read off the entries of the inverse matrix directly. The retarded and advanced Greens functions are just the inverse of the diagonal entries in agreement with the definition in Eq. (5.3.27), and the Keldysh Greens function is $G^K = -G^R \Sigma^K G^A$. The lesser Greens function follows from the identity $G^< = \frac{1}{2}(G^K + G^R - G^A) = G^R(-\Sigma^K + \Sigma^R - \Sigma^A)G^A$ [122], reproducing Eq. (5.3.33) through the relation $\Sigma^< = \frac{1}{2}(\Sigma^R - \Sigma^A - \Sigma^K)$ [123].

Because $\Sigma^{R/A}$ are time-independent, the retarded and advanced Greens functions $G^{R/A}(t, \varepsilon)$ are periodic in the remaining time component. They can therefore be expressed in eigenstates and eigenvalues of the Floquet operators extended by the self-energy,

$$(H_{m-n} - \Sigma^R \delta_{mn} - n\Omega \delta_{mn}) |u_\alpha^n\rangle = \varepsilon_\alpha |u_\alpha^m\rangle, \quad (5.3.35a)$$

$$(H_{m-n} - \Sigma^A \delta_{mn} - n\Omega \delta_{mn}) |v_\alpha^n\rangle = \varepsilon_\alpha^* |v_\alpha^m\rangle. \quad (5.3.35b)$$

Since Σ^R and Σ^A are not Hermitian, the eigenvalues are complex valued. The complex conjugated and transposed eigenvectors $\langle u_\alpha^n |$ and $\langle v_\alpha^n |$ also serve as left eigenvalues to the other, i.e., complex conjugate, operator. Together they form a bi-orthonormal basis, $\sum_n \langle u_\alpha^n | v_\beta^n \rangle = \delta_{\alpha\beta}$. In this basis, the retarded and advanced Greens functions can be given explicitly as a matrix in Fourier indices,

$$\begin{aligned} G_n^R(\varepsilon) &= \frac{1}{T} \int_0^T dt e^{in\Omega t} G^R(t, \varepsilon) \\ &= \sum_{\alpha, m} \frac{|u_\alpha^{m+n}\rangle \langle v_\alpha^m|}{\varepsilon - \varepsilon_\alpha - m\Omega}, \end{aligned} \quad (5.3.36)$$

$$\begin{aligned} G_n^A(\varepsilon) &= \frac{1}{T} \int_0^T dt e^{in\Omega t} G^A(t, \varepsilon) \\ &= \sum_{\alpha, m} \frac{|v_\alpha^m\rangle \langle u_\alpha^{m-n}|}{\varepsilon - \varepsilon_\alpha^* - m\Omega}. \end{aligned} \quad (5.3.37)$$

All eigenvalues ε_α are shifted up from the real axis, because all entries in Σ^R have positive imaginary part, and vice versa for the complex conjugate eigenvalues. Therefore, no infinitesimal shift from the real axis is needed. Here, the sum over α includes only Floquet quasienergies from the first FBZ and the sum over the Fourier index m accounts for the other solutions of Eqs. (5.3.35a) and (5.3.35b) explicitly.

5.4 Current in a finite sample

In this chapter, we follow the approach in Ref. [18] and calculate the anomalous Hall current in the Landauer–Büttiker formalism [124]. In this approach, we describe a finite-sized sample with N layers and open boundary conditions in the x -direction. The remaining directions are treated in periodic boundary conditions. At the left and right boundaries we introduce leads, which keep the translational invariance in the remaining directions. Therefore, $k = (k_z, k_y)$ remain good quantum numbers. In Fig. 5.3 we illustrate the setup. In this geometry, there are no surface states, as the nodal line in the $k_z = 0$ plane is projected to a line in the real space description. The

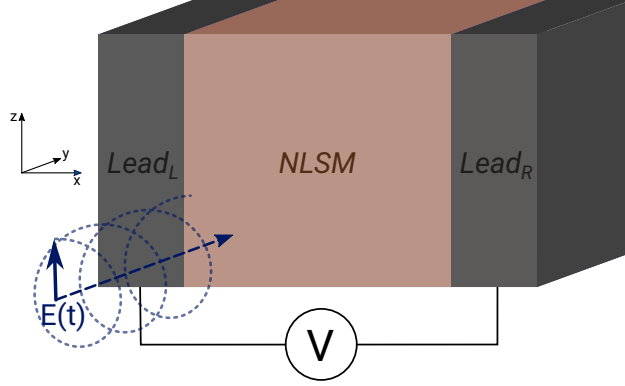


Figure 5.3: Schematic setup of the driven NLSM between two leads. The boundary conditions in y and z direction are treated as periodic.

applied voltage across the sample is modeled by the difference in chemical potential between the left and right lead.

The partially real space version of the nodal line Hamiltonian introduced in Eq. (5.1.1) is

$$\begin{aligned}
 H_{\text{NL}}(k, t) = & \sum_{r,s} \sum_{i=1}^N M_{rs}(k_y, k_z + A_z \sin(\Omega t)) c_{k,i,r}^\dagger c_{k,i,s} \\
 & + \sum_r \sum_{i=1}^{N-1} \frac{t_r}{2} (e^{+iA_x \cos(\Omega t)} c_{k,i,r}^\dagger c_{k,i+1,r} + \text{h.c.}).
 \end{aligned} \tag{5.4.1}$$

Here and in the following, indices r, s label the two sites per unit cell and indices i, j label cells. In x -direction there is only nearest-neighbor hopping with strength $t_r = \frac{\bar{v}_r \pm \delta v}{\sin k_F}$, c.f. Fig. 4.1(a). The intra-unit cell component $M = \varepsilon \sigma_0 + \mathbf{m} \cdot \boldsymbol{\sigma}$ contains the k -dispersion and on-site potentials,

$$\bar{\varepsilon} = -\frac{\bar{v}_r}{\sin k_F} \cos k_y - 2\bar{w} \cos k_z + \mu, \tag{5.4.2a}$$

$$m_z = -\frac{\delta v_r}{\sin k_F} \cos k_y - 2\delta w \cos k_z + \delta \mu, \tag{5.4.2b}$$

$$m_y = 2v_z \sin\left(\frac{k_z}{2}\right), \tag{5.4.2c}$$

$$m_x = 0. \tag{5.4.2d}$$

The entries in the Floquet operator of this Hamiltonian again contain the

Bessel functions of the first kind and can readily be identified using the identities given in Eq. (5.3.14) and Eq. (5.3.15). Both sites in the first and last unit cells are coupled uniformly to the leads with coupling strength $\sqrt{\Gamma}$. In this case, the self-energy terms defined in Eqs. (5.3.26) and (5.3.32) read

$$\Sigma_{k,ij,rs}^{\text{R/A}} = \pm i \frac{\Gamma}{2} \delta_{ij} \delta_{rs} (\delta_{i1} + \delta_{iN}), \quad (5.4.3)$$

$$\Sigma_{k,ij,rs}^<(\varepsilon) = -i \Gamma \delta_{ij} \delta_{rs} (\delta_{i1} f(\varepsilon - \mu_1) + \delta_{iN} f(\varepsilon - \mu_N)). \quad (5.4.4)$$

The difference in the chemical potential of the leads, $\mu_1 - \mu_N$, will drive a current through the system. We calculate the expectation value of the current via the equal-time lesser Greens function,

$$\mathbf{J}(t) = -i \text{Tr} \left(\hat{\mathbf{J}}(t) G^<(t, t) \right). \quad (5.4.5)$$

Here, the trace runs over all momenta k and the orbital and unit cell indices. The matrix elements of the current operator are

$$(\hat{J}_{z/y}(t))_{k,ij,rs} = \frac{\partial}{\partial k_{z/y}} M_{rs}(k_y, k_z + A_z \cos(\Omega t)) \delta_{ij}, \quad (5.4.6)$$

$$(\hat{J}_x(t))_{k,ij,rs} = \frac{t_\alpha}{2} \delta_{rs} (i e^{i A_x \cos(\Omega t)} \delta_{i,j+1} - i e^{-i A_x \cos(\Omega t)} \delta_{i+1,j}). \quad (5.4.7)$$

Below, we will calculate the time-averaged DC current, for which the x -component defined in the last line can be evaluated at an arbitrary unit cell index i_0 due to Kirchhoff's law of charge conservation.

Both the current operator and the equal-time lesser Greens function are periodic in t and can be expressed as a discrete Fourier series. Based on the definitions (5.3.36) and (5.3.37), the equal-time lesser Greens function can be written as

$$\begin{aligned} G_k^< &= \frac{1}{T} \int_0^T dt e^{ik\Omega t} G^<(t, t) \\ &= \sum_{m,n} \sum_{\alpha,\beta} \int_{-\frac{\Omega}{2}}^{\frac{\Omega}{2}} d\varepsilon \frac{|u_\alpha^{n+k}\rangle \langle v_\alpha^m|}{\varepsilon - \varepsilon_\alpha} \Sigma^<(\varepsilon + m\Omega) \frac{|v_\beta^m\rangle \langle u_\beta^n|}{\varepsilon - \varepsilon_\beta^*}. \end{aligned} \quad (5.4.8)$$

Here, the sum over α and β runs over all solutions to the eigenvalue equation

of the Floquet operator and not only the ones in the FBZ $[-\frac{\Omega}{2}, \frac{\Omega}{2}]$, because we used the identity (5.3.7) to rewrite sums over eigenvalues and Fourier indices. Furthermore, we broke the ε -integral over the real axis into several integrals covering the FBZ. In this way, a closed form expression for the ε -integral can be given for the zero-temperature limit using the identity

$$\int_a^b d\varepsilon \frac{1}{(\varepsilon - \varepsilon_\alpha)(\varepsilon - \varepsilon_\beta^*)} = \frac{1}{\varepsilon_\alpha - \varepsilon_\beta^*} \left(\log\left(\frac{b - \varepsilon_\alpha}{a - \varepsilon_\alpha}\right) - \log\left(\frac{b - \varepsilon_\beta^*}{a - \varepsilon_\beta^*}\right) \right), \quad (5.4.9)$$

with the boundaries a and b determined by the fermionic thermal distribution function $f(\varepsilon + m\Omega - \mu_i) = \Theta(-\varepsilon - m\Omega + \mu_i)$. The Fourier transformed current operator can also be obtained from the Floquet operator directly,

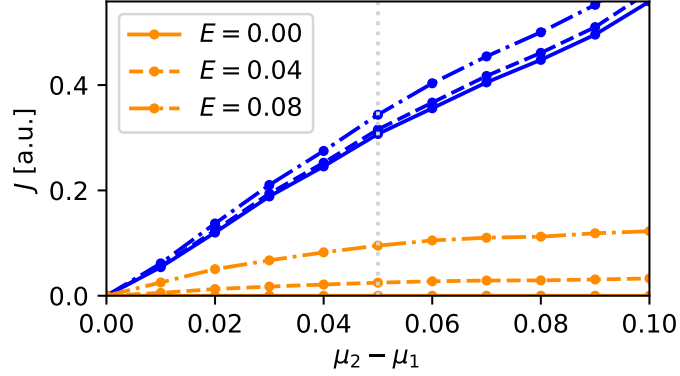
$$(\hat{J}_{y/z})_{n-m} = \frac{\partial Q_{mn}}{\partial k_{x/z}}, \quad (5.4.10)$$

$$\begin{aligned} (\hat{J}_x)_{n-m} &= \frac{\partial Q_{mn}}{\partial \tilde{A}_x}, \\ &= \sum_{k,r} \left(i (Q_{mn})_{k,i_0,i_0+1,r,r} c_{k,i_0,r}^\dagger c_{k,i_0+1,r} + \text{h.c.} \right), \end{aligned} \quad (5.4.11)$$

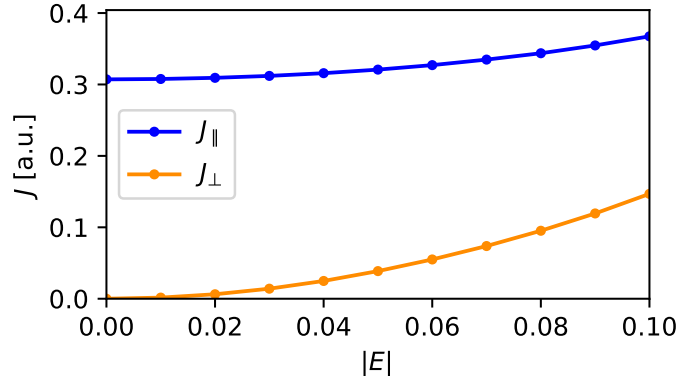
This is equivalent to evaluating the Fourier series of Eq. (5.4.7), because these operations commute. Finally, the frequency resolved current is given by

$$\mathbf{J}(n\Omega) = \text{Tr} \left(\sum_m \hat{\mathbf{J}}_{n-m} G_m^< \right). \quad (5.4.12)$$

We are interested in the DC current, i.e., the cycle average with $n = 0$. In Fig 5.4(b) we show the current for different amplitudes of circularly polarized light, $E_x = E_z$. For small driving amplitudes, the Hall current $J_\perp = J_z$ rises quadratically in the field strength. Changing E_x and E_z independently reveals a linear dependence in each component. This implies, that the Hall current vanishes for linear polarization and switches direction when going from right to left circular polarization. This is in accordance to the expectation from the effective model discussed in Sec. 5.3.2. The driving does not break the reflection symmetry in y -direction and the component J_y always



(a) Voltage dependence of longitudinal and anomalous Hall currents, J_{\parallel} and J_{\perp} , respectively, for various amplitudes of the driving field.



(b) Amplitude dependence along the gray dashed line $U = 0.05$ in (a).

Figure 5.4: Longitudinal (blue) and anomalous Hall current (orange) in the finite-sized driven nodal line system. The parameters of the nodal line are identical to the ones in Fig. 5.1 and the number of unit cells in x -direction is $N = 36$.

vanishes identically. In the case of strong driving, the longitudinal current $J_{\parallel} = J_x$ rises slightly with increasing driving intensity, see Fig. 5.4(b). This can be understood from the increasing weight of Floquet side bands, which effectively increases the availability of bands for conduction compared to the low density of states at Fermi level of the undriven NLSM.

Figure 5.4(a) shows the current for different voltages for three different driving amplitudes. The average chemical potential is kept at the level of the nodal line. Initially, all components of the current rise linearly, but the anomalous Hall current saturates for higher values of $\mu_N - \mu_1$. This strongly indicates that only the direct vicinity of the nodal line contributes to the Hall current and once the potential difference covers this interval, the contribution due to the Berry curvature saturates. Crossing of different Floquet side bands occur only outside the interval spanned by the chemical potentials of the leads, such that possible contributions from them are suppressed. Therefore no fine tuning of frequency is required for this effect. In this non-resonant condition, the driving frequency influences the result only by changing the amplitude of the vector potential $\mathbf{A} \propto \frac{1}{\Omega}$ for fixed electric field strength and thereby in the gap introduced in the nodal line.

5.5 Conductivity tensor

The calculation in the previous section shows linear response of the currents for a small potential difference. In this section we will evaluate the conductivity tensor in linear response theory. It is in this framework, that the Berry curvature can be identified as a direct contribution to the anomalous Hall conductivity [109].

The conductivity is a bulk quantity and, in contrast to the previous section, is independent of the transport measurement layout. However, this approach requires some simplifying assumptions. In this section, we assume that each degree of freedom is coupled uniformly and independently to the heat bath. This situation is for example given in a disorder averaged system coupled to some internal degrees of freedom, which are not affected by the driving and act as a correlation free thermal bath. In addition, we ne-

glect contributions from skew scattering at impurities here [125, 126]. We assume uniform coupling and a uniform chemical potential. The resulting formalism corresponds to an energy-independent finite lifetime. This setting preserves translation symmetry in all directions and all quantities can be expressed in three-dimensional \mathbf{k} -space. The self-energy terms defined in equations (5.3.26) and (5.3.32) are proportional to the identity matrix with respect to all indices, i.e., different crystal momenta or orbital degrees of freedom are not coupled,

$$\Sigma^R = i\frac{\Gamma}{2}\mathbf{1}, \quad (5.5.1)$$

$$\Sigma^<(\varepsilon) = i\Gamma f(\varepsilon)\mathbf{1}. \quad (5.5.2)$$

In this form, the retarded and advanced self-energy in the eigenvalue equations Eqs. (5.3.35a) and (5.3.35b) simplify to

$$(H_{m-n} \pm \frac{i}{2}\Gamma\delta_{mn} - n\Omega\delta_{mn})|u_\alpha^n\rangle = (\varepsilon_\alpha \pm \frac{i}{2}\Gamma)|u_\alpha^m\rangle. \quad (5.5.3)$$

The self-energies shift the real valued quasienergy eigenvalues ε_α into the complex plane by the constant factor of $\pm\frac{i}{2}\Gamma$ and we write out the imaginary part explicitly in this section. The eigenvectors $|u_\alpha\rangle$ are independent of the self-energy term and identical to the solutions of the hermitian eigenvalue equation, therefore no distinction has to be made between left and right eigenvectors.

In order to derive the conductivity tensor, we introduce the vector potential of a spatially homogeneous electric field, $\tilde{\mathbf{A}}^{\text{ext}}(t) = \frac{i}{\omega}\mathbf{E}^{\text{ext}}e^{i\omega t}$, in addition to the potential of the circularly polarized light. The total Hamiltonian reads $H(\mathbf{k} - \tilde{\mathbf{A}}(t) - \tilde{\mathbf{A}}^{\text{ext}}(t))$. We then expand Eq. (5.4.5) in the electric field up to linear order. Ultimately, we are interested in the DC conductivity, which is evaluated in the limit of vanishing ω . Therefore, the time-scale of the external electric field is large compared to the driving and the expansion can be done in the framework of the two-time method, where the long and short timescales are treated as independent variables in the derivatives and identified later [127]. The derivation is presented in Appendix C. In the

limit $\omega \rightarrow 0$, the conductivity is given entirely in terms of T -periodic quantities. We are interested in the DC current response, i.e., the cycle averaged contribution, which can be expressed in the Floquet eigenstate basis,

$$\sigma_{ij}^{\text{DC}} = \sum_{\alpha\beta\gamma} \sum_n \int_{-\frac{\Omega}{2}}^{\frac{\Omega}{2}} d\varepsilon \frac{(\hat{J}_i)_{\gamma\alpha} \Gamma \langle u_\alpha^n | f(\varepsilon + n\Omega) | u_\beta^n \rangle (\hat{J}_j)_{\beta\gamma}}{(\varepsilon - \varepsilon_\alpha + \frac{i\Gamma}{2})(\varepsilon - \varepsilon_\beta - \frac{i\Gamma}{2})(\varepsilon - \varepsilon_\gamma - \frac{i\Gamma}{2})^2} - \frac{(\hat{J}_i)_{\gamma\alpha} \Gamma \langle u_\beta^n | f(\varepsilon + n\Omega) | u_\gamma^n \rangle (\hat{J}_j)_{\alpha\beta}}{(\varepsilon - \varepsilon_\alpha + \frac{i\Gamma}{2})^2 (\varepsilon - \varepsilon_\beta - \frac{i\Gamma}{2})(\varepsilon - \varepsilon_\gamma + \frac{i\Gamma}{2})}, \quad (5.5.4)$$

with the matrix elements $(J_i)_{\alpha\beta} = \sum_{n,m} \langle u_\alpha^n | J_{n-m} | u_\beta^m \rangle$. Here, the indices α and β run over all solutions to the Floquet eigenvalue equations in- and outside the FBZ.

Note that in the case of vanishing driving amplitude, the Floquet side bands become decoupled with the full weight of an eigenstate on the zeroth index, $|u_\alpha^n\rangle = \delta_{n0} |u_\alpha^0\rangle$ for the bands whose quasienergy corresponds to the unperturbed energy. Additionally, the only non-zero component of the current operator is \hat{J}_0 . The lesser Greens function reduces to the spectral function $\mathcal{A} = \frac{i}{2\pi}(G^R - G^A)$ with inverse lifetime $\frac{\Gamma}{2}$, weighted by the Fermi distribution function $f(\varepsilon)$,

$$G_\alpha^<(\varepsilon) \Big|_{A=0} = \frac{i\Gamma f(\varepsilon)}{(\varepsilon - \varepsilon_\alpha)^2 + \frac{\Gamma^2}{4}} = -2i\pi \mathcal{A}(\varepsilon) f(\varepsilon). \quad (5.5.5)$$

Inserting this identity into Eq. (C.12) reproduces the formula for DC conductivity in time invariant systems in thermal equilibrium [128]. In Fig. 5.5 we show the time-averaged occupation of Floquet states $n_\alpha = \text{Tr}(G_\alpha^<)$, together with the projection of the states $|i\rangle$ of the undriven system, $n_i = \text{Tr}(|i\rangle \langle i| G^<)$. The majority of the weight lies on states in the first FBZ and the weight on side bands falls off quickly. The low weight on the side bands is a consequence of the locality of the Floquet operator with respect to the side-band index and justifies the use of a truncated matrix. The projection on the original bands shows, that the steady state solution mainly retains the distinction into valence and conduction bands, but the occupation number changes smoothly in the steady state solution despite the assumption of

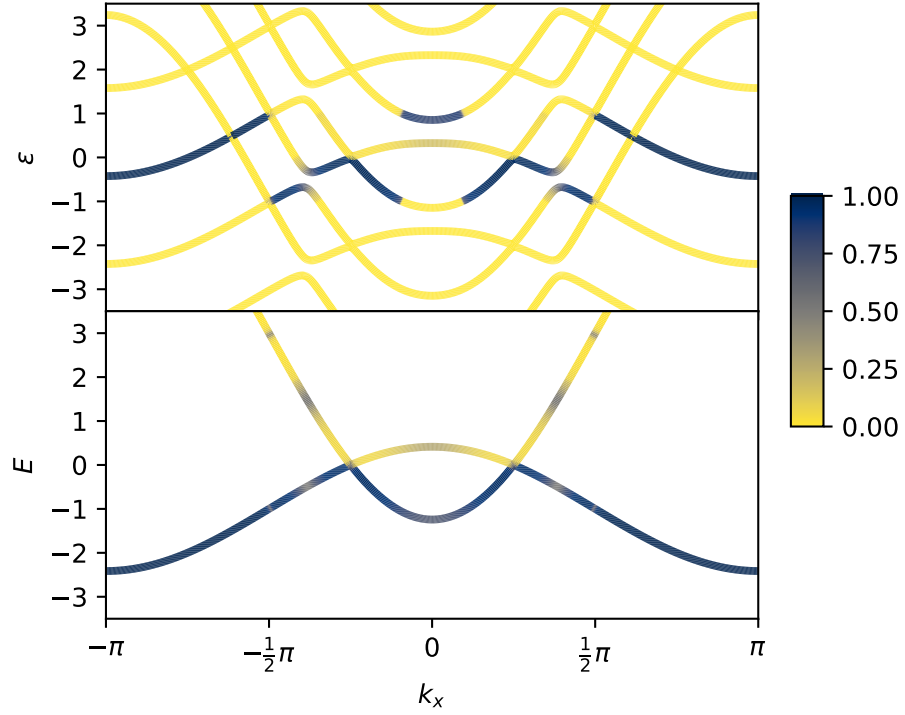


Figure 5.5: Floquet quasienergy bands $\varepsilon(\mathbf{k})$ color coded with their time-averaged occupation $n_\alpha = \text{Tr}(G_\alpha^<)$ (up), and original energy bands $E(\mathbf{k})$ with the projected average occupation $n_i = \text{Tr}(|i\rangle\langle i| G^<)$ (down) on the axis $(k_x, 0, 0)$ for the same parameters as in Fig. 5.1 and $\Gamma = 0.01$. The Floquet bands have been calculated for a truncated Floquet operator with $N_m = 5$. A close-up of the nodal line is shown in Fig. 5.9(b).

vanishing temperature. Exceptions from the valence and conduction band occupation are found at the Fermi level and for momenta, where the driving frequency is resonant to the gap. In the Floquet band structure, these cases correspond to the avoided crossings of Floquet bands.

Finally, we are in the position to evaluate the conductivity for various driving intensities. In Fig. 5.6 we show all non-vanishing contributions of the conductivity tensor. Despite the vanishing density of states at the nodal line, the longitudinal components do not vanish, because the occupation number changes smoothly over a finite energy range around the Fermi energy with non-vanishing density of states instead of a step function at the nodal line. The component σ_{zz} is scaled by a factor of 0.2 in the plot to better fit into the scale of the plot. The large difference to the other longitudinal components can be understood from the larger Fermi velocity in z -direction, which enters quadratically in the longitudinal conductivity. Additionally, the whole nodal line contributes uniformly, whereas the Fermi velocity in the perpendicular directions varies with the angle along the nodal line. With increasing driving strength, the longitudinal conductivity grows. This can be understood from the additional changes in occupation number at momenta where the driving becomes resonant. In agreement with the flow of Berry curvature in the effective model discussed in Sec. 5.3.2, only $\sigma_{xz} = -\sigma_{zx}$ acquires a non-zero contribution from the driving field. Again, we find linear dependence on each component E_x or E_z . The strength of the effect scales therefore quadratically on the driving amplitude, i.e., linearly on the intensity. A change in polarization corresponds to a sign change in either amplitude and therefore to a sign change in the conductivity. For comparison, we also evaluated the effective Floquet Hamiltonian based on the lattice model, using the ordinary expression for the conductivity of a static system with a finite lifetime in thermal equilibrium, shown as dotted lines in Fig. 5.6. It can be seen that the anomalous Hall conductivity is well captured from the effective model. The crossing of Floquet side bands is not captured and the assumptions for the effective model are not valid in the region in momentum space with resonant driving. Therefore, the enhancement of the longitudinal conductivity is also not captured. This shows that the Berry curvature provides a good explana-

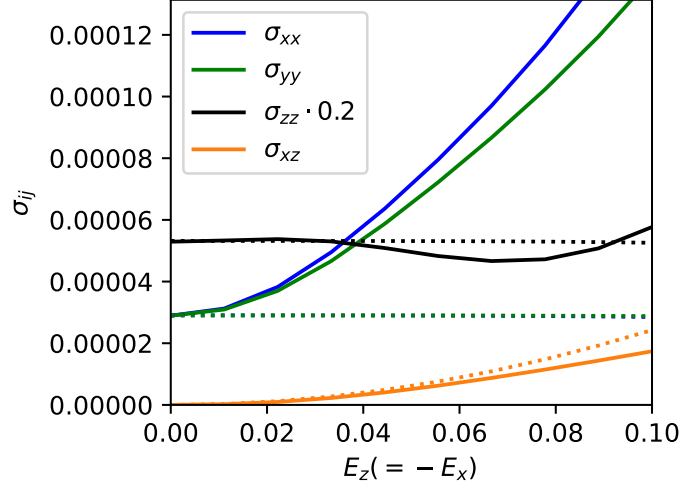


Figure 5.6: Conductivity as a function of driving amplitude $|E|$ for the driven NLSM with parameters as given in Fig. 5.1, $\Gamma = 0.1$. The anomalous Hall conductivity σ_{xz} grows linear with the intensity $|E|^2$ of the circularly polarized light. The dotted lines show the same quantities evaluated from the effective Floquet Hamiltonian.

tion of the anomalous Hall effect in the driven NLSM, but its contribution is overestimated by assuming a sharp Fermi-Dirac thermal distribution for the effective model.

In Fig. 5.7 we show the conductivity for different values of the chemical potential μ . The longitudinal components have a minimum at the nodal line, because of the low density of states. This can be seen from the effective model as well, with the shortcomings mentioned in the previous paragraph. The anomalous Hall component is largest with the chemical potential right at the energy of the nodal line, $\mu = 0$ and falls of when shifting the nodal line away from the Fermi energy, because the Berry curvature is largest at the nodal line and falls of quickly.

In undriven materials in thermal equilibrium, longitudinal and anomalous Hall conductivity are expected to scale with Γ^{-1} and Γ^0 for small lifetimes, respectively [109]. The Γ dependence is shown in Fig. 5.8 and shows an exponential decay for all components. Since the driven nodal line in the Floquet picture remains gapless at two points and the maximum gap is of

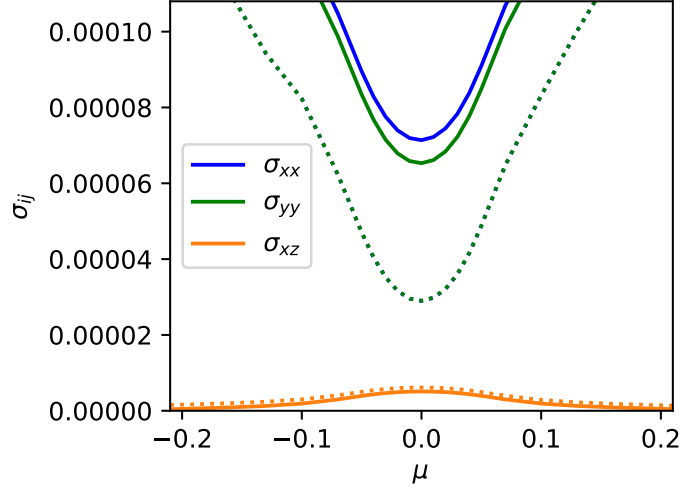


Figure 5.7: Chemical potential dependence of the longitudinal and transversal conductivity relative to the energy of the nodal line for $E_x = E_z = 0.05$. The dotted lines show the same quantities evaluated from the effective Floquet Hamiltonian.

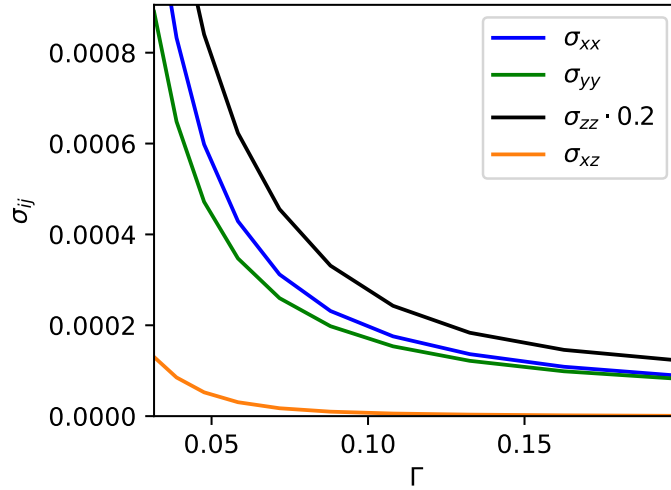


Figure 5.8: Lifetime dependence of the conductivity tensor components for $E_z = -E_x = 0.1$.

the order of the light intensity $|E|^2$, these limits do not apply, as there are always sections in the BZ, when the Γ is large compared to the gap size. In that case, there is no clear distinction between valence and conduction band, which limits the contribution of the Berry curvature to the anomalous Hall conductivity. A detailed view of the occupation of Floquet bands and original bands in the vicinity of the (maximally gapped) nodal line is shown in Fig. 5.9 for two different values of Γ . In the case $\Gamma = 0.1$, the occupation is of the order of the gap and there is no clear distinction in occupied and unoccupied bands. Furthermore, small values of Γ pose an additional challenge in evaluating the BZ integral numerically on a finite grid.

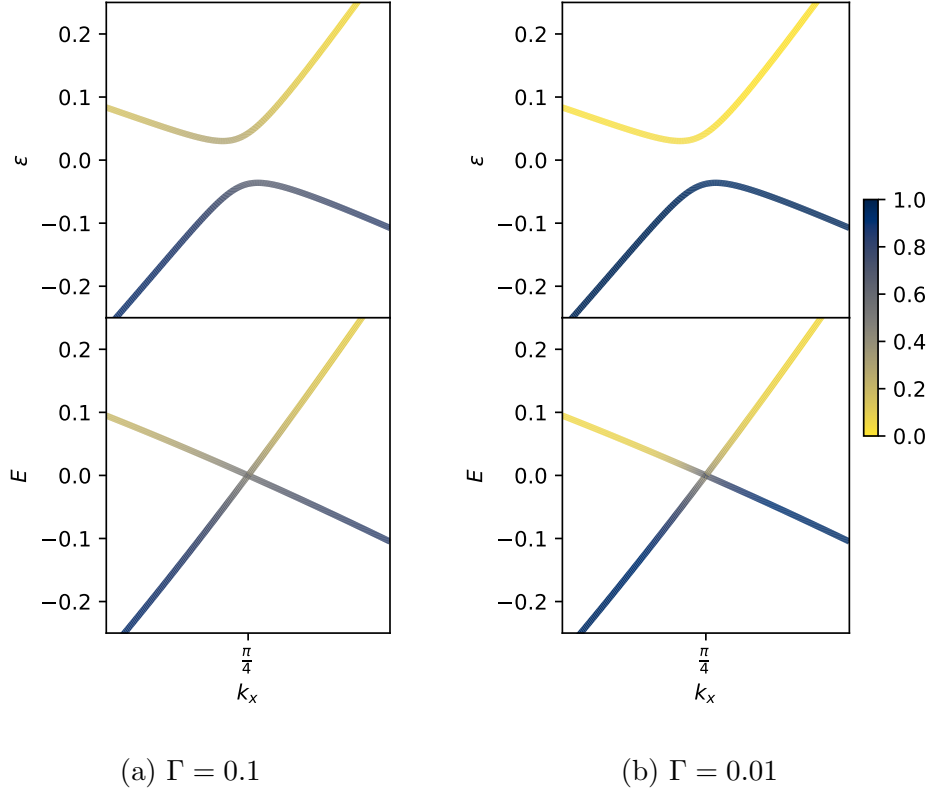


Figure 5.9: Detailed occupation of bands close to the nodal line for two different values of Γ .

The results confirm the calculation in the previous section of an anomalous Hall current induced by circularly polarized light. A quantitative comparison is, however, not possible due to the different assumptions in terms of the

coupling to the heat bath and the different treatment with respect to the x -direction and system size.

5.6 Real-time description

Recently, an anomalous Hall current induced by circularly polarized light has been measured in graphene [129], which is a lower dimensional analogue from a topological point of view. In the theoretical analysis of their results, the authors question the validity of the Floquet approach and the interpretation through the Berry curvature of dressed bands [130]. Motivated by these arguments, we calculate the current in the driven nodal-loop system field in the time domain.

We add a small static electric field along the x -direction order to drive a current through the system. For an electric field that is constant in time, its potential $\mathbf{A}^{\text{stat}}(t)$ has to grow linearly with t in the temporal gauge. The total time-dependent Hamiltonian reads then $H(\mathbf{k} - \tilde{\mathbf{A}}(t) - \mathbf{A}^{\text{stat}}(t))$. Both, the static and driving fields are smoothly switched on, one after the other. The static electric field is turned on first at time t_1 with smooth phase in time f_1 ,

$$\mathbf{A}^{\text{stat}}(t) = -E^{\text{stat}}\hat{\mathbf{e}}_x \times \begin{cases} 0 & t \leq t_1, \\ \left(\frac{t-t_1}{f_1}\right)^2 - \frac{1}{2}\frac{(t-t_1)^4}{f_1^3} & t_1 < t \leq t_1 + f_1, \\ t - t_1 - \frac{1}{2}f_1 & t > t_1 + f_1. \end{cases} \quad (5.6.1)$$

The amplitude of the driving field is modeled as a Gaussian with width f_2 before reaching its maximum at t_2 . After that, the amplitude is kept constant to achieve a steady state solution,

$$\tilde{\mathbf{A}}(t) = -\frac{1}{\Omega} \begin{pmatrix} E_x \cos \Omega t \\ 0 \\ E_z \sin \Omega t \end{pmatrix} \times \begin{cases} \exp\left(\frac{(t-t_2)^2}{2f_2^2}\right) & t < t_2, \\ 1 & t \geq t_2. \end{cases} \quad (5.6.2)$$

In this way, the increasing amplitude in the beginning resembles a short

pulse, whereas the rest of the calculation can still be compared to the Floquet solution, which assumes continuous driving. The x -component of the total potential is shown in the upper part of Fig. 5.10.

There are two contributions to the time evolution. The Hermitian part is given by the unitary time step $U(t + \Delta t, t) \approx e^{-iH(t)\Delta t}$. The uniform coupling $\frac{\Gamma}{2}$ to the heat bath introduced in the previous section corresponds to a finite lifetime $\tau = \frac{1}{\Gamma}$ after integrating out the bath degrees of freedom. We include this second, effectively non-Hermitian contribution via a factor proportional to the difference between the current state and the thermal equilibrium for the instantaneous eigenstates of the Hamiltonian $H(t)$. The discretized time evolution of the density matrix reads

$$\rho(t_{n+1}) = e^{-iH(t_n)\Delta t} \rho(t_n) e^{+iH(t_n)\Delta t} - \Delta t \Gamma (\rho(t_n) - \rho_{\text{eq}}(t_n)), \quad (5.6.3)$$

where $\rho_{\text{eq}}(t) = \sum_a f(E_a(t)) |a(t)\rangle \langle a(t)|$ is defined as the thermal equilibrium mixed state for the instantaneous eigenstates and eigenenergies, $H(t) |a(t)\rangle = E_a(t) |a(t)\rangle$. This also serves as the starting point of the evolution at t_0 , $\rho(t_0) = \rho_{\text{eq}}(t_0)$. In the basis of these instantaneous eigenstates, Eq. (5.6.3) can also be expressed component-wise,

$$\rho_{ab}(t_{n+1}) = e^{-i(E_a - E_b)\Delta t} \rho_{ab}(t_n) - \Delta t \Gamma (\rho_{ab}(t_n) - \delta_{ab} f(E_a)). \quad (5.6.4)$$

At each time step, we directly evaluate the current components $J_i(t_n) = \text{Tr}\left(\frac{\partial H(t_n)}{\partial k_i} \rho(t_n)\right)$. The resulting time-dependent current is dominated by the much larger driving field and oscillates strongly with the driving frequency. In order to identify the DC component, we average the current using a moving Gaussian filter with a width of $\sigma_{\text{Gauss}} = 2T$. By dividing the current components J_x and J_z by the strength of the static field E^{stat} , we can compare the results directly to the corresponding entries in the conductivity tensor, $\frac{J_x}{E^{\text{stat}}} = \sigma_{xx}$ and $\frac{J_z}{E^{\text{stat}}} = \sigma_{zx} = -\sigma_{xz}$, respectively. J_y and consequently σ_{yx} vanish identically. The remaining entries of the conductivity tensor are not probed in this setup. Because we calculate σ_{zx} instead of σ_{xz} , we use the opposite polarization for the driving field in this chapter, in order to end up

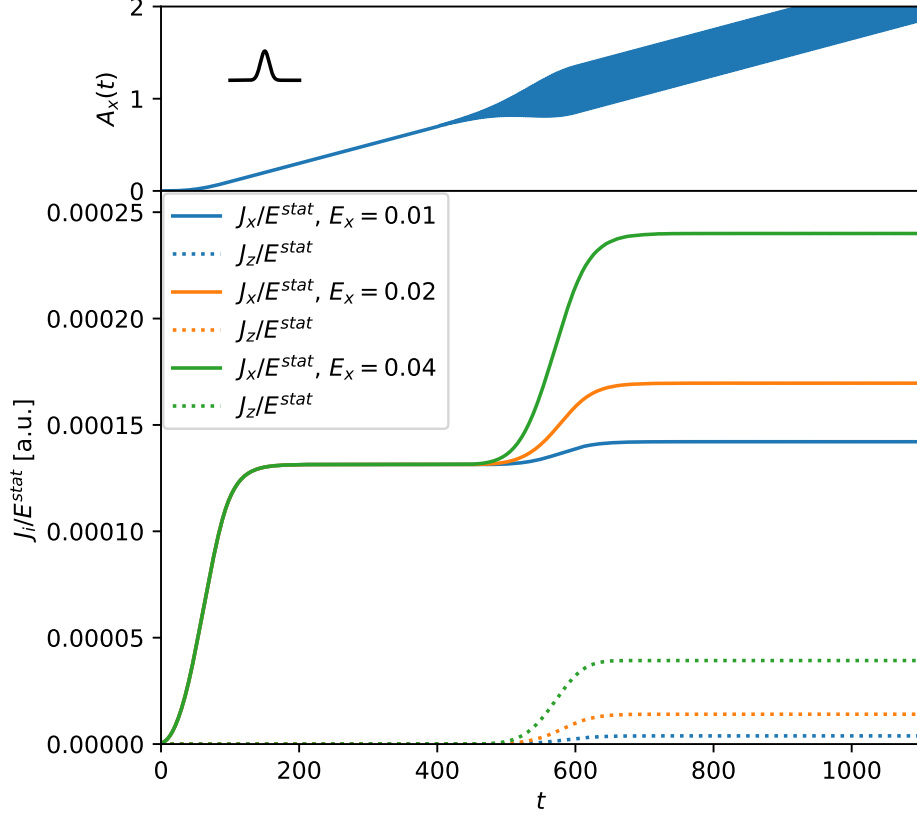


Figure 5.10: The upper part shows the x -component of the total electromagnetic potential $\tilde{A}_x(t) + A_x^{\text{stat}}(t)$ with the time scale in units of inverse hopping strength. For visual clarity, a larger driving amplitude has been chosen than in the results shown below. The static electric field is smoothly switched on at $t_1 = 0$ and reaches its final value at $t_1 + f_1 = 100$. The driving field reaches its maximal strength at $t_2 = 600$ and remains constant afterwards. The inset shows the Gaussian filter used for averaging the currents below. The lower plot shows the real-time calculation of the longitudinal current J_x and anomalous Hall current J_z (dotted) divided by the static field strength E^{stat} for different values of the driving field strength $E_x (= E_z)$. Apart from the polarization, which is reversed here, the parameters in the Hamiltonian are identical to the ones of the previous plots, c.f. Fig. 5.1. The relaxation to a steady state is given by the lifetime $\tau = \frac{1}{\Gamma} = 20$.

again with positive numbers for the anomalous Hall component.

Figure 5.10 shows the time-averaged currents for three different values of the driving amplitude. In all cases, the longitudinal current rises with the amplitude of the electric field and asymptotically approaches the steady state solution with the lifetime $\tau = \frac{1}{\Gamma}$. With the onset of the driving field, the longitudinal component increases and the anomalous Hall component becomes non-zero, reproducing the behavior seen in the previous chapters. The anomalous Hall current rises almost quadratically with the driving field, as seen for the conductivity, which in turn almost follows the quadratic increase of the effective model. For $\Gamma = 0.05$ and driving amplitudes $E_z = 0.01, 0.02$ and 0.04 , the anomalous Hall conductivity evaluated through the Floquet states is $1.1 \cdot 10^{-6}, 3.6 \cdot 10^{-6}$ and $1.1 \cdot 10^{-5}$, respectively, compared to $3.9 \cdot 10^{-6}, 1.4 \cdot 10^{-5}$ and $4.0 \cdot 10^{-5}$, when evaluated from the real-time calculations. The relative change with the driving amplitude agrees up to a few percent when comparing both methods. However, the two methods differ qualitatively, which is also the case for the longitudinal components. We attribute this difference partly to the way Γ enters the calculation, one the one hand as a coupling to the heat bath, one the other hand as an inverse lifetime for excited states. Fig. 5.11 shows the time-averaged current for two different values of Γ , showing a similar scaling behavior as in the previous chapter. In addition, the different times to reach a steady state solution can be seen in the parts where the static and driving fields are switched on.

Furthermore, the numerical evaluation of the three-dimensional model poses a challenge, as it limits the number of k -points. The evaluation of the integral in Eq. (5.5.4) on a finite grid requires a large enough Γ to reliably pick up the peaks created by the denominators. An estimate can be given by comparing the difference of quasienergy eigenvalues for neighboring k -points, $\frac{\Gamma}{2} \gtrsim \varepsilon(\mathbf{k}) - \varepsilon(\mathbf{k} + \Delta\mathbf{k})$. The step size is given by the number N_k of k -points per direction, $\Delta k_i = \frac{2\pi}{N_k}$. Around the nodal line, we find $\Delta\varepsilon \geq \Delta k_i = \frac{2\pi}{N_k}$ for the hopping strength used in the NLSM model. For the $N_k = 200$ points per spatial dimension used in the calculations, this requires $\Gamma \gtrsim 0.06$. In the time-evolution calculated in this chapter, a smaller Γ corresponds to a longer lifetime and ensures, that a steady state solution regarding the occupation of

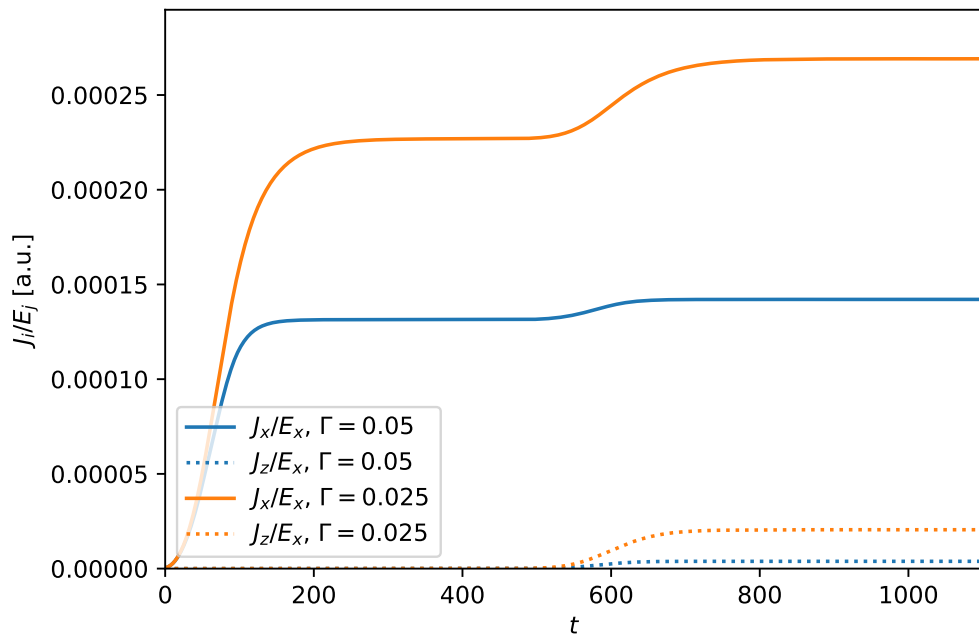


Figure 5.11: Time-averaged current for the same Hamiltonian and driving field as in Fig. 5.10, but for two different values of Γ and fixed driving strength $E_x = 0.01$.

an eigenstate of $H(\mathbf{k} - \mathbf{A}(t))$ can be achieved. A relevant time scale for this is given by the time it takes $\mathbf{A}^{\text{stat}}(t)$ to traverse the gap between two discrete k -points. Because the conductivity is valid only in the limit of vanishing E^{stat} , it has to be substantially smaller than the amplitude of the driving field and this component becomes the limiting factor. The estimated validity for Γ is then dictated by the relation $\frac{1}{\Gamma} \gtrsim \frac{\Delta k}{E^{\text{stat}}}$, which in our case requires $\Gamma \lesssim 0.06$. From these rough estimates it can be seen, that the two methods can only be compared in a very narrow range for Γ , in which they might already show numerical artifacts. Indeed, at close inspection oscillations can be seen in all components of $\mathbf{J}(t)$ with a period determined by E^{stat} and Δk , corresponding to a shifting k -grid on which the Fermi surface periodically gets sampled with more or less accuracy by the discrete k -mesh. At the same time, the scaling of the longitudinal components of the conductivity also deviates from the expected Γ^{-1} -scaling already in this regime. Moving away from the crossover regime, the two methods start to disagree also qualitatively. Although these numerical limitations prevent a qualitative comparison, the Hall angles, i.e., the ratio of longitudinal to transversal conductivity, agree within one percent in the crossover regime for small driving amplitudes, showing that the Berry curvature in the Floquet picture provides a good description of the anomalous Hall current for the driven NLSM.

5.7 Summary

In this chapter, we calculated the anomalous Hall current of a nodal-loop semimetal driven by circularly polarized light. In the Floquet picture, the driving can be understood as a symmetry breaking perturbation, which gaps the nodal line almost everywhere and turns the system into a Weyl semimetal. The flow of Berry curvature along the gapped nodal line leads to an anomalous Hall conductivity. The nodal loop in three dimensions falls into the same topological category as graphene and provides an analogue to the light-induced anomalous Hall effect there. In contrast to graphene, however, the circularly polarized light is not only needed to create an imbalance among canceling terms on opposite sides of the nodal ring, but also to introduce a

well-defined flow of Berry curvature.

We used three different methods to calculate the longitudinal and anomalous Hall currents or conductivities, each based on different assumptions for the coupling to a heat bath and for the static potential. The common signature for the light-induced anomalous Hall conductivity is a quadratic dependence on the field strength of the driving and a sign change when the polarization is flipped. More precisely, the anomalous Hall conductivity is proportional to the product of the two polarizations of the driving field and, thus vanishes exactly for light that is linearly polarized only in one direction. This can be readily understood from an effective Floquet Hamiltonian, as the symmetry breaking term contains the product of both polarization components. Another strong indicator for the relevance of the topology of Floquet bands is the strong dependence on chemical potential, i.e., the nodal line should be sufficiently close to the Fermi level to see this effect. For a concrete material, the preferred numerical method depends on the sample size and the values of Γ and Ω relative to the energy scale of the bands forming the nodal line. Furthermore, the Floquet approach relies on a sufficiently long driving pulse in relation to the driving frequency, which might become challenging in an experimental setup, where usually very high light intensities are required, leading to unwanted heating effects.

6. Conclusion

In this work, we investigated the topology of band crossings from a symmetry point of view, focusing on weakly correlated materials where interactions can be neglected. More concretely, in the first part of this work (Chapter 3) we identified all band crossings whose existence is enforced by combinations of spatial and non-spatial symmetries in band structures of orthorhombic and tetragonal space groups. This systematic analysis revealed a variety of degeneracies along points, lines and planes. Making extensive use of group representation theory, we further classified them in terms of their topological invariants. The analysis also took compatibility relations between representations at different high-symmetry points into account and identified several so-called movable crossings, that cannot be predicted from the local little group. Instead, global restrictions on the band structure imposed by the symmetry group have to be taken into account. These movable crossings must exist, but can be placed anywhere on a rotation axis or within a mirror plane. We considered both materials with strong and weak spin-orbit coupling, where the latter case also applies to bosonic and spinless band structures. Beyond the well known Weyl and Dirac points, we identified several different types of pointlike crossings of several bands or with larger Chern numbers. For each of these points or lines we gave a detailed description of the mechanism enforcing the degeneracy and provided a low-energy model. Notable examples are fourfold degenerate Weyl points with a Chern number of $\mathcal{C} = \pm 2$, which are found at high-symmetry points or as movable versions on one of three rotation axes. In the presence of a fourfold screw rotation, two of these are found superimposed at the same high-symmetry point, forming a fourfold degenerate point crossing with Chern number $\mathcal{C} = 4$. We also characterized

line crossings, which can be twofold or fourfold degenerate, some of which are enforced to exist by symmetry, but are not pinned to a high-symmetry axis. Finally, we also identified all space groups with symmetry-enforced nodal planes, some of which necessarily carry a topological charge. The main results of this chapter have been published in references [53, 54] and are summarized in comprehensive tables presented in Appendix B. Understanding the interplay of symmetry eigenvalues and representations provides insight into the stability of the nodes under symmetry breaking perturbations. For example, breaking one of the spatial symmetries might split a multifold Weyl point into several independent copies in the vicinity, while the sum of their Chern numbers is protected for any type of perturbation, as long as they remain separate from other Weyl points in the band structure.

The topology of band structures has become a new characteristic of compounds which is reported alongside the information about their symmetry. For example, the "Topological Quantum Chemistry" project already evaluates the topological classification of insulators and some other topological phases in an automatized manner and lists them in databases of known materials [24, 55]. Our results provide a compact reference to extend this classification for semimetals in the corresponding space groups. Since symmetry-enforced topology is valid for all band structures in a given space group, it can also be used as a guide in finding new topological materials. We have paired the systematic analysis of symmetry-enforced crossings with an automated screening of material databases to identify topologically interesting materials [53, 54], and thereby found interesting examples for many of the topological band crossings from the purely symmetry-based analysis. With these methods and results, we created a guide for identifying novel functional materials based on their topological properties and hope to inspire research into growing new compounds, especially in the nonsymmorphic chiral space groups, which have shown to be especially rich in symmetry-enforced topological band crossings of various kinds. The methods presented in this chapter can be used to extend the analysis to other space groups beyond the scope of this work, including also magnetic space groups, spin space groups and other spatial dimensions. In magnetic space groups, one might expect an

interesting topology in spin split bands from the various combinations of time-reversal symmetry and spatial symmetries.

In the second part of this work (Chapter 4) we took a closer look at observable consequences arising from a topological line crossing protected by a mirror symmetry. In this chapter, we studied a two band model that describes the low-energy physics of materials like CaAgP and CaAgAs, both of which have nodal lines close to the Fermi energy [90]. We investigated the bulk-boundary correspondence for such a nodal-line semimetal. It is still often claimed that a non-zero Zak phase leads in general to surface states, but we showed that there is no strict bulk-boundary correspondence for this particular model. However, we also demonstrated that a drumhead surface state is found for the relevant parameters used to describe these materials. A finite spin-orbit coupling introduces a topological gap at the nodal line, turning the semimetal into a weakly gapped topological insulator [95]. In this situation, the bulk-boundary correspondence can be applied and a spin-polarized surface state is guaranteed by the nontrivial bulk topology.

We then calculated the quasiparticle interference patterns resulting from scattering at a surface impurity. Due to the high weight in the surface density of states, the drumhead surface states dominate the quasiparticle interference spectrum at energies close to the nodal line. The interference pattern of a similar nodal line surface states has been measured recently [108]. Spin-resolved quasiparticle interference patterns from magnetic impurities can be measured in a spin-sensitive scanning tunneling microscope using a magnetic tip [103, 104]. We calculated the quasiparticle interference patterns for different orientations of the magnetization of tip and impurity and showed, that the structure of the spin polarized drumhead surface states can be resolved in the presence of sufficiently strong spin-orbit coupling [88]. The exponentially localized drumhead surface states of a nodal-line semimetal might provide an interesting platform in itself for experiments in weakly dispersing two-dimensional bands. These studies could be generalized to more complicated arrangements of surface states, for example for drumhead surface states of several nodal loops or ones that coexist with Fermi arcs.

In the last part of this work (Chapter 5), we explored the impact of the nodal line topology on the transport characteristics of the nodal-line semimetal. We calculated the longitudinal and transversal currents and the conductivity tensor for a nodal-line semimetal subject to periodic driving with circularly polarized light. We showed that the driven nodal-line semimetal acquires a non-zero anomalous Hall conductivity that grows with the square of the driving amplitude. This calculation was done in the Floquet formalism using various experimental setups and assumptions. The driving breaks the protecting symmetry of the nodal line. In the Floquet picture, the nodal-line semimetal turns into a Weyl semimetal and the anomalous Hall conductivity can be directly related to its topology. Finally, we compared the results to a simulation of the driven nodal-line semimetal in real time and identified the topology arising from the nodal line as the main contribution to the anomalous Hall effect. Albeit using the simplest model of a nodal line, these results are relevant for any nodal line close to the Fermi energy, including the symmetry-enforced ones identified in the Chapter 3. The sign and magnitude of the anomalous Hall current in the driven nodal-line semimetal depends on the polarization and strength of the driving field, respectively. This is one of the unique characteristics of this effect and allows to control the orientation and strength of the transversal current. It might provide a first step towards using the topology of nodal lines in functional materials, such as topological devices or sensors. Our results show that Floquet engineering can be used to design topological phases using the symmetry breaking of the driving field. In this way, nodal-line semimetals might provide a starting point to using the topology of Weyl and Dirac semimetals for several other transport quantities, e.g., the anomalous Nernst effect [131, 132] or the chiral photogalvanic effect [133], and the gyrotropic magnetic effect [34]. This might also be of relevance to other topological semimetals with inversion symmetry and topological transport characteristics.

A. Group action on crystal momentum

The action of a symmetry on a Bloch function $\Psi_{\alpha,\mathbf{k}}$ can be constructed by its decomposition into symmetry-adapted Wannier functions,

$$\Psi_{\alpha,\mathbf{k}}(\mathbf{r}) = \sum_{\mathbf{R}} e^{-i\mathbf{k}\mathbf{R}} \phi_{\alpha}(\mathbf{R} + \mathbf{r}). \quad (\text{A.1})$$

Here, α is an arbitrary multi-index for internal degrees of freedom like spin or orbital. The lattice vectors \mathbf{R} assign each Wannier function to a lattice point with the sum running over all lattice points. A spatial symmetry $\{R_i|\mathbf{t}_i\}$ with point group symmetry R_i and translational part \mathbf{t}_i acts on the coordinates of the Wannier function,

$$\{R_i|\mathbf{t}_i\} : \phi_{\alpha}(\mathbf{R} + \mathbf{r}) \rightarrow U_{\alpha\beta} \phi_{\beta}(R_i\mathbf{R} + R_i\mathbf{r} + \mathbf{t}_i). \quad (\text{A.2})$$

We use the Einstein summation convention and the unitary map $U_{\alpha\beta}$ contains phase factors or mapping between the internal degrees of freedom. We split the translational part of the symmetry into lattice vectors plus a fractional part, $\mathbf{t}_i = \mathbf{T}_i + \mathbf{t}'_i$ to separate the change in lattice site from the translation within a unit cell of the lattice. Using this decomposition, we can rewrite the sum in Eq. (A.1) via the substitution $\mathbf{R} \rightarrow R_i^{-1}(\mathbf{R} - \mathbf{T}_i)$, leading to

$$\begin{aligned} \{R_i|\mathbf{t}_i\} : \Psi_{\alpha\mathbf{k}}(\mathbf{r}) &\rightarrow e^{i\mathbf{k}R_i^{-1}\mathbf{T}_i} \sum_{\mathbf{R}} e^{-i\mathbf{k}R_i^{-1}\mathbf{R}} U_{\alpha\beta} \phi_{\beta}(\mathbf{R} + R_i\mathbf{r} + \mathbf{t}'_i) \\ &= e^{i\mathbf{k}'\mathbf{T}_i} U_{\alpha\beta} \Psi_{\beta,\mathbf{k}'}(R_i\mathbf{r} + \mathbf{t}'_i), \end{aligned} \quad (\text{A.3})$$

which is the symmetry-related Bloch wave function with crystal momentum $\mathbf{k}' = (R_i^{-1})^T \mathbf{k}$. In an orthonormal basis, the matrix of a point group symmetry is orthogonal, $R_i^{-1} = R_i^T$, and we simply find $\mathbf{k}' = R_i \mathbf{k}$. It can be readily seen, that the lattice part \mathbf{T}_i of the translation in the symmetry leads to a phase factor according to the transformed crystal momentum \mathbf{k}' .

Time reversal symmetry \mathcal{T} acts through complex conjugation and a unitary symmetry $U_{\alpha\beta}$, e.g., $U = i\sigma_y$ in spin space. The action in momentum space $\mathbf{k} \rightarrow -\mathbf{k}$ can be read of from

$$\begin{aligned}
\mathcal{T}\Psi_{\alpha,\mathbf{k}}(\mathbf{r}) &= \sum_{\mathbf{R}} e^{+i\mathbf{k}\mathbf{R}} \phi_{\alpha}^*(\mathbf{R} + \mathbf{r}) \\
&= \sum_{\mathbf{R}} e^{+i\mathbf{k}\mathbf{R}} U_{\alpha\beta} \phi_{\beta}(\mathbf{R} + \mathbf{r}) \\
&= U_{\alpha\beta} \Psi_{\beta,-\mathbf{k}}(\mathbf{r}).
\end{aligned} \tag{A.4}$$

B. Symmetry-enforced nodes in orthorhombic and tetragonal space groups

Here we present the result of our systematic search for symmetry-enforced nodal points, lines and planes in orthorhombic and tetragonal SGs discussed in Chapter. 3. For the orthorhombic SGs, we consider the spinless and spinful case, while we only present results for spinful band structures for the tetragonal SGs. The tables are further divided in noncentrosymmetric orthorhombic SGs (SG 16 – SG 46) and centrosymmetric orthorhombic SGs (SG 47 – SG 74) with and without SOC, and in noncentrosymmetric tetragonal SGs (SG 75–SG 82, SG 89–SG 122) and centrosymmetric tetragonal SGs (SG 83–SG 88, SG 123–SG 142) with SOC. Hexagonal and trigonal SGs with SOC have been investigated by others [72, 134] and spinless band structures in these SGs and the remaining families of SGs are left for future work.

Each line describes one SG given in terms of its number and Hermann–Mauguin symbol in the conventional setting [135]. The columns in each table are organized foremost by the dimensionality of the nodes, i.e., into point degeneracies, nodal lines, and planes. In the last column, we highlight notable or unique features. Throughout, we use a notation based on named points in the BZ of a SG family, as shown in Figures B.1 and B.2 for the orthorhombic and tetragonal lattices, respectively. High-symmetry lines are highlighted in color and are indicated in the tables by the two named points they connect, e.g., the entry Γ -Z refers to the line parametrized by $\mathbf{k} = (0, 0, w)$ in all

cases. Unlike the segments shown in the figure, these lines are not finite and w in the example covers the whole BZ. Symmetry-related segments are not shown explicitly. In the main text, we included the parametrisation in Cartesian coordinates explicitly. Intersecting lines can be written in a contracted form, e.g., Γ -Z-T means Γ -Z and Z-T. The Dirac or Weyl points of Sections 3.1–3.3 and 3.6 are listed in terms of the high-symmetry point they are pinned to, while movable point crossings are given in terms of the axis they are confined to, i.e., the entry Γ -Z in the column “points” means a movable point somewhere on this axis together with its symmetry-related copies. In a separate column, we list the pinned and movable nodal lines described in Sec. 3.7. Pinned nodal lines are listed explicitly in terms of the high-symmetry lines. Movable lines always lie between two sets of degenerate points with different mirror eigenvalue pairing. We indicate movable nodal lines by specifying these sets in terms of a tuple $(A; B)$. Left of the semicolon are all degeneracies where opposite eigenvalues are paired, while on the right the degeneracy is made up of two bands with identical eigenvalues. The sets A and B can be points, lines or combinations thereof. If a point appears on both sides of the semicolon, it must be fourfold degenerate and is written in italic font. Since such a crossing is not a point degeneracy at any level of bands, these fourfold degeneracies do not appear in the column “points”. Usually, all entries in the tuple identify the mirror plane uniquely, otherwise we specify it explicitly as a subscript. For nodal planes discussed in Sec. 3.4, we use Cartesian coordinates, aligned with the coordinate system shown in the figures. In spinful centrosymmetric SGs there are no nodal planes and we list insulating planes with a symmetry-enforced nontrivial weak invariant as described in Sec. 3.8, using the labels of the four TRIMs in the plane. The TRIM with identical fourfold inversion eigenvalue pairing is highlighted in bold font.

There are four Bravais lattice types compatible with the twofold rotations of the orthorhombic SGs: primitive, body-, face- and base-centered lattices. Their BZs are shown in Fig. B.1. In the absence of higher rotation symmetries, no symmetry axis is preferred. Since our analysis is based on symmetries alone with no concrete material in mind, we always use the align-

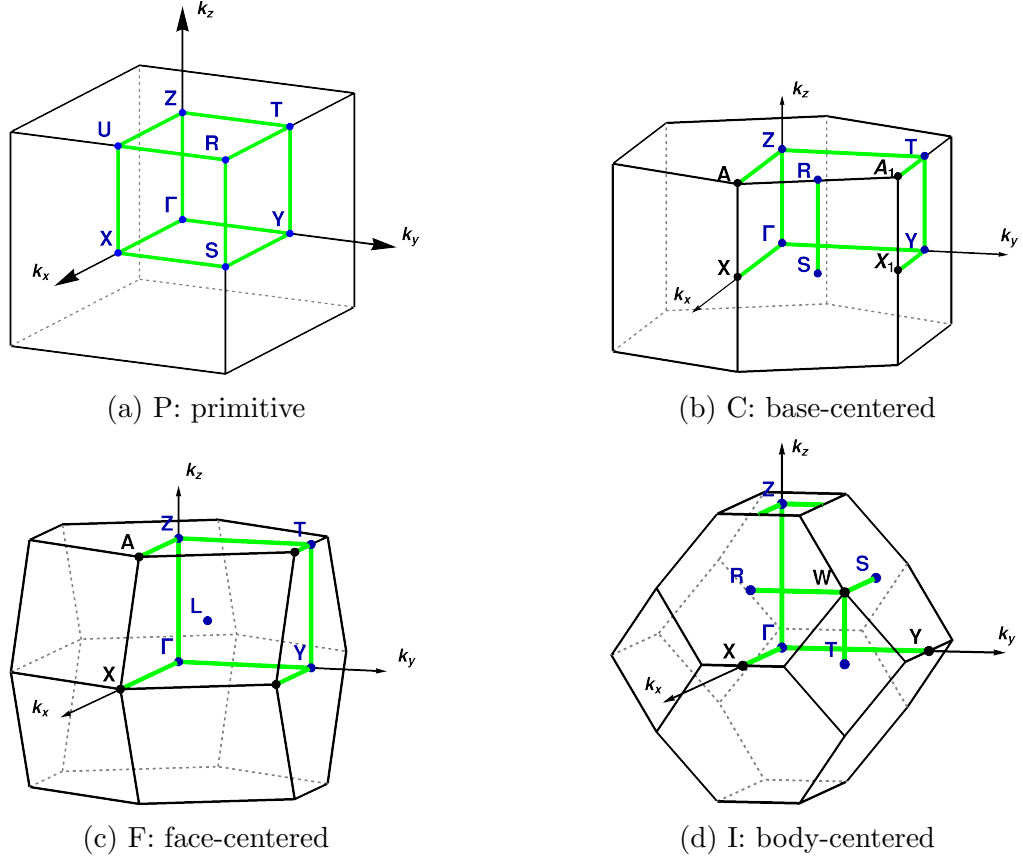


Figure B.1: Brillouin zones (BZs) of orthorhombic lattices with $a < b < c$. Of the several possibilities in the face-centered case, the one for $\frac{1}{a^2} = \frac{1}{b^2} + \frac{1}{c^2}$ is shown and used for labeling the points and axis. The BZ of side-centered lattices (SG 38–SG 41) is obtained from (b) by rotation around the Γ -Y axis, e.g. $Z = (\pi, 0, 0)$, Γ -X = $(0, 0, w)$, etc. TRIMs are labeled in blue, high-symmetry axes are shown in green and labeled by the points they are connecting. Figure adapted from Ref. [54].

ment as given by the Hermann–Mauguin symbol in the first column of tables. For example, SG 17 has the Hermann–Mauguin symbol $P222_1$, which means the screw rotation is aligned with the c -axis and its invariant points in the BZ are on the lines Γ -Z, X-U, S-R and Y-T. When comparing to results from high-throughput calculations, attention has to be paid to the convention, as the crystal axes are often sorted by their relative length, $a < b < c$ [62] and our results must be rotated accordingly. For example, SG 17 might then

alternatively read $P2_122$ or $P22_12$ and the movable Weyl point is found on the axis Γ -X or Γ -Y and their parallels, respectively.

Table I lists all symmetry-enforced band crossings in the noncentrosymmetric orthorhombic SGs for spinless bands. Table II covers the same SGs for spinful bands. The horizontal line separates the chiral SGs 16–24 from the ones including mirror symmetries. The centrosymmetric orthorhombic SGs are covered in Table III and IV, for the spinless and spinful cases, respectively. In the latter case, all bands are twofold degenerate and crossings are always Dirac points and lines. The overall twofold degeneracy is not included when specifying the number of bands involved in forming an hourglass dispersion.

SG	points	lines	nodal planes	notable features	
16 (P222)	Γ -[X \vee Y \vee Z](4), R(4)		$k_z = \pi$	fourfold double WP	
17 (P222 ₁)			$k_{x/y} = \pi$		
18 (P2 ₁ 2 ₁ 2)			$k_{x/y/z} = \pi$		
19 (P2 ₁ 2 ₁ 2 ₁)					
20 (C222 ₁)			$k_z = \pi$		
21 (C222)					
22 (F222)					
23 (I222)					
24 (I2 ₁ 2 ₁ 2 ₁)	Γ -[X \vee Y \vee Z](2), W(2)			only 4 WPs	
25 (Pmm2)			$k_z = \pi$		
26 (Pmc2 ₁)					
27 (Pcc2)			Z-U-R-T-Z		
28 (Pma2)			X-U-R-S-X		
29 (Pca2 ₁)			(U-X-S-R;U-R)		$k_z = \pi$
30 (Pnc2)			Z-U-R-S-Y-T-Z		
31 (Pmn2 ₁)			U-X-S-R		$k_z = \pi$
32 (Pba2)			X-U-R-T-Y-S-X		
33 (Pna2 ₁)			(S-X-U;U-R), S-Y-T		$k_z = \pi$
34 (Pnn2)			X-S-Y-T-Z-U-X		
35 (Cmm2)					
36 (Cmc2 ₁)					$k_z = \pi$
37 (Ccc2)			U-Z-T		
38 (Amm2)					
39 (Aem2)			R-S		
40 (Ama2)			A-Z-T		
41 (Aea2)			R-S, A-Z-T		

SYMMETRY-ENFORCED NODES IN ORTHORHOMBIC AND TETRAGONAL SPACE GROUPS

SG	points	lines	nodal planes	notable features
42 ($Fmm2$)				
43 ($Fdd2$)		A-Z-T-Y		
44 ($Imm2$)				
45 ($Iba2$)		R-W-S		
46 ($Ima2$)		R-W		

Table I: Symmetry-enforced band crossings in *spinless* band structures of *noncentrosymmetric* orthorhombic SGs. The second column shows all pointlike degeneracies. They can be on a high-symmetry point (e.g. Γ), somewhere on an axis connecting two high-symmetry points (e.g. Γ -Z) or on one of several axes (e.g. Γ -[X \vee Y \vee Z]) with \vee indicating the exclusive OR. Numbers in brackets indicate the total number of bands involved in the hourglass dispersion or crossing. The topological type of the degeneracies are listed under notable features, if it is different from a Weyl point (WP). The third column lists all symmetry-enforced nodal lines. The notation (A ; B) indicates an hourglass nodal line between two point- or linelike degeneracies A with eigenvalue pairing $(+, -)$ and B with $(+, +)$ or $(-, -)$. The fourth column lists all twofold degenerate nodal planes.

SG	points	lines	nodal planes	notable features
16 (P222) 17 (P222 ₁)	all TRIMs Γ, X, Y, S, Γ-Z(4), X-U(4), Y-T(4), S-R(4)		$k_z = \pi$	only 4 WPs
18 (P2 ₁ 2 ₁ 2)	Γ, Z, Γ-X(4), Γ-Y(4), Z-U(4), Z-T(4), S(4), R(4)		$k_{x/y} = \pi$	fourfold double WPs (n even), only 2 WPs (n odd)
19 (P2 ₁ 2 ₁ 2 ₁)	Γ, Γ-Z(4), Γ-X(4), Γ-Y(4), S(4), T(4), U(4), R-[S ∇ T ∇ U](8)		$k_{x/y/z} = \pi$	top. nodal plane trio, fourfold dou- ble WPs
20 (C222 ₁)	Γ, S, Y, Γ-Z(4), Y-T(4), S-R(4)		$k_z = \pi$	only 4 WPs
21 (C222)	all TRIMs			
22 (F222)	all TRIMs			
23 (I222)	all TRIMs, W			
24 (I2 ₁ 2 ₁ 2 ₁)	all TRIMs, W-[R ∇ S ∇ T](4)			
25 (Pmm2)		Γ-Z, X-U, Y-T, S-R		
26 (Pmc2 ₁)		(Γ-Z,Y-T;Z-T), (X-U,R-S;U-R)	$k_z = \pi$	
27 (Pcc2)	Z(4), T(4), U(4), R(4)	Γ-Z-U-R-T-Z, X-U, S-R, Y-T		fourfold points ($\mathcal{C}=0$)
28 (Pma2)		(Γ-Z;X,U), (Y-T;S,R), X-S, U-R		
29 (Pca2 ₁)		(Γ-Z;Z-U,X), (Y-T;S,R-T), (X-S;U-R)	$k_z = \pi$	
30 (Pnc2)	Z(4), U(4)	(Γ-Z-T;Y), (X-U-R;S), (Y-S;T,R), Z-U		nodal chain, four- fold points ($\mathcal{C}=0$)
31 (Pmn2 ₁)		(Γ-Z,T-Y;Z-T), (Γ-Z-U;X), (Y-T-R;S), X-S	$k_z = \pi$	

SYMMETRY-ENFORCED NODES IN ORTHORHOMBIC AND TETRAGONAL SPACE GROUPS

SG	points	lines	nodal planes	notable features
32 (<i>Pba</i> 2)	R(4), S(4)	(Γ -Z;Y,T), (Γ -Z;X,T), X-S-Y, U-R-T, S-R		fourfold points ($\mathcal{C}=0$)
33 (<i>Pna</i> 2 ₁)	S(4)	(<i>R</i> -S-X; <i>R</i> -U) (Γ -Z; <i>Z</i> -U,X), (Γ -Z-T;Y), Y-S	$k_z = \pi$	fourfold point ($\mathcal{C}=0$)
34 (<i>Pnn</i> 2)	Z(4), S(4)	(Γ -Z-T;Y), (Y-S-R;T), (Γ -Z-U;X), (X-S-R;U)		nodal chain, four- fold points ($\mathcal{C}=0$)
35 (<i>Cmm</i> 2)	R, S	Γ -Z, Y-T		only 4 WPs
36 (<i>Cmc</i> 2 ₁)	S, R-S(4)	(Γ -Z,Y-T; <i>Z</i> -T)	$k_z = \pi$	only 2 (4) WPs for <i>n</i> odd (even)
37 (<i>Ccc</i> 2)	R, S, Z(4), T(4)	Γ -Z-T-Y, Z-U		fourfold points ($\mathcal{C}=0$), only 4 WPs
38 (<i>Amm</i> 2)		(R;-), (S;-), Γ -X, Z-A		
39 (<i>Aem</i> 2)		(Γ -X;S), (Z-A;R), R-S		
40 (<i>Ama</i> 2)		(Γ -X;Z,T), (R;-), (S;-), Z-T		
41 (<i>Aea</i> 2)		(Γ -X;Z,T), (Γ -X;S), (Z-T;R), R-S		
42 (<i>Fmm</i> 2)	L	Γ -Z, Y-T		only 4 WPs
43 (<i>Fdd</i> 2)	L, Z(4)	(Γ -Z-T;Y) _{$k_x=0$} , (Γ -Z-A;T) _{$k_z=0$}		nodal chain, four- fold point, only 4 WPs
44 (<i>Imm</i> 2)	T	(R;-), (S;-), Γ -Z		only 2 WPs
45 (<i>Iba</i> 2)	T, T-W(4)	(Γ -Z;S,R), R-W-S		only 2 (4) WPs for <i>n</i> odd (even)
46 (<i>Ima</i> 2)	T	(Γ -Z;R), (S;-), R-W		only 2 WPs

Table II: Symmetry-enforced band crossings in band structures *with SOC* of *noncentrosymmetric* orthorhombic SGs. The notation is identical to the one in Table I. Additionally, almost movable lines are indicated by (*A*;-) with *A* being the high-symmetry point they run through as described in Sec. 3.7.4.

SG	points	lines	nodal planes	notable features
47 (<i>Pmmm</i>)				
48 (<i>Pnnn</i>)		Z-U-X-S-Y-T-Z		
49 (<i>Pccm</i>)		Z-U-R-T-Z		
50 (<i>Pban</i>)		X-U-R-T-Y-S-X		
51 (<i>Pmma</i>)			$k_x = \pi$	
52 (<i>Pnna</i>)		U-Z-T, X-S, (U-X-S;S-R)(4), (X-S,Y-S)(4)	$k_y = \pi$	precedes \mathbb{Z}_2 invariant (with SOC)
53 (<i>Pmna</i>)		U-X-S-R	$k_z = \pi$	
54 (<i>Pcca</i>)		R-T-Z-U, (Z-U;U-X)(4), (T-R;R-S)(4), (U-R;R-T-Z-U)	$k_x = \pi$	
55 (<i>Pbam</i>)			$k_x, k_y = \pi$	
56 (<i>Pccn</i>)		T-Z-U, (T-Z;Y-T)(4), (U-Z-T;U-R-T)(4), (Z-U;U-X)(4)	$k_x, k_y = \pi$	precedes \mathbb{Z}_2 invariant (with SOC)
57 (<i>Pbcm</i>)		R-T(4), (Y-T;T-Z)(4), (S-R;R-U)(4)	$k_y, k_z = \pi$	
58 (<i>Pnmm</i>)		T-Z-U	$k_x, k_y = \pi$	
59 (<i>Pmmn</i>)			$k_x, k_y = \pi$	
60 (<i>Pbcn</i>)		S-Y-T, U-R(4), (Y-T;T-Z)(4), (Z-U;U-X)(4), (R-S-Y-T;T-R)(4)	$k_x, k_z = \pi$	precedes \mathbb{Z}_2 invariant (with SOC)
61 (<i>Pbca</i>)		S-R(4), U-R-T(4), (Y-T;T-Z)(4), (Z-U;U-X)(4) (X-S;S-Y)(4)	$k_{x/y/z} = \pi$	
62 (<i>Pnma</i>)		S-R(4), (X-S;S-Y)	$k_{x/y/z} = \pi$	precedes \mathbb{Z}_2 invariant (with SOC)
63 (<i>Cmcm</i>)			$k_z = \pi$	
64 (<i>Cmca</i>)		S-R, (S;-)(2)	$k_z = \pi$	
65 (<i>Cmmm</i>)				
66 (<i>Cccm</i>)		A-Z-T		
67 (<i>Cmme</i>)		S-R, (S;-)(2), (R;-)(2)		
68 (<i>Ccce</i>)		A-Z-T,S-R, (S;-)(2), (R;-)(2)		
69 (<i>Fmmm</i>)				
70 (<i>Fddd</i>)		A-Z-T-Y		
71 (<i>Immm</i>)				

SYMMETRY-ENFORCED NODES IN ORTHORHOMBIC AND TETRAGONAL SPACE GROUPS

SG	points	lines	nodal planes	notable features
72 (<i>Ibam</i>)		S-W-R, (S;-)(2), (R;-)(2)		
73 (<i>Ibca</i>)	W(4)	S-W-R, W-T, (S;-)(2), (R;-)(2), (T;-)(2)		fourfold point ($C=0$) at half filling
74 (<i>Imma</i>)		W-T, (T;-)(2)		

Table III: Symmetry-enforced band crossings in *spinless* band structures of *centrosymmetric* orthorhombic SGs. The notation is identical to the one introduced in Tables I and II.

SG	points	lines	nontrivial \mathbb{Z}_2 planes	notable features
47 (<i>Pmmm</i>)				
48 (<i>Pnnn</i>)	S,T,U,X,Y,Z			
49 (<i>Pccm</i>)	R,T,U,Z			
50 (<i>Pban</i>)	R,S,T,U,X,Y			
51 (<i>Pmma</i>)		U-X, S-R		
52 (<i>Pnna</i>)	U,X,Z, X-S(4)	R-S-Y	ZUR T , XUY T	movable DP
53 (<i>Pmna</i>)	X,S	T-Z		
54 (<i>Pcca</i>)	T,Z, U-Z(4), R-T(4)	S-R-U-X		
55 (<i>Pbam</i>)		X-S-R-U, S-Y, R-T		
56 (<i>Pccn</i>)	Z, Z-U(4), Z-T(4)	Y-T-R-U-X, S-R	XUSR, YT SR	movable DP
57 (<i>Pbcm</i>)		U-R,S-Y,T-Z, (S-Y;R,T)(4)		only Dirac nodal line at half filling
58 (<i>Pnnm</i>)	Z	X-S-R,S-Y		
59 (<i>Pmnn</i>)		X-U,S-R,Y-T		
60 (<i>Pbcn</i>)	Y, T-Y(4)	X-U, R-T-Z, (X-U;R)(4), (R-T-Z;U)(4)	X STZ	Dirac nodal chain
61 (<i>Pbca</i>)		T-Z, (U-X;S)(4), (S-Y;T)(4), (T-Z;U)(4)	X YRZ	three Dirac nodal lines at half filling

SG	points	lines	nontrivial \mathbb{Z}_2 planes	notable features
62 (<i>Pnma</i>)		Z-U-X, U-R-T, S-Y, (R-U-X;S)	XUTY, ZURT	
63 (<i>Cmcm</i>)		(R;-), Z-T		
64 (<i>Cmca</i>)	S	Z-A		
65 (<i>Cmmm</i>)				
66 (<i>Cccm</i>)	T,Z			
67 (<i>Cmme</i>)	R,S			
68 (<i>Ccce</i>)	T,Z,R,S			
69 (<i>Fmmm</i>)				
70 (<i>Fddd</i>)	T,Y,Z			
71 (<i>Immm</i>)				
72 (<i>Ibam</i>)	R,S,W			
73 (<i>Ibca</i>)	R,S,T, W-[R \forall S \forall T](4)			movable DP
74 (<i>Imma</i>)	T			

Table IV: Symmetry-enforced band crossings in band structures *with SOC* of *centrosymmetric* orthorhombic SGs. The notation is identical to the one introduced in Tables I and II. All degeneracies are Dirac points (DP) and lines and the overall twofold degeneracy due to \mathcal{PT} -symmetry is not counted in the number of involved bands. There are no nodal planes and in the fourth column we list instead planes with a nontrivial \mathbb{Z}_2 invariant in terms of the TRIMs they contain. The TRIM with identical inversion eigenvalue pairing is highlighted in bold font.

There are two lattice types compatible with the tetragonal SG symmetries, the primitive lattice and the body-centered lattice. The fourfold rotation or rotoinversion defines the primary symmetry axis and relates the remaining symmetry axes to their equivalent perpendicular instances. Hence, there is no ambiguity in the orientation of the lattice with respect to the symmetry. The shape of the BZ for body-centered lattices depends on the relative length of lattice constants a and c . We use the BZ for the case $c < a$ for indicating high-symmetry lines based on labeled points. The results hold true in the other case as well, after identifying the appropriate parametrization in coordinates. As an example, the line $(0, 0, w)$ is given as Γ -Z-M and connects Γ and M = $(0, 0, 2\pi)$ along the k_z -axis. In the BZ for $c > a$, the

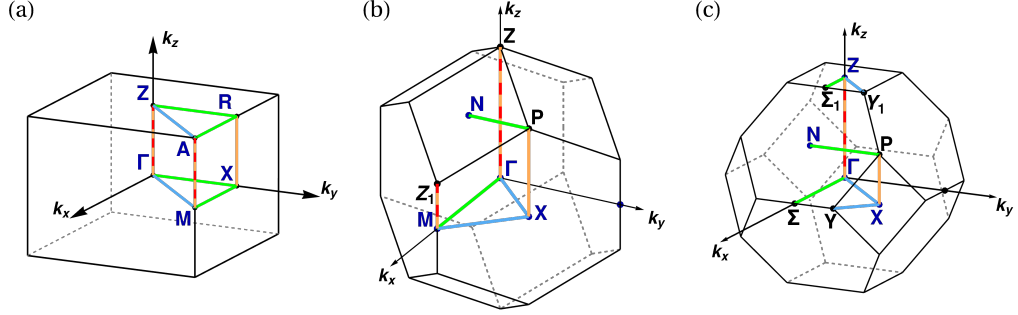


Figure B.2: Brillouin zones of the tetragonal crystal system with labeled high-symmetry points. TRIMs are highlighted in dark blue. Representative sections of high-symmetry lines are highlighted in color and correspond to the axis invariant under rotations. Namely, the fourfold rotation axis along the primary symmetry axis $[001]$ (red), and twofold rotations axis along $\langle 100 \rangle$ (green), $\langle 110 \rangle$ (light blue), and $[001]$ (orange). (a) Primitive BZ. (b) Body-centered BZ for $c < a$, used for defining symmetry axes of body-centered SGs in Tables V and VI. (c) Body-centered BZ for $c > a$. Figure adapted from Ref. [53].

point $(0, 0, 2\pi)$ is called Z, but any result holds equally on this axis. For the tetragonal SGs, we considered only the spinful representations relevant for band structures with non-negligible SOC. In contrast to the previous tables, pinned twofold points and lines are not given explicitly and we refer to tabulated representations, e.g., on the Bilbao Crystallographic Server [4, 3]. The only exceptions are Weyl and Dirac points at P in the body-centered BZ, mentioned explicitly in the column "notable features", as this is not a TRIM. For the noncentrosymmetric tetragonal SGs, given in Table V, we list all movable twofold point crossings in the first column and all fourfold point and line degeneracies in the second. The two cases of fourfold degenerate lines in SGs 113 and 114 are given by the symbol \overline{MA} and refer to the whole axis (π, π, w) . Otherwise, the notation is identical to the one defined previously. Table VI show the result for all centrosymmetric tetragonal SGs. In the second column, we list all pinned and movable Dirac points. Again, the number in brackets indicates the number of bands involved in an hourglass crossing and does not include the overall spin-degeneracy due to Kramers theorem. Pinned nodal lines can be found in the third column, indexed by

the points on the line as shown in Fig. B.2. There are no movable nodal lines or nodal planes in the centrosymmetric SGs, and only one case of a 2D subsystem with a symmetry-enforced nontrivial invariant.

SG	movable Weyl points	fourfold points & lines	movable lines	nodal planes	notable features
75 ($P4$)					
76 ($P4_1$)	Γ -Z(8), M-A(8), X-R(4)			$k_z = \pi$	double WP
77 ($P4_2$)	Γ -Z(4), M-A(4)				double WP
78 ($P4_3$)	Γ -Z(8), M-A(8), X-R(4)			$k_z = \pi$	double WP
79 ($I4$)					WP at P
80 ($I4_1$)	Γ -Z- M(4)				double WP, WP at P
81 ($P\bar{4}$)					
82 ($I\bar{4}$)					
89 ($P422$)					
90 ($P42_12$)	Γ -X(4), Z-R(4)	A, M		$k_{x/y} = \pi$	fourfold WP
91 ($P4_122$)	Γ -Z(8), M-A(8), X-R(4)			$k_z = \pi$	double WP
92 ($P4_12_12$)	Γ -Z(8), Γ -X(4)	M, R, A		$k_{x/y/z} = \pi$	top. nodal plane trio, twofold/four- fold (dou- ble/quadru- ple) WP
93 ($P4_222$)	Γ -Z(4), M-A(4)				double WP
94 ($P4_22_12$)	Γ -Z(4), Γ -X(4), Z-R(4)	A, M		$k_{x/y} = \pi$	top. nodal plane duo, double/four- fold WP

SYMMETRY-ENFORCED NODES IN ORTHORHOMBIC AND TETRAGONAL SPACE GROUPS

SG	movable Weyl points	fourfold points & lines	movable lines	nodal planes	notable features
95 ($P4_322$)	Γ -Z(8), M-A(8), X-R(4)			$k_z = \pi$	double WP
96 ($P4_3212$)	Γ -Z(8), Γ -X(4)	M, R, A		$k_{x/y/z} = \pi$	see SG 92
97 ($I422$)					WP at P
98 ($I4_122$)	Γ -Z- M(4)				WP at P
99 ($P4mm$)					
100 ($P4bm$)		M, A	$(\Gamma$ -Z;X,R)(4)		
101 ($P4_2cm$)		Z, A, R			
102 ($P4_2nm$)		Z, M	$(\Gamma$ -Z-R;X)(4), $(X$ -M-A;R)(4)		nodal chain metal
103 ($P4cc$)		Z, R, A			
104 ($P4nc$)		Z, M, A	$(\Gamma$ -Z-R;X)(4), $(X$ -M-A;R)(4)		nodal chain metal
105 ($P4_2mc$)		Z, A			
106 ($P4_2bc$)		Z, A, M, M-A(8)	$(\Gamma$ -Z;X,R)(4)		movable four- fold point
107 ($I4mm$)			$(N,\Gamma$ -Z,M- Z ₁ ;-)(2)		
108 ($I4cm$)		P	$(\Gamma$ -Z,M-Z ₁ ;N)(4)		
109 ($I4_1md$)		M	$(\Gamma$ -Z;X)(4), $(N,\Gamma$ -Z,M- Z ₁ ;-)(2)		WP at P, nodal chain metal
110 ($I4_1cd$)		M	$(\Gamma$ -Z,P;X)(4), $(\Gamma$ -Z,X;P)(4), $(X$ -M;P)(4), $(\Gamma$ -Z,M-Z ₁ ;N)(4), $(P,\Gamma$ -Z;-)(2), $(P,X$ -M-Z ₁ ;-)(2)		8N bands, in-gap nodal lines
111 ($P\bar{4}2m$)					
112 ($P\bar{4}2c$)		Z, A			
113 ($P\bar{4}2_1m$)	Γ -X(4), Z-R(4)	$\bar{M}\bar{A}$		$k_{x/y} = \pi$	fourfold line
114 ($P\bar{4}2_1c$)	Γ -X(4)	Z, $\bar{M}\bar{A}$		$k_{x/y} = \pi$	fourfold line
115 ($P\bar{4}m2$)					

SG	movable Weyl points	fourfold points & lines	movable lines	nodal planes	notable features
116 ($P\bar{4}c2$)		Z, A, R			
117 ($P\bar{4}b2$)		A, M	$(\Gamma\text{-Z};\text{X},\text{R})(4)$		
118 ($P\bar{4}n2$)	A-R(4), R-X(4)	Z, M	$(\Gamma\text{-Z-R};\text{X})(4)$ $(\text{X-M-A};\text{R})(4)$		nodal chain metal
119 ($I\bar{4}m2$)			$(\text{N},\Gamma\text{-Z},\text{M-Z}_1; -)(2)$		
120 ($I\bar{4}c2$)	X-P(4)		$(\Gamma\text{-Z},\text{M-Z}_1;\text{N})(4)$		
121 ($I\bar{4}2m$)					
122 ($I\bar{4}2d$)		M	$(\Gamma\text{-Z};\text{X})(4)$		nodal chain metal

Table V: Classification of band crossings in spinful bands with strong SOC for time-reversal symmetric, *noncentrosymmetric* tetragonal SGs, given in the first column. The second column lists all movable Weyl points in terms of the symmetry axis. The number in brackets indicates the total number of connected bands involved in enforcing the crossing, i.e., (4) for an hourglass crossing and (8) for an accordion state. In the third column we list pinned and movable fourfold degenerate points, as well as pinned fourfold degenerate lines. The latter ones are written with an overline to distinguish them from movable points. The third column contains movable and almost movable lines, as before indicated by the two sets of different eigenvalue pairing in a plane. In the fourth column we list all nodal planes and in the last column we highlight the most noteworthy features.

SG	Dirac points	Dirac lines	nontrivial \mathbb{Z}_2 planes	notable features
83 ($P4/m$)				
84 ($P4_2/m$)	Z, A			
85 ($P4/n$)	X, A, M, R			
86 ($P4_2/n$)	X, Z, M, R			
87 ($I4/m$)				
88 ($I4_1/a$)	X, M			
123 ($P4/mmm$)				
124 ($P4/mcc$)	A, Z, R			
125 ($P4/nbm$)	M, A, X, R			
126 ($P4/nnc$)	X, Z, A, R, M			

SYMMETRY-ENFORCED NODES IN ORTHORHOMBIC AND TETRAGONAL SPACE GROUPS

SG	Dirac points	Dirac lines	nontrivial \mathbb{Z}_2 planes	notable features
127 ($P4/mbm$)		M-X, A-M, A-R		
128 ($P4/mnc$)	Z	A-M, M-X		
129 ($P4/nmm$)		R-X, A-M		
130 ($P4/ncc$)	Z, R-Z(4), A(8)	R-X, A-M, A-R		movable DP, double DP
131 ($P4_2/mmc$)	Z, A			
132 ($P4_2/mcm$)	Z, R, A			
133 ($P4_2/nbc$)	X, Z, A, R, M, A-M(4)			movable DP
134 ($P4_2/nmm$)	X, Z, M, R			
135 ($P4_2/mbc$)	Z, A(8)	M-X, A-M, A-R		double DP
136 ($P4_2/mnm$)	Z	M-X, A-M		
137 ($P4_2/nmc$)	Z	A-M, R-X		
138 ($P4_2/ncm$)	Z, R-Z(4)	A-M, A-R, R-X	XMAR	movable DP
139 ($I4/mmm$)				
140 ($I4/mcm$)	N, P			
141 ($I4/amd$)	X, M			
142 ($I4_1/acd$)	X, M, N, P			DP at P

Table VI: Classification of symmetry-enforced band crossings in *centrosymmetric* tetragonal crystals with strong SOC. The second and third columns list the positions of pinned and movable Dirac points and pinned Dirac lines, respectively, following the notation of the previous tables. The fourth column lists two-dimensional planes within the BZ with an enforced nontrivial \mathbb{Z}_2 invariant, indicated by the four TRIMs in the plane, with the one with even parity highlighted in bold font. The last column highlights the most noteworthy features.

C. Derivation of DC conductivity for a periodically driven system

Without the external field there is no current due to symmetry, and we can define the entries of the polarization tensor $\Pi(t, \omega)$ as the coefficient of the lowest order expansion of the current component with respect to the amplitude component of the vector potential, $J_i(t, \omega) = \Pi_{ij}(t, \omega) A_j^{\text{ext}}$. By varying with respect to the amplitude, the frequency ω of the external field is incorporated in the definition of the polarization tensor directly. There are two contributions from the expansion,

$$\Pi_{ij}(t, \omega) = \left. \frac{\delta J_i}{\delta A_j^{\text{ext}}} \right|_{A^{\text{ext}}=0} = \text{Tr} \left(\hat{J}_i(t) \frac{\delta G^<(t, t)}{\delta A_j^{\text{ext}}} + \frac{\delta \hat{J}_i(t)}{\delta A_j^{\text{ext}}} G^<(t, t) \right). \quad (\text{C.1})$$

A graphical representation of the following calculation in terms of Feynman diagrams is shown in Fig. C.1. The wiggly lines represent the coupling to the field or the current expectation value, the dashed line represents the interaction with the bath. Starting with the derivative of the lesser Greens

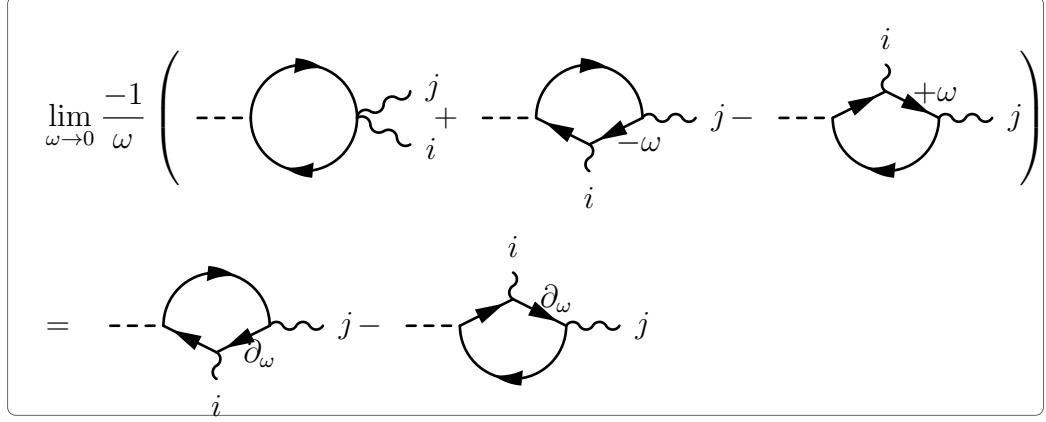


Figure C.1: Graphical representation of Eq. (C.12) in terms of Feynman diagrams. The dashed line represents the coupling to the bath, wiggly lines to the external electric field.

function, we first vary the retarded and advanced Greens functions,

$$\begin{aligned}
 \frac{\delta G^R}{\delta A_i^{\text{ext}}}(t, \varepsilon) &= \int dt' e^{i\varepsilon(t-t')} \int dt'' \frac{\delta G^R(t, t')}{\delta \tilde{A}_i^{\text{ext}}(t'')} \frac{\partial \tilde{A}_i^{\text{ext}}(t'')}{\partial A_i^{\text{ext}}} \\
 &= \int dt' e^{i\varepsilon(t-t')} \int dt'' G^R(t, t'') \frac{\partial H(t'')}{\partial k_i} e^{i\omega t''} G^R(t'', t') \\
 &= \sum_{n, m, m'} e^{i(\omega - n\Omega)t} G_{n-m}^R(\varepsilon - \omega + m\Omega) (\hat{J}_i)_{m-m'} G_{m'}^R(\varepsilon), \quad (\text{C.2})
 \end{aligned}$$

$$\begin{aligned}
 \frac{\delta G^A}{\delta A_i^{\text{ext}}}(t, \varepsilon) &= \int dt' e^{i\varepsilon(t-t')} \int dt'' G^A(t, t'') \frac{\partial H(t'')}{\partial k_i} e^{i\omega t''} G^A(t'', t') \\
 &= \sum_{n, m, m'} e^{i(\omega - n\Omega)t} G_{n-m}^A(\varepsilon) (J_i)_{m-m'} G_{m'}^A(\varepsilon + \omega + (m' - n)\Omega). \quad (\text{C.3})
 \end{aligned}$$

Inserting these relations into Eq. (5.3.33) leads to the expression

$$\frac{\delta G^<(t, t)}{\delta A_i} = \int d\varepsilon \frac{\delta G^R(t, \varepsilon)}{\delta A_i} \Sigma^<(\varepsilon) G^A(t, \varepsilon) + G^R(t, \varepsilon) \Sigma^<(\varepsilon) \frac{\delta G^A(t, \varepsilon)}{\delta A_i} \quad (\text{C.4})$$

$$= \int_{-\frac{\Omega}{2}}^{\frac{\Omega}{2}} d\varepsilon \sum_{m, n, q, r, s} e^{i(\omega - (m-s)\Omega)t} \left(G_{m-n}^R(\varepsilon + \omega + n\Omega) (\hat{J}_i)_{n-q} G_{q-r}^R(\varepsilon + r\Omega) \Sigma^<(\varepsilon + r\Omega) G_{r-s}^A(\varepsilon + r\Omega) \right. \\ \left. + G_{m-n}^R(\varepsilon + n\Omega) \Sigma^<(\varepsilon + n\Omega) G_{n-q}^A(\varepsilon + n\Omega) (\hat{J}_i)_{q-r} G_{r-s}^A(\varepsilon - \omega - r\Omega) \right). \quad (\text{C.5})$$

We introduce the shorter notation

$$g_{nm}^R(\varepsilon) = G_{n-m}^R(\varepsilon + m\Omega) = \sum_{\alpha} \frac{|u_{\alpha}^n\rangle \langle u_{\alpha}^m|}{\varepsilon - \varepsilon_{\alpha} + i\frac{\Gamma}{2}}, \quad (\text{C.6})$$

$$g_{nm}^A(\varepsilon) = G_{n-m}^A(\varepsilon + n\Omega) = \sum_{\alpha} \frac{|u_{\alpha}^n\rangle \langle u_{\alpha}^m|}{\varepsilon - \varepsilon_{\alpha} - i\frac{\Gamma}{2}}, \quad (\text{C.7})$$

as well as $(\hat{J}_i)_{n-m} = \frac{\partial Q_{mn}}{\partial k_i}$ and $\hat{\Sigma}_{mn}^<(\varepsilon) = \delta_{mn} \Sigma^<(\varepsilon + m\Omega)$, and write the above expression compactly as a matrix equation, implicitly including the Floquet indices,

$$\frac{\delta G^<(t, t)}{\delta A_i} = \int d\varepsilon \sum_{n, m} e^{i(\omega + (n-m)\Omega)t} \left(g^R(\varepsilon - \omega) \frac{\partial Q}{\partial k_i} g^R(\varepsilon) \hat{\Sigma}^<(\varepsilon) g^A(\varepsilon) \right. \\ \left. + g^R(\varepsilon) \hat{\Sigma}^<(\varepsilon) g^A(\varepsilon) \frac{\partial Q}{\partial k_i} g^A(\varepsilon + \omega) \right)_{nm}. \quad (\text{C.8})$$

The second term in Eq. (C.1) can be rewritten under the trace using partial integration in the momentum component,

$$\text{Tr} \left(\frac{\delta \hat{J}(t)}{\delta A_i} G^<(t, t) \right) = \text{Tr} \left(\frac{\partial \hat{J}(t)}{\partial k_i} e^{i\omega t} G^<(t, t) \right) \\ = - \text{Tr} \left(\hat{J}(t) e^{i\omega t} \frac{\partial G^<(t, t)}{\partial k_i} \right). \quad (\text{C.9})$$

In the notation introduced above, the equal time lesser Greens function reads $G_{mn}^< = \left(g^R(\varepsilon) \hat{\Sigma}^<(\varepsilon) g^A(\varepsilon) \right)_{mn}$, c.f., Eq. (5.4.8). Inserting the relation

$\frac{\partial g^{R/A}}{\partial k_i} = g^{R/A}(\varepsilon) \frac{\partial Q}{\partial k_i} g^{R/A}(\varepsilon)$, the k -derivative of the equal time lesser Greens function reproduces Eq. (C.3) with $\omega = 0$ in the argument of $g^{R/A}$. In total, we find

$$\begin{aligned} \Pi_{ij}(t, \omega) = \int d\varepsilon \sum_{n,m} \hat{J}(t) e^{i(\omega+(n-m)\Omega)t} & \left((g^R(\varepsilon - \omega) - g^R(\varepsilon)) \frac{\partial Q}{\partial k_i} g^R(\varepsilon) \hat{\Sigma}^<(\varepsilon) g^A(\varepsilon) \right. \\ & \left. + g^R(\varepsilon) \hat{\Sigma}^<(\varepsilon) g^A(\varepsilon) \frac{\partial Q}{\partial k_i} (g^A(\varepsilon + \omega) - g^A(\varepsilon)) \right)_{nm}. \end{aligned} \quad (\text{C.10})$$

Conductivity $\sigma_{ij}(t, \omega)$ is defined as the coefficient of linear expansion with respect to the electric field rather than the vector potential. Using the relation $\frac{\partial}{\partial E} = \frac{\partial A}{\partial E} \frac{\partial}{\partial A} = \frac{-1}{i\omega} \frac{\partial}{\partial A}$, the cycle averaged conductivity for a static field can be calculated from the polarization tensor by the relation

$$\sigma_{ij}^{\text{DC}} = \int_0^T \frac{dt}{T} \lim_{\omega \rightarrow 0} \frac{i}{\omega} \Pi_{ij}(t, \omega) \quad (\text{C.11})$$

$$\begin{aligned} &= -i \text{Tr} \int d\varepsilon \frac{\partial Q}{\partial k_i} \frac{\partial g^R(\varepsilon)}{\partial \varepsilon} \frac{\partial Q}{\partial k_j} g^R(\varepsilon) \hat{\Sigma}^<(\varepsilon) g^A(\varepsilon) \\ &\quad - \frac{\partial Q}{\partial k_i} g^R(\varepsilon) \hat{\Sigma}^<(\varepsilon) g^A(\varepsilon) \frac{\partial Q}{\partial k_j} \frac{\partial g^A(\varepsilon)}{\partial \varepsilon}. \end{aligned} \quad (\text{C.12})$$

Here, the trace includes the Floquet indices explicitly. Taking the limit $\omega \rightarrow 0$ turns the differences in Eq. (C.10) into derivatives and the DC conductivity tensor contains only Fourier components of \hat{J} and $G^{R/A}$. Changing into an eigenstate basis using $M_{\alpha\beta} = \sum_{mn} \langle u_\alpha^m | M_{mn} | u_\beta^n \rangle$ for all components reproduces Eq. (5.5.4) given in the main text.

Bibliography

- [1] Evgraf S Fedorov. The symmetry of regular systems of figures (Russian). *Proceedings of the Imperial St. Petersburg Mineralogical Society*, 28:1–146, 1891.
- [2] A Schönflies. Kristallsysteme und Kristallstruktur. *Leipzig: BG Taubner*, 1891.
- [3] Mois Iliá Aroyo, Juan Manuel Pérez-Mato, Cesar Capillas, Eli Kroumova, Svetoslav Ivantchev, Gotzon Madariaga, Asen Kirov, and Hans Wondratschek. Bilbao Crystallographic Server: I. Databases and crystallographic computing programs. *Zeitschrift für Kristallographie - Crystalline Materials*, 221(1):15 – 27, 01 Jan. 2006.
- [4] <https://www.cryst.ehu.es/>.
- [5] Michael Victor Berry. Quantal phase factors accompanying adiabatic changes. *Proceedings of the Royal Society of London. A. Mathematical and Physical Sciences*, 392(1802):45–57, 1984.
- [6] J. Zak. Berry’s phase for energy bands in solids. *Phys. Rev. Lett.*, 62:2747–2750, Jun 1989.
- [7] Gregory W. Moore. A comment on Berry connections. *arXiv e-prints*, arXiv:1706.01149, 2017.
- [8] D. Hsieh, D. Qian, L. Wray, Y. Xia, Y. S. Hor, R. J. Cava, and M. Z. Hasan. A topological Dirac insulator in a quantum spin Hall phase. *Nature*, 452(7190):970–974, 2008.

- [9] D. Hsieh, Y. Xia, L. Wray, D. Qian, A. Pal, J. H. Dil, J. Osterwalder, F. Meier, G. Bihlmayer, C. L. Kane, Y. S. Hor, R. J. Cava, and M. Z. Hasan. Observation of unconventional quantum spin textures in topological insulators. *Science*, 323(5916):919–922, 2009.
- [10] M. Z. Hasan and C. L. Kane. Colloquium: Topological insulators. *Rev. Mod. Phys.*, 82:3045–3067, Nov 2010.
- [11] K. v. Klitzing, G. Dorda, and M. Pepper. New method for high-accuracy determination of the fine-structure constant based on quantized Hall resistance. *Phys. Rev. Lett.*, 45:494–497, Aug 1980.
- [12] D. J. Thouless, M. Kohmoto, M. P. Nightingale, and M. den Nijs. Quantized Hall conductance in a two-dimensional periodic potential. *Phys. Rev. Lett.*, 49:405–408, Aug 1982.
- [13] Andreas P. Schnyder, Shinsei Ryu, Akira Furusaki, and Andreas W. W. Ludwig. Classification of topological insulators and superconductors in three spatial dimensions. *Phys. Rev. B*, 78:195125, Nov 2008.
- [14] Ching-Kai Chiu, Jeffrey C. Y. Teo, Andreas P. Schnyder, and Shinsei Ryu. Classification of topological quantum matter with symmetries. *Rev. Mod. Phys.*, 88:035005, Aug 2016.
- [15] Shinsei Ryu, Andreas P Schnyder, Akira Furusaki, and Andreas W W Ludwig. Topological insulators and superconductors: tenfold way and dimensional hierarchy. *New Journal of Physics*, 12(6):065010, jun 2010.
- [16] D. J. Thouless. Quantization of particle transport. *Phys. Rev. B*, 27:6083–6087, May 1983.
- [17] Takahiro Morimoto and Naoto Nagaosa. Topological nature of nonlinear optical effects in solids. *Science Advances*, 2(5):e1501524, 2016.
- [18] Takashi Oka and Hideo Aoki. Photovoltaic Hall effect in graphene. *Phys. Rev. B*, 79:081406, Feb 2009.

- [19] André Eckardt. Colloquium: Atomic quantum gases in periodically driven optical lattices. *Rev. Mod. Phys.*, 89:011004, Mar 2017.
- [20] Ivar Martin, Gil Refael, and Bertrand Halperin. Topological frequency conversion in strongly driven quantum systems. *Phys. Rev. X*, 7:041008, Oct 2017.
- [21] Frank Wilczek. Quantum time crystals. *Phys. Rev. Lett.*, 109:160401, Oct 2012.
- [22] Ching-Kai Chiu and Andreas P. Schnyder. Classification of reflection-symmetry-protected topological semimetals and nodal superconductors. *Phys. Rev. B*, 90:205136, Nov 2014.
- [23] Ching-Kai Chiu, Hong Yao, and Shinsei Ryu. Classification of topological insulators and superconductors in the presence of reflection symmetry. *Phys. Rev. B*, 88:075142, Aug 2013.
- [24] Barry Bradlyn, L. Elcoro, Jennifer Cano, M. G. Vergniory, Zhijun Wang, C. Felser, M. I. Aroyo, and B. Andrei Bernevig. Topological quantum chemistry. *Nature*, 547(7663):298–305, 2017.
- [25] Xiangang Wan, Ari M. Turner, Ashvin Vishwanath, and Sergey Y. Savrasov. Topological semimetal and Fermi-arc surface states in the electronic structure of pyrochlore iridates. *Phys. Rev. B*, 83:205101, May 2011.
- [26] A. A. Burkov and Leon Balents. Weyl semimetal in a topological insulator multilayer. *Phys. Rev. Lett.*, 107:127205, Sep 2011.
- [27] Gang Xu, Hongming Weng, Zhijun Wang, Xi Dai, and Zhong Fang. Chern semimetal and the quantized anomalous Hall effect in HgCr_2Se_4 . *Phys. Rev. Lett.*, 107:186806, Oct 2011.
- [28] Grigory E Volovik. *The universe in a helium droplet*, volume 117. OUP Oxford, 2003.

- [29] A. A. Burkov, M. D. Hook, and Leon Balents. Topological nodal semimetals. *Phys. Rev. B*, 84:235126, Dec 2011.
- [30] Meng Xiao and Shanhui Fan. Topologically charged nodal surface. *arXiv e-prints*, arXiv:1709.02363, Sep 2017.
- [31] Marc A Wilde, Matthias Doderhöft, Arthur Niedermayr, Andreas Bauer, Moritz M Hirschmann, Kirill Alpin, Andreas P Schnyder, and Christian Pfleiderer. Symmetry-enforced topological nodal planes at the Fermi surface of a chiral magnet. *Nature*, 594(7863):374–379, 2021.
- [32] D. T. Son and B. Z. Spivak. Chiral anomaly and classical negative magnetoresistance of Weyl metals. *Phys. Rev. B*, 88:104412, Sep 2013.
- [33] H.B. Nielsen and M. Ninomiya. A no-go theorem for regularizing chiral fermions. *Physics Letters B*, 105(2):219 – 223, 1981.
- [34] Felix Flicker, Fernando de Juan, Barry Bradlyn, Takahiro Morimoto, Maia G. Vergniory, and Adolfo G. Grushin. Chiral optical response of multifold fermions. *Phys. Rev. B*, 98:155145, Oct 2018.
- [35] R. Jackiw and C. Rebbi. Solitons with fermion number $\frac{1}{2}$. *Phys. Rev. D*, 13:3398–3409, Jun 1976.
- [36] Yasuhiro Hatsugai. Chern number and edge states in the integer quantum Hall effect. *Phys. Rev. Lett.*, 71:3697–3700, Nov 1993.
- [37] Yasuhiro Hatsugai. Edge states in the integer quantum Hall effect and the Riemann surface of the Bloch function. *Phys. Rev. B*, 48:11851–11862, Oct 1993.
- [38] Xiao-Liang Qi, Yong-Shi Wu, and Shou-Cheng Zhang. General theorem relating the bulk topological number to edge states in two-dimensional insulators. *Phys. Rev. B*, 74:045125, Jul 2006.
- [39] A. Bravais. Mémoire sur les systèmes formés par les points distribués régulièrement sur un plan ou dans l’espace. 1850.

- [40] Issai Schur. Neue Begründung der Theorie der Gruppencharaktere. *Sitzungsberichte der Königlich Preussischen Akademie der Wissenschaften zu Berlin*, page 406–432, 1905.
- [41] Léon Brillouin. Les électrons libres dans les métaux et le rôle des réflexions de Bragg. *J. phys. radium*, 1(11):377–400, 1930.
- [42] Ch. Mauguin. Sur le symbolisme des groupes de répétition ou de symétrie des assemblages cristallins. *Zeitschrift für Kristallographie - Crystalline Materials*, 76(1-6):542–558, 1931.
- [43] C. Hermann. Bemerkung zu der vorstehenden Arbeit von Ch. Mauguin. *Zeitschrift für Kristallographie - Crystalline Materials*, 76(1-6):559–561, 1931.
- [44] Mikio Nakahara. *Geometry, topology and physics*. CRC press, 2018.
- [45] Jennifer Cano, Barry Bradlyn, Zhijun Wang, L. Elcoro, M. G. Vergniory, C. Felser, M. I. Aroyo, and B. Andrei Bernevig. Building blocks of topological quantum chemistry: Elementary band representations. *Phys. Rev. B*, 97:035139, Jan 2018.
- [46] Jennifer Cano and Barry Bradlyn. Band representations and topological quantum chemistry. *Annual Review of Condensed Matter Physics*, 12(1):225–246, Mar 2021.
- [47] Jean-Pierre Serre. Faisceaux algébriques cohérents. *Annals of Mathematics*, 61(2):197–278, 1955.
- [48] Richard G. Swan. Vector bundles and projective modules. *Transactions of the American Mathematical Society*, 105(2):264–277, 1962.
- [49] Jeffrey C. Y. Teo and C. L. Kane. Topological defects and gapless modes in insulators and superconductors. *Phys. Rev. B*, 82:115120, Sep 2010.

- [50] A. Alexandradinata, Xi Dai, and B. Andrei Bernevig. Wilson-loop characterization of inversion-symmetric topological insulators. *Phys. Rev. B*, 89:155114, Apr 2014.
- [51] Barry Simon. Holonomy, the quantum adiabatic theorem, and Berry's phase. *Phys. Rev. Lett.*, 51:2167–2170, Dec 1983.
- [52] Takahiro Fukui, Yasuhiro Hatsugai, and Hiroshi Suzuki. Chern numbers in discretized Brillouin zone: Efficient method of computing (spin) Hall conductances. *Journal of the Physical Society of Japan*, 74(6):1674–1677, 2005.
- [53] Moritz M. Hirschmann, Andreas Leonhardt, Berkay Kilic, Douglas H. Fabini, and Andreas P. Schnyder. Symmetry-enforced band crossings in tetragonal materials: Dirac and Weyl degeneracies on points, lines, and planes. *Phys. Rev. Materials*, 5:054202, May 2021.
- [54] Andreas Leonhardt, Moritz M. Hirschmann, Niclas Heinsdorf, Xianxin Wu, Douglas H. Fabini, and Andreas P. Schnyder. Symmetry-enforced topological band crossings in orthorhombic crystals: Classification and materials discovery. *Phys. Rev. Materials*, 5:124202, Dec 2021.
- [55] Anubhav Jain, Shyue Ping Ong, Geoffroy Hautier, Wei Chen, William Davidson Richards, Stephen Dacek, Shreyas Cholia, Dan Gunter, David Skinner, Gerbrand Ceder, and Kristin a. Persson. The Materials Project: A materials genome approach to accelerating materials innovation. *APL Materials*, 1(1):011002, 2013.
- [56] <https://materialsproject.org/>.
- [57] G Bergerhoff and ID Brown. Crystallographic databases/Allen FH et al.(Hrsg.). Chester. *International Union of Crystallography*, 1987.
- [58] <https://icsd.fiz-karlsruhe.de/>.
- [59] Shyue Ping Ong, Shreyas Cholia, Anubhav Jain, Miriam Brafman, Dan Gunter, Gerbrand Ceder, and Kristin A. Persson. The materials

- application programming interface (API): A simple, flexible and efficient API for materials data based on REpresentational State Transfer (REST) principles. *Computational Materials Science*, 97:209–215, feb 2015.
- [60] Anubhav Jain, Geoffroy Hautier, Charles J. Moore, Shyue Ping Ong, Christopher C. Fischer, Tim Mueller, Kristin A. Persson, and Gerbrand Ceder. A high-throughput infrastructure for density functional theory calculations. *Computational Materials Science*, 50(8):2295–2310, 2011.
- [61] Anubhav Jain, Geoffroy Hautier, Shyue Ping Ong, Charles J. Moore, Christopher C. Fischer, Kristin A. Persson, and Gerbrand Ceder. Formation enthalpies by mixing GGA and GGA + U calculations. *Phys. Rev. B*, 84:045115, Jul 2011.
- [62] Wahyu Setyawan and Stefano Curtarolo. High-throughput electronic band structure calculations: Challenges and tools. *Computational materials science*, 49(2):299–312, 2010.
- [63] Hermann Weyl. Quantenmechanik und Gruppentheorie. *Zeitschrift für Physik*, 46(1-2):1–46, 1927.
- [64] Su-Yang Xu, Ilya Belopolski, Nasser Alidoust, Madhab Neupane, Guang Bian, Chenglong Zhang, Raman Sankar, Guoqing Chang, Zhu-jun Yuan, Chi-Cheng Lee, Shin-Ming Huang, Hao Zheng, Jie Ma, Daniel S. Sanchez, BaoKai Wang, Arun Bansil, Fangcheng Chou, Pavel P. Shibayev, Hsin Lin, Shuang Jia, and M. Zahid Hasan. Discovery of a Weyl fermion semimetal and topological Fermi arcs. *Science*, 349(6248):613–617, 2015.
- [65] Guoqing Chang, Benjamin J Wieder, Frank Schindler, Daniel S Sanchez, Ilya Belopolski, Shin-Ming Huang, Bahadur Singh, Di Wu, Tay-Rong Chang, Titus Neupert, et al. Topological quantum properties of chiral crystals. *Nature materials*, 17(11):978–985, 2018.

- [66] Stepan S. Tsirkin, Ivo Souza, and David Vanderbilt. Composite Weyl nodes stabilized by screw symmetry with and without time-reversal invariance. *Phys. Rev. B*, 96:045102, Jul 2017.
- [67] Tiantian Zhang, Ryo Takahashi, Chen Fang, and Shuichi Murakami. Twofold quadruple Weyl nodes in chiral cubic crystals. *Phys. Rev. B*, 102:125148, Sep 2020.
- [68] Chaoxi Cui, Xiao-Ping Li, Da-Shuai Ma, Zhi-Ming Yu, and Yugui Yao. Charge-four Weyl point: Minimum lattice model and chirality-dependent properties. *Phys. Rev. B*, 104:075115, Aug 2021.
- [69] Shin-Ming Huang, Su-Yang Xu, Ilya Belopolski, Chi-Cheng Lee, Guoqing Chang, Tay-Rong Chang, BaoKai Wang, Nasser Alidoust, Guang Bian, Madhab Neupane, Daniel Sanchez, Hao Zheng, Horng-Tay Jeng, Arun Bansil, Titus Neupert, Hsin Lin, and M. Zahid Hasan. New type of Weyl semimetal with quadratic double Weyl fermions. *Proceedings of the National Academy of Sciences*, 113(5):1180–1185, 2016.
- [70] Weikang Wu, Zhi-Ming Yu, Xiaoting Zhou, Y. X. Zhao, and Shengyuan A. Yang. Higher-order Dirac fermions in three dimensions. *Phys. Rev. B*, 101:205134, May 2020.
- [71] Zhijun Wang, Aris Alexandradinata, Robert J Cava, and B Andrei Bernevig. Hourglass fermions. *Nature*, 532(7598):189–194, 2016.
- [72] J. Zhang, Y.-H. Chan, C.-K. Chiu, M. G. Vergniory, L. M. Schoop, and A. P. Schnyder. Topological band crossings in hexagonal materials. *Phys. Rev. Materials*, 2:074201, Jul 2018.
- [73] G. Gatti, D. Gosálbez-Martínez, S. S. Tsirkin, M. Fanciulli, M. Puppini, S. Polishchuk, S. Moser, L. Testa, E. Martino, S. Roth, Ph. Bugnon, L. Moreschini, A. Bostwick, C. Jozwiak, E. Rotenberg, G. Di Santo, L. Petaccia, I. Vobornik, J. Fujii, J. Wong, D. Jariwala, H. A. Atwater, H. M. Rønnow, M. Chergui, O. V. Yazyev, M. Grioni, and A. Crepaldi. Radial spin texture of the Weyl fermions in chiral tellurium. *Phys. Rev. Lett.*, 125:216402, Nov 2020.

- [74] Akira Furusaki. Weyl points and Dirac lines protected by multiple screw rotations. *Science Bulletin*, 62(11):788–794, 2017.
- [75] Luis Elcoro, Barry Bradlyn, Zhijun Wang, Maia G. Vergniory, Jennifer Cano, Claudia Felser, B. Andrei Bernevig, Danel Orobengoa, Gemma de la Flor, and Mois I. Aroyo. Double crystallographic groups and their representations on the Bilbao Crystallographic Server. *Journal of Applied Crystallography*, 50(5):1457–1477, Oct 2017.
- [76] Meng Xiao, Liping Ye, Chunyin Qiu, Hailong He, Zhengyou Liu, and Shanhui Fan. Experimental demonstration of acoustic semimetal with topologically charged nodal surface. *Science Advances*, 6(8):eaav2360, 2020.
- [77] M. G. Vergniory, L. Elcoro, Zhijun Wang, Jennifer Cano, C. Felser, M. I. Aroyo, B. Andrei Bernevig, and Barry Bradlyn. Graph theory data for topological quantum chemistry. *Phys. Rev. E*, 96:023310, Aug 2017.
- [78] Zhi-Ming Yu, Weikang Wu, Y. X. Zhao, and Shengyuan A. Yang. Circumventing the no-go theorem: A single Weyl point without surface Fermi arcs. *Phys. Rev. B*, 100:041118, Jul 2019.
- [79] G. A. Wiegers. The crystal structure of the low-temperature form of silver selenide. *Am. Mineral.*, 56:1882–1888, 1971.
- [80] Lisa Siggelkow, Viktor Hlukhyy, and Thomas F. Fässler. Sr_7Ge_6 , Ba_7Ge_6 and Ba_3Sn_2 — Three new binary compounds containing dumbbells and four-membered chains of tetrel atoms with considerable Ge–Ge π -bonding character. *Journal of Solid State Chemistry*, 191:76–89, 2012.
- [81] Paul Adrien Maurice Dirac. The quantum theory of the electron. *Proceedings of the Royal Society of London. Series A, Containing Papers of a Mathematical and Physical Character*, 117(778):610–624, 1928.

- [82] Barry Bradlyn, Jennifer Cano, Zhijun Wang, M. G. Vergniory, C. Felser, R. J. Cava, and B. Andrei Bernevig. Beyond Dirac and Weyl fermions: Unconventional quasiparticles in conventional crystals. *Science*, 2016.
- [83] Bohm-Jung Yang, Troels Arnfred Bojesen, Takahiro Morimoto, and Akira Furusaki. Topological semimetals protected by off-centered symmetries in nonsymmorphic crystals. *Phys. Rev. B*, 95:075135, Feb 2017.
- [84] Thomas F Fässler and Christian Kronseder. NaSn₅: An intermetallic compound with covalent α -tin and metallic β -tin structure motifs. *Angewandte Chemie International Edition*, 37(11):1571–1575, 1998.
- [85] Tomáš Bzdušek, QuanSheng Wu, Andreas Rüegg, Manfred Sigrist, and Alexey A. Soluyanov. Nodal-chain metals. *Nature*, 538(7623):75–78, 2016.
- [86] Shan-Shan Wang, Ying Liu, Zhi-Ming Yu, Xian-Lei Sheng, and Shengyuan A Yang. Hourglass Dirac chain metal in rhenium dioxide. *Nature communications*, 8(1):1–7, 2017.
- [87] Liang Fu and C. L. Kane. Topological insulators with inversion symmetry. *Phys. Rev. B*, 76:045302, Jul 2007.
- [88] Mehdi Biderang, Andreas Leonhardt, Nimisha Raghuvanshi, Andreas P. Schnyder, and Alireza Akbari. Drumhead surface states and their signatures in quasiparticle scattering interference. *Phys. Rev. B*, 98:075115, Aug 2018.
- [89] Qiunan Xu, Rui Yu, Zhong Fang, Xi Dai, and Hongming Weng. Topological nodal line semimetals in the CaP₃ family of materials. *Phys. Rev. B*, 95:045136, Jan 2017.
- [90] Ai Yamakage, Youichi Yamakawa, Yukio Tanaka, and Yoshihiko Okamoto. Line-node Dirac semimetal and topological insulating phase in noncentrosymmetric pnictides CaAg X (X= P, As). *J. Phys. Soc. Jpn*, 85(1):013708, 2015.

-
- [91] Daichi Takane, Kosuke Nakayama, Seigo Souma, Taichi Wada, Yoshihiko Okamoto, Koshi Takenaka, Youichi Yamakawa, Ai Yamakage, Taichi Mitsuhashi, Koji Horiba, et al. Observation of Dirac-like energy band and ring-torus Fermi surface associated with the nodal line in topological insulator CaAgAs. *npj Quantum Materials*, 3(1):1, 2018.
- [92] N. Xu, Y. T. Qian, Q. S. Wu, G. Autès, C. E. Matt, B. Q. Lv, M. Y. Yao, V. N. Strocov, E. Pomjakushina, K. Conder, N. C. Plumb, M. Radovic, O. V. Yazyev, T. Qian, H. Ding, J. Mesot, and M. Shi. Trivial topological phase of CaAgP and the topological nodal-line transition in CaAg(P_{1-x}As_x). *Phys. Rev. B*, 97:161111, Apr 2018.
- [93] David Vanderbilt and R. D. King-Smith. Electric polarization as a bulk quantity and its relation to surface charge. *Phys. Rev. B*, 48:4442–4455, Aug 1993.
- [94] Jun-Won Rhim, Jan Behrends, and Jens H. Bardarson. Bulk-boundary correspondence from the intercellular Zak phase. *Phys. Rev. B*, 95:035421, Jan 2017.
- [95] C. K. Chiu, Y. H. Chan, and A. P. Schnyder. Quantized Berry phase and surface states under reflection symmetry or space-time inversion symmetry. *arXiv e-prints*, arXiv:1810.04094, 2018.
- [96] A. S. Sergeev. Geometry of projected connections, Zak phase, and electric polarization. *Phys. Rev. B*, 98:161101, Oct 2018.
- [97] Mikhail Pletyukhov, Dante M. Kennes, Jelena Klinovaja, Daniel Loss, and Herbert Schoeller. Topological invariants to characterize universality of boundary charge in one-dimensional insulators beyond symmetry constraints. *Phys. Rev. B*, 101:161106, Apr 2020.
- [98] Mikhail Pletyukhov, Dante M. Kennes, Jelena Klinovaja, Daniel Loss, and Herbert Schoeller. Surface charge theorem and topological constraints for edge states: Analytical study of one-dimensional nearest-neighbor tight-binding models. *Phys. Rev. B*, 101:165304, Apr 2020.

- [99] Y.-H. Chan, Ching-Kai Chiu, M. Y. Chou, and Andreas P. Schnyder. Ca_3P_2 and other topological semimetals with line nodes and drumhead surface states. *Phys. Rev. B*, 93:205132, May 2016.
- [100] J. E. Hoffman, E. W. Hudson, K. M. Lang, V. Madhavan, H. Eisaki, S. Uchida, and J. C. Davis. A four unit cell periodic pattern of quasi-particle states surrounding vortex cores in $\text{Bi}_2\text{Sr}_2\text{CaCu}_2\text{O}_{8+\delta}$. *Science*, 295(5554):466–469, 2002.
- [101] K McElroy, RW Simmonds, JE Hoffman, D-H Lee, J Orenstein, H Eisaki, S Uchida, and JC Davis. Relating atomic-scale electronic phenomena to wave-like quasiparticle states in superconducting $\text{Bi}_2\text{Sr}_2\text{CaCu}_2\text{O}_{8+\delta}$. *Nature*, 422(6932):592–596, 2003.
- [102] L. Capriotti, D. J. Scalapino, and R. D. Sedgewick. Wave-vector power spectrum of the local tunneling density of states: Ripples in a d-wave sea. *Phys. Rev. B*, 68:014508, Jul 2003.
- [103] Daniel T Pierce. Spin-polarized electron microscopy. *Physica Scripta*, 38(2):291, 1988.
- [104] M Bode. Spin-polarized scanning tunnelling microscopy. *Reports on Progress in Physics*, 66(4):523, 2003.
- [105] Lukas Muechler, Andreas Topp, Raquel Queiroz, Maxim Krivenkov, Andrei Varykhalov, Jennifer Cano, Christian R. Ast, and Leslie M. Schoop. Modular arithmetic with nodal lines: Drumhead surface states in ZrSiTe . *Phys. Rev. X*, 10:011026, Feb 2020.
- [106] M Mofazzel Hosen, Gyanendra Dhakal, Baokai Wang, Narayan Poudel, Klauss Dimitri, Firoza Kabir, Christopher Sims, Sabin Regmi, Krzysztof Gofryk, Dariusz Kaczorowski, et al. Experimental observation of drumhead surface states in SrAs_3 . *Scientific reports*, 10(1):1–9, 2020.

- [107] Weiyin Deng, Jiuyang Lu, Feng Li, Xueqin Huang, Mou Yan, Jiahong Ma, and Zhengyou Liu. Nodal rings and drumhead surface states in phononic crystals. *Nature communications*, 10(1):1–6, 2019.
- [108] B. A. Stuart, Seokhwan Choi, Jisun Kim, Lukas Muechler, Raquel Queiroz, Mohamed Oudah, L. M. Schoop, D. A. Bonn, and S. A. Burke. Quasiparticle interference observation of the topologically nontrivial drumhead surface state in ZrSiTe. *Phys. Rev. B*, 105:L121111, Mar 2022.
- [109] Johannes Mitscherling. Longitudinal and anomalous Hall conductivity of a general two-band model. *Phys. Rev. B*, 102:165151, Oct 2020.
- [110] W. B. Rui, Y. X. Zhao, and Andreas P. Schnyder. Topological transport in Dirac nodal-line semimetals. *Phys. Rev. B*, 97:161113, Apr 2018.
- [111] O. Gunawan, Y. P. Shkolnikov, K. Vakili, T. Gokmen, E. P. De Poortere, and M. Shayegan. Valley susceptibility of an interacting two-dimensional electron system. *Phys. Rev. Lett.*, 97:186404, Nov 2006.
- [112] Di Xiao, Wang Yao, and Qian Niu. Valley-contrasting physics in graphene: Magnetic moment and topological transport. *Phys. Rev. Lett.*, 99:236809, Dec 2007.
- [113] Ching-Kit Chan, Netanel H. Lindner, Gil Refael, and Patrick A. Lee. Photocurrents in Weyl semimetals. *Phys. Rev. B*, 95:041104, Jan 2017.
- [114] Hideo Sambe. Steady states and quasienergies of a quantum-mechanical system in an oscillating field. *Phys. Rev. A*, 7:2203–2213, Jun 1973.
- [115] Motohiko Ezawa. Photoinduced topological phase transition from a crossing-line nodal semimetal to a multiple-Weyl semimetal. *Phys. Rev. B*, 96:041205, Jul 2017.

- [116] Alexey A Soluyanov, Dominik Gresch, Zhijun Wang, QuanSheng Wu, Matthias Troyer, Xi Dai, and B Andrei Bernevig. Type-II Weyl semimetals. *Nature*, 527(7579):495–498, 2015.
- [117] Kai-Yu Yang, Yuan-Ming Lu, and Ying Ran. Quantum Hall effects in a Weyl semimetal: Possible application in pyrochlore iridates. *Phys. Rev. B*, 84:075129, Aug 2011.
- [118] A. A. Burkov. Topological response in ferromagnets. *Phys. Rev. B*, 89:155104, Apr 2014.
- [119] A. A. Burkov. Anomalous Hall effect in Weyl metals. *Phys. Rev. Lett.*, 113:187202, Oct 2014.
- [120] Sigmund Kohler, Jörg Lehmann, and Peter Hänggi. Driven quantum transport on the nanoscale. *Physics Reports*, 406(6):379–443, 2005.
- [121] Antti-Pekka Jauho, Ned S. Wingreen, and Yigal Meir. Time-dependent transport in interacting and noninteracting resonant-tunneling systems. *Phys. Rev. B*, 50:5528–5544, Aug 1994.
- [122] Alex Kamenev. *Field theory of non-equilibrium systems*. Cambridge University Press, 2011.
- [123] Ben Vollmayr-Lee. Alex Kamenev: Field theory of non-equilibrium systems. *Journal of Statistical Physics*, 148(6):1104–1105, 2012.
- [124] M. Büttiker. Absence of backscattering in the quantum Hall effect in multiprobe conductors. *Phys. Rev. B*, 38:9375–9389, Nov 1988.
- [125] N. A. Sinitsyn, Qian Niu, Jairo Sinova, and Kentaro Nomura. Disorder effects in the anomalous Hall effect induced by Berry curvature. *Phys. Rev. B*, 72:045346, Jul 2005.
- [126] Naoto Nagaosa, Jairo Sinova, Shigeki Onoda, A. H. MacDonald, and N. P. Ong. Anomalous Hall effect. *Rev. Mod. Phys.*, 82:1539–1592, May 2010.

-
- [127] H.P. Breuer and M. Holthaus. Quantum phases and Landau-Zener transitions in oscillating fields. *Physics Letters A*, 140(9):507–512, 1989.
- [128] Johannes Mitscherling and Walter Metzner. Longitudinal conductivity and Hall coefficient in two-dimensional metals with spiral magnetic order. *Phys. Rev. B*, 98:195126, Nov 2018.
- [129] James W McIver, Benedikt Schulte, F-U Stein, Toru Matsuyama, Gregor Jotzu, Guido Meier, and Andrea Cavalleri. Light-induced anomalous Hall effect in graphene. *Nature physics*, 16(1):38–41, 2020.
- [130] S. A. Sato, J. W. McIver, M. Nuske, P. Tang, G. Jotzu, B. Schulte, H. Hübener, U. De Giovannini, L. Mathey, M. A. Sentef, A. Cavalleri, and A. Rubio. Microscopic theory for the light-induced anomalous Hall effect in graphene. *Phys. Rev. B*, 99:214302, Jun 2019.
- [131] Di Xiao, Yugui Yao, Zhong Fang, and Qian Niu. Berry-phase effect in anomalous thermoelectric transport. *Phys. Rev. Lett.*, 97:026603, Jul 2006.
- [132] Tian Liang, Jingjing Lin, Quinn Gibson, Tong Gao, Max Hirschberger, Minhao Liu, R. J. Cava, and N. P. Ong. Anomalous Nernst effect in the Dirac semimetal Cd_3As_2 . *Phys. Rev. Lett.*, 118:136601, Mar 2017.
- [133] Fernando de Juan, Adolfo G Grushin, Takahiro Morimoto, and Joel E Moore. Quantized circular photogalvanic effect in Weyl semimetals. *Nature communications*, 8(1):1–7, 2017.
- [134] Y.-H. Chan, Berkay Kilic, Moritz M. Hirschmann, Ching-Kai Chiu, Leslie M. Schoop, Darshan G. Joshi, and Andreas P. Schnyder. Symmetry-enforced band crossings in trigonal materials: Accordion states and Weyl nodal lines. *Phys. Rev. Materials*, 3:124204, Dec 2019.
- [135] Th. Hahn. *The 230 space groups*, pages 112–717. Springer Netherlands, Dordrecht, 2002.

Acknowledgments

Foremost, I would like to thank my supervisor Dr. Andreas P. Schnyder for inspiring this project, for all his guidance, helpful advice and support in the completion of this work, without which this project would not have been possible. I am also deeply grateful to Prof. Dr. Walter Metzner for this special opportunity to work in his fantastic group, for providing me with the opportunity to attend valuable conferences, summer schools and group retreats, and for his continuous support. Furthermore, I want to thank all the members of my thesis advisory committee and Prof. Dr. Hans Peter Büchler for his participation in the examination board and evaluation of this work. I also want to thank all the people on this institute working tirelessly to ensure a smooth operation, especially Jeanette Schüller-Knapp and the IT department.

A big "Thank you!" goes to all group members and my collaborators, first of all for creating such a welcoming and inspiring environment of open thoughts, open doors and helping hands. Thank you also for all the vivid and enriching discussions, nice memories and coffees. Especially, I would like to thank Moritz for being the best office mate one could ask for, his enriching explanations, for brightening up dull days and endless evenings, for all the snacks and finally for enduring all the extracurricular activities, even when they went a bit over his head. Or right at it. Special thanks also go to all the frequent visitors in our office and partners in crime, especially my two other long-time companions Jáchym and Johannes.

Last but not least I thank my wife Kalina from the bottom of my heart for all the support, patience and for always believing in me, way from before I started this project to the very end and beyond.

**Schriftliche Bestätigung der eigenständig erbrachten Leistung gemäß
§ 6 Absatz 2 der Promotionsordnung der Universität Stuttgart**

Die eingereichte Dissertation zum Thema
”Crystalline topological semimetals: Classification and properties”
stellt meine eigenständig erbrachte Leistung dar.

Ich habe ausschließlich die angegebenen Quellen und Hilfsmittel benutzt.
Wörtlich oder inhaltlich aus anderen Werken übernommene Angaben habe
ich als solche kenntlich gemacht.

Die Richtigkeit der hier getätigten Angaben bestätige ich und versichere,
nach bestem Wissen die Wahrheit erklärt zu haben.

Stuttgart, den 26. 08. 2022



Andreas Leonhardt